mNeonGreen-collagen12: a tool for real time, high resolution, visualisation of collagen I trafficking

ELEANOR ROSE CASEY

mNeonGreen-collagen1α2: a tool for real time, high resolution, visualisation of collagen I trafficking

Eleanor Rose Casey

This thesis is submitted as part of the requirements of the degree of

Master of Research

Department of Biological Sciences

Durham University

March 2021

Abstract

Collagen I is a fibrillar protein of the extracellular matrix, where it provides strength and support to a number of connective tissues. Collagen I is produced by the cells of connective tissues as a short procollagen peptide, which self-assembles into fibrils upon secretion. Despite its important role in the skin, there are still gaps in our understanding of the intracellular trafficking and extracellular fibril assembly of collagen I. The highly dynamic nature of collagen I trafficking makes light microscopy the best tool to further investigate this process.

In this thesis, an mNeonGreen-collagen1α2 fusion protein will permit live imaging of collagen I in real time and with a higher resolution than previously achieved within the field. Following design of the construct, the expression of mNeonGreen-collagen1α2 was characterised within three immortalised cell lines of interest and extensively controlled for. mNeonGreen-collagen1α2 successfully permitted imaging all stages of collagen I trafficking: from synthesis, through the cell secretory pathway, and fibril assembly in the extracellular matrix. mNeonGreen-collagen1α2 was also used to investigate biological and cosmetic questions within the field. Overall showing that mNeonGreen-collagen1α2 is a robust, replicable and biologically relevant tool to study collagen I trafficking in real time with high resolution.

Table of Contents

Table of Figures

Table of Tables

List of Abbreviations

AA – Ascorbic Acid

ACN – Acetonitrile

BFA – Brefeldin A

BSA – Bovine Serum Albumin

bp – base pairs

CHX – Cycloheximide

CLEM – Correlative Light and Electron Microscopy

CMP – Collagen Mimetic Peptide

CMV – cytomegalovirus

CO_2 – Carbon dioxide

CRM – Confocal Reflection Microscopy

DMEM – Dulbecco's Minimum Essential Medium

DNA – Deoxyribose nucleic acid

E. coli – Escherichia coli

ECM – Extracellular Matrix

ER – Endoplasmic Reticulum

FBS – Foetal Bovine Serum

GAMPO – Goat anti-mouse phosphor-oxidase

GFP – Green Fluorescent Protein

Golgi – Golgi apparatus

Hsp47 – Heat Shock Protein 47

Lat B – Latrunculin B

LC-MS – Liquid Chromatography Mass Spectrometry

MEM – Eagle's Minimum Essential Medium

mNG – mNeonGreen

mNG-COL1α2 – mNeonGreen-collagen1α2

mRNA – messenger ribose nucleic acid

NAT – Native promoter

P&G – the Procter and Gamble Co.

P4HA – Proline 4-Hydroxylase A

P4HB – Proline 4-Hydroxylase B

PALM – Photoactivated localisation microscopy

PBS – Phosphate Buffered Saline

PDI – Protein Disulphide Isomerase

PFA – Paraformaldehyde

PM – Plasma Membrane

PVDF – Polyvinylidene fluoride

RAGPO – Rabbit anti-goat phosphor-oxidase

RT – Room Temperature

SARPO – Swine anti-rabbit phosphor-oxidase

SDS-PAGE – Sodium Dodecyl Sulphate Polyacrylamide gel electrophoresis

SHG – Second Harmonic Generation

TBST – Tris buffered saline with tween

TET – Tetracycline

TFA – Trifluoroacetic acid

TGN – Trans-Golgi Network

TIRF – Total Internal Reflectance Microscopy

tRNA – transfer ribose nucleic acid

Declaration of originality

I confirm that this thesis is my own work. It contains no material previously submitted for a degree in this or any other institute. All data were obtained by myself other than those represented in the following figures: 1.1 C, 1.2, 1.3 A and B, 3.2 B and E, 4.3 A and B, 7.2 A, respective authors are credited in the legends. This thesis does not infringe upon copyright or proprietary rights and no material has been previously published or written, except where references are made.

Statement of copyright

Acknowledgements

I must firstly thank my supervisors; Dr Tim Hawkins and Dr Adam Benham. Prior to this masters I had no lab experience or understanding what academic research was like. Their training, supervision and expertise has led to me to love research, and given me a future career that I am so excited about. I really can't thank them enough for this opportunity or the support I have received over the last 18 months. I must also thank the Proctor and Gamble Co. for their financial support and investment in my research, without which this project would not have been possible.

Thank you to all the members of lab 8 for your friendship, for making me smile on bad days, and for the spiciest group chat I have had the privilege of being in. I particularly need to thank Dr Max Brown for being an incredible teacher and putting up with my endless questions and mistakes, you've been a truly inspirational role model for me. Also sending big love to Clews for your role as my lab wife/partner in crime, I am so excited that we get to do this all over again for another four years.

Finally thank you to Mum, Dad, Jess and Granny for being the constants in my life; putting up with me for over 23 years now, I'm sure it hasn't always been the easiest thing to do! I am so appreciative of all for supporting me physically and emotionally, and allowing me to be uniquely myself. I hope you are all as proud of me as I am of you. All my love xxx

1 Introduction

Collagen accounts for approximately 30% of proteins expressed in animals and makes up 25% of the dry mass of humans. The collagen proteins represent a diverse group of ECM fibres and are expressed in connective tissues including the skin, bone, and cartilage (Nimni, 1983). Collagen I is synthesised as a procollagen polypeptide of approximately 300nm in length (Canty & Kadler, 2005). Procollagen undergoes extensive and sophisticated processing in the cell secretory pathway (Kelly, 1985). Following processing, collagen is secreted into the ECM where it self-assembles into a fibrous network to provide connective tissues with strength and support (Birk et al., 1989)

The study of collagen trafficking has relevance in academic, medical, and cosmetic research. Mutations in the collagen I protein resulting in incorrect trafficking and mis-folding can cause diseases such as osteogenesis imperfecta and Ehlers-Danlos Syndrome (Deshmukh et al., 2016). Understanding collagen trafficking is important to identify targets for novel treatment of these diseases. Collagen plays a vital role within the skin, providing support and structure to the tissue. As we age collagen I production decreases, resulting in the formation of wrinkles and older looking skin (Lim Goh et al., 2018; Panwar et al., 2018). For this reason, collagen I is a promising target of anti-aging creams within the skin care industry.

Analysis or visualisation of collagen I trafficking is limited by its large size, insolubility, repetitive sequence and hierarchical structure. These properties make collagen very difficult to analyse via conventional biochemistry, especially if interacting proteins, for example those which chaperone and modify procollagen in the Golgi, have not been identified (Banushi et al., 2016; Shoulders & Raines, 2009). Methods of collagen imaging are advancing, and have been used effectively alongside traditional biochemical approaches to analyse collagen trafficking in real time (section 1.3).

1.1 The procollagen triple helix

The procollagen peptide is characterized by globular N and C terminal domains and a central triple helix (figure 1.1). The procollagen triple helical domain has a highly unusual amino acid composition; proteomic data shows that 33% of all amino acid residues are glycine, with a further 20% made up of proline and hydroxyproline (Bowes & Kenten, 1948). This gives rise to a model whereby the primary structure of the collagen peptide comprises a triplet repeat of Gly-X-Y where X and Y are typically filled by proline and hydroxyproline, respectively (Long et al., 1993; Ramshaw et al., 1998; figure 1.1A)

In the ER, procollagen peptides trimerise following synthesis giving rise to the distinctive collagen triple helix, stabilised by the unusual primary peptide sequence of procollagen. The triple helix was first identified by X-ray diffraction photography, which shows that extended collagen fibres are trimers with 10-fold symmetry which form a right handed, coiled-coil triple helix (Ramachandran & Kartha, 1954; Rich &

Crick, 1961; figure 1.1 B-C). Protein crystallography shows that the triple helix is stabilised through hydrogen bonds between glycine residues on each procollagen peptide, and through interactions between hydroxyproline and the surrounding water molecules (Bella et al., 1994; Bella et al., 1995; Berg & Prockop, 1973; Jiravanichanun et al., 2006).

The formation of the triple helix is nucleated with disulphide bonds form between the C termini of three procollagen peptides (Bächinger et al., 1980; figure 1.1C). Trimerisation then occurs in a linear fashion toward the N terminus, with isomerisation of proline residues acting as the rate limiting step (Frank et al., 2003). The presence of hydroxyproline within the structure has a stabilising effect and allows triple helix formation to occur at a higher rate (S. Boudko et al., 2002). The N terminus remains extended following triple helix formation, allowing collagen to be directed through the cell and preventing premature fibrillogenesis. Once collagen has been secreted from the cell, the N and C termini are cleaved through proteinase activity, allowing collagen to assemble into mature fibres.

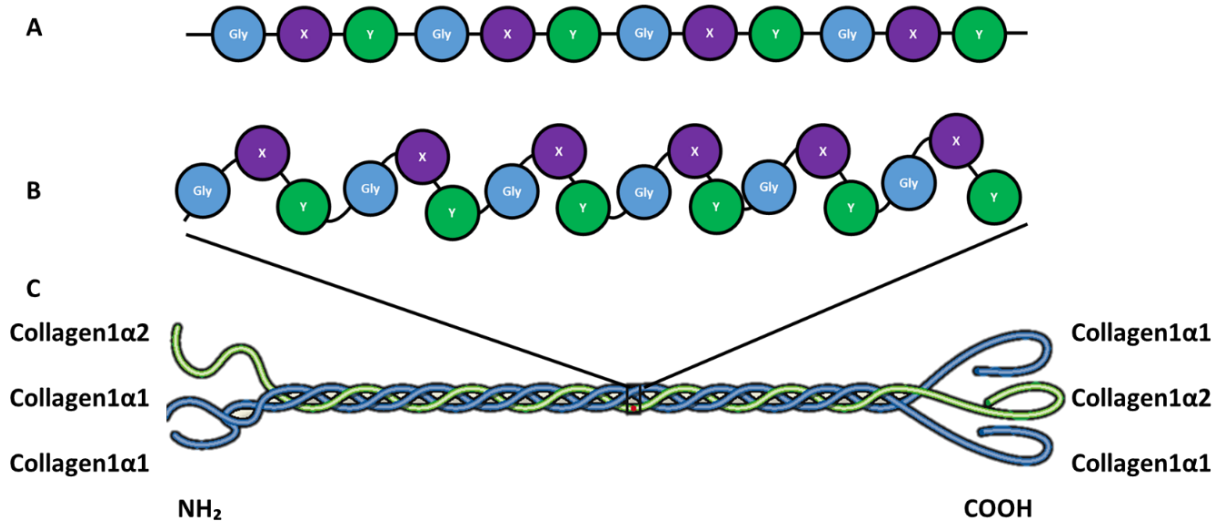

Figure 1.1 the molecular structure of collagen I. (A) primary structure of Collagen1 consists of Gly-X-Y triplet repeats. (B) Secondary Structure of Collagen1 in a left-handed alpha helix. (C) Procollagen tertiary structure is a heterotrimeric triple helix with globular N and C terminal domains. Image in C is adapted from Brodsky & Baum, 2008.

1.2 Collagen trafficking

1.2.1 Translation into the ER

Procollagen is co-translationally targeted to the ER through its N terminus signal peptide (Karamyshev et al., 2020; Rajpar et al., 2002). Within the ER, three procollagen peptides associate together to form the triple helix (Section 1.2). Whilst trimerisation occurs, ER resident chaperone proteins act upon procollagen to ensure correct folding. The P4H subunit of PDI acts upon the procollagen peptides to facilitate inter-chain disulphide bond formation. A P4HB/P4HA complex further acts upon collagen to convert proline to hydroxyproline, stabilising the procollagen triple helix (Koivu et al., 1987). Selected lysine residues are glycosylated at this stage by the galactotransferases GLT25D1 and GLT25D2 (Schegg et al., 2009). The activity of P4H is facilitated by an AA cofactor. When AA is removed, or P4H is knocked down, collagen is retained in the ER due to incorrect folding (Walmsley et al., 1999). During the process of triple helix formation, Hsp47 binds to the N terminus of procollagen to prevent premature folding while proline is hydroxylated. Once again loss of Hsp47 results in collagen retention in the ER (Ishida et al., 2006; figure 1.2).

1.2.2 ER-to-Golgi Trafficking

Following folding in the ER, procollagen triple helices are transported to the Golgi. Proteins are generally transported from ER to Golgi through COPII coated vesicles which are 60-90 nm in diameter. The procollagen triple helix is approximately 300nm in length, logically too large to be packaged in COPII secretory vesicles (Malhotra & Erlmann, 2015). However, components of the COPII vesicle are recruited to the ER upon collagen translation, and when Sar1, Sec13/31 or Sec23/24 are perturbed, procollagen is retained in the ER (S. D. Kim et al., 2012; Saito et al., 2017; Townley et al., 2008). These contradictory observations call into question the role of COPII in procollagen ER-to-Golgi trafficking.

1.2.2.1 The Role of COPII

A genome wide screen of cultured *Drosophila melanogaster* S2 cells identified that TANGO1, a transmembrane protein localized to the ER, is essential for procollagen ER-to-Golgi trafficking. Domain analysis of TANGO1 reveal SH3 domains in the ER lumen interact with procollagen, and a proline rich domain in the cytosol interacts with Sec23/24 proteins of the inner COPII coat (Saito et al., 2017). The presence of TANGO1 in the ER membrane accumulates procollagen into bundles within the ER. TANGO1 recruits a second protein cTAGE, which mediates COPII vesicle formation by controlling the GAP and GEF activity of Sar1, a monomeric small GTPase which regulates the assembly of COPII vesicles (Saito et al., 2011, 2014).

Sec31 initiates deformation of the ER membrane for COPII vesicle formation and is a target of CUL3-KLHL12 ubiquitination (Jin et al., 2012). It is proposed that Sec31 ubiquitination prevents normal scission

of COPII vesicles, allowing super-large COPII vesicles to form which transport collagen from ER to Golgi. However, super large vesicles have only been observed in systems in which ubiquitin ligase and adaptor Kelch-like proteins are overexpressed, making it hard to determine if super-large COPII vesicles form in physiologically relevant conditions (McGourty et al., 2016).

Stevens and colleagues transfected live cells with a collagen1α1-GFP construct to observe super-large collagen vesicle formation in real time (section 1.3.3.1). Overall, very few super-large COPII vesicles were observed in each cell, too few to be responsible for movement of all procollagens from ER to Golgi. The super-large COPII vesicles were slow moving and do not move toward the Golgi (McCaughey et al., 2019). These results support an alternative hypothesis that collagen moves to the Golgi through TANGO1-cTAGE5-COPII mediated membrane fusions of Golgi and ER (Mironov et al., 2003). This hypothesis is supported by high resolution imaging showing that lateral interactions between TANGO1 and cTAGE5 form a TANGO1/COPII ring which mediates fusion of cis-Golgi and ER membranes (Raote et al., 2018; Reynolds et al., 2019).

1.2.3 Golgi Progression

There are two theories which are used to describe the movement of collagen through the Golgi. Procollagen visualised by electron microscopy as electron dense aggregates in the Golgi provides support for a model in which collagen is moved through the Golgi by cisternal maturation (Bonfanti et al., 1998). Cisternal maturation is a model in which the Golgi cisternae move through the Golgi structure without secretory proteins transferring between them. As the cisternae move from the cis to the trans face of the Golgi they undergo a maturation process in which different chaperone proteins and enzymes for secretory protein modification fluctuate. In this model, the oversized cargo, such as procollagen I, does not have to leave the Golgi cisternae it entered into from the ER, until the cisternae has reached the trans-Golgi (J. J. Kim et al., 2016; Pelham, 2001).

In the second model, large proteins move directly between Golgi cisternae during fusion events between cisternae. Lateral fusions of Golgi stacks have been observed in mammalian cells, often called Golgi ribbons within the literature. Interruption of ribbon formation resulted in the prevention of collagen secretion from the cell. Furthermore, simpler animal cells, such as those of *Drosophila melanogaster* which do not have a complex Golgi capable of forming lateral connections between the Golgi cisternae, were not able to produce and secrete collagen at all (Lavieu et al., 2014). Inter-cisternal connections have also been observed as transient structures in cells which appear when the cell is undergoing a period of increased secretory protein production (Trucco et al., 2004). The mechanism by which procollagen I is trafficked through the Golgi is still disputed in the field.

1.2.4 Golgi to PM carriers

Compared to ER-to-Golgi transport, Golgi-to-PM transport is poorly characterised within the field generally, and particularly for procollagen trafficking. Evidence from electron microscopy and biochemical analysis identified the trans-Golgi as the site of site of protein sorting and Golgi egress (Griffiths & Simons, 1986). Proteins in the trans-Golgi are packaged into vesicles of diverse size and morphology, although the molecular determinants of formation and budding of post-Golgi carriers remain undetermined within the field (Stalder & Gershlick, 2020).

Procollagen presents a unique challenge for Golgi-to-PM transport because of its large size of 300 nm making it difficult to fit into typical clathrin or COP mediated vesicles of approx. 50-100 nm in size (section 1.2.2). Furthermore, evidence suggests that collagen fibrillogenesis can start once procollagen has left the Golgi, leading to an increased cargo size within the trafficked vesicles (section 1.2.5). Electron micrographs and CLEM show that procollagen is trafficked in highly pleomorphic post-Golgi structures (Mironov et al., 2003; Polishchuk et al., 2000). These large carriers are suggested to be microtubule dependent due to their reliance upon microtubule motor protein KIF5A in myoblasts (Kamata et al., 2017). The biological mechanism underlying the transport of procollagen I from Golgi to PM will be investigated in this thesis (section 6.0).

1.2.5 Collagen fibrilogenesis

Advanced transmission and serial block face scanning electron microscopy techniques show that fibrilogenesis of procollagen begins in membrane bound compartments, negative for lysosomal markers, between the trans-Golgi and plasma membrane called fibricarriers (Kalson et al., 2013). Fibricarriers are directed to plasma membrane protrusions known as fibripositors. The base of the fibripositors is the site of fibril nucleation while the tip is the site of procollagen secretion into the ECM (Canty & Kadler, 2005). The removal of N and C propeptides is essential for fibril nucleation and assembly, and is achieved by ADAM proteinases specific to the N or C terminus. There are conflicting studies within the literature to determine if ADAM proteinases are active within the cell or in the ECM (Canty-Laird et al., 2012; figure 1.2). It could be the case that alternative activation of ADAM proteinases is a cell or tissue specific phenomenon.

Once in the ECM, collagen self-assembles into bundles which grow in a linear fashion both axially and longitudinally, parallel to the fibripositor (Birk et al., 1989). Many different types of collagen come together to form the mature fibril. The process by which fibrillogenesis occurs is specific to the tissue and the microenvironment in which the collagen fibril is assembled. Electron microscopy shows that each end of this molecule has a distinct structure, indicating that the mature fibre has a polarity. Fibrillogenesis of polar collagen fibrils can be recreated *in vitro* (Ahn et al., 2018). In order to stabilize the collagen fibril network, collagen fibres must be cross linked through the action of lysine oxidases. EM studies show that cross links

occurs between the N and C termini of different fibrils (Eyre & Glimcher, 1973; Lucero & Kagan, 2006; figure 1.2).

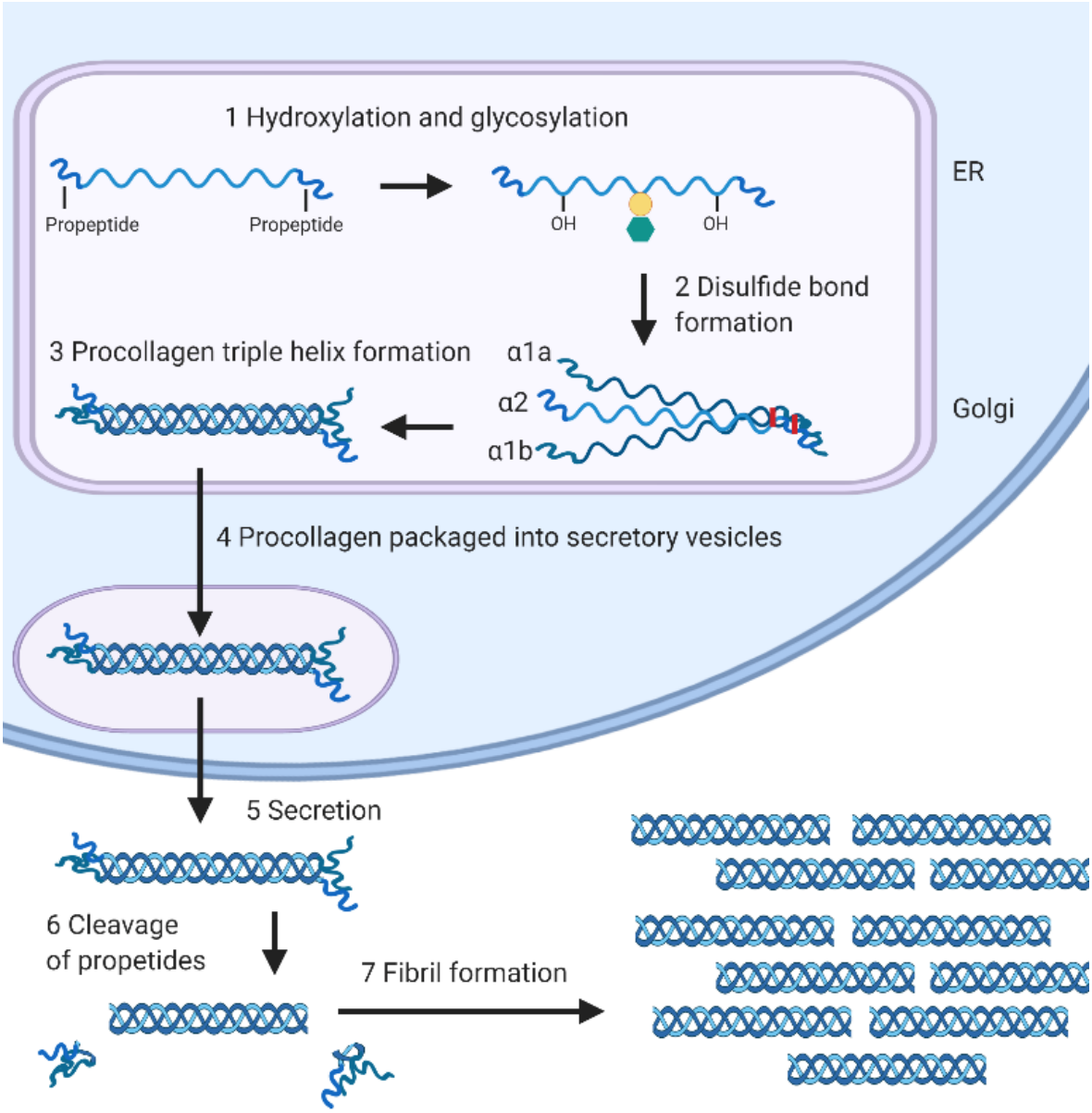

Figure 1.2 trafficking of procollagen I through the cell secretory pathway and extracellular assembly of collagen fibrils. Illustration made by Dr Max Brown.

1.3 Imaging collagen

Collagen in cells and tissues can be visualised by immunofluorescence, electron microscopy, or histological staining, following fixation. While highly effective at visualising collagen distribution, these techniques do not provide insight on the dynamic events which occur in live cells and tissues. Live imaging of intracellular procollagen trafficking and fibril assembly in the ECM, with high resolution and in real time is a valuable tool to correctly understand the complex process of collagen trafficking. Live imaging of collagen is hindered by the unique structural properties of collagen: its high tensile strength, hydrophobicity, repetitive primary amino acid sequence and tertiary structure, and large, bulky size. There are three confocal imaging approaches to visualise collagen within live organisms: utilisation of collagen's intrinsic optical properties, using fluorescent-labelled collagen binding proteins, or genetically modifying collagen to express a fluorescent tag. These three approaches have been widely used in the literature and are best suited to different biological questions, which will be discussed further in this section.

1.3.1 Utilising the intrinsic optical properties of collagen

The unique structure of collagen imparts upon it intrinsic optical properties, allowing visualization of collagen by confocal microscopy in the absence of fluorescent labels, or physical or chemical manipulation. Autofluorescence microscopy, CRM, and SHG utilise different optical properties of collagen to facilitate real time visualisation of collagen networks within the ECM of most connective tissues.

1.3.1.1 Autofluorescence microscopy

Collagen is autofluorescent due to the presence of aromatic amino acids at the point of crosslinks between mature collagen fibres in the ECM (Croce & Bottiroli, 2014). Autofluorescence microscopy has been successful to provide insight into the dynamics of collagen crosslinking in the ECM, as different 3D collagen structures will provide different emission patterns when excited by the same wavelength. This has been used to investigate the changes to collagen networks in photo-aged skin (Lutz et al., 2012).

1.3.1.2 CRM

To achieve confocal reflectance microscopy (CRM) of collagen fibres, samples are illuminated with a laser scanning confocal microscope. The intrinsic reflective properties of collagen allow incident light to be back scattered, amplified in a photomultiplier tube and detected. By imaging successive sections through a tissue, this technique has been used to monitor 3D changes to ECM collagen fibril network in real time. CRM has provided insights into the rate of fibril deposition and impact of other ECM proteins on the rate of collagen fibril formation (Brightman et al, 2000). Simultaneous CRM imaging with fluorescent labelled collagen, shows that the angle at which a collagen fibre is at relative to the optical plane will alter the brightness detected by CRM. In this study, the signal from collagen fibres greater than 50^{o} from the optical plane was lost, resulting in an incomplete map of the ECM (Jawerth et al., 2010). This shows that CRM might miss

some collagen fibril structures in *in vivo* studies. Therefore, CRM is most suited to visualising collagen in *in vitro* studies of collagen matrix assembly for tissue engineering (Hartmann et al., 2006).

1.3.1.3 SHG

SHG is a phenomenon in which incident light is reflected from a molecule at half the original wavelength (Williams et al., 2005). Fibrillary collagen is an extremely bright second harmonic generator. Unlike autofluorescence microscopy and CRM, SHG is more sensitive to refractive changes in the tissue making it better suited to distinguish between collagen populations and preventing interference from other ECM components (Chen et al., 2012). SHG is a powerful tool to visualise changes to the organisation of collagen in a range of human tissues and has great applications to biomedical research (Mansfield et al., 2019; Mostaço-Guidolin et al., 2017; Narice et al., 2016).

Of the three imaging techniques described above, SGH is best suited to *in vivo* visualisation of collagen fibril assembly. However, results from SHG can lack specificity, due to interference from other second harmonic generators, such as elastin in the ECM. Second-harmonic patterned polarisation-analysed reflection confocal microscopy is an enhanced version of CRM combined with SGH which allows collagen to be de-lineated from other ECM components and therefore reduces interference from the ECM (Okoro et al., 2018).

SHG CRM and autofluorescence microscopy techniques cannot image collagen during intracellular trafficking, when procollagen is less bifringent and autofluorescence from cell organelles interferes with data collection. Therefore, the above methods while effective at visualising 3D collagen structures in the ECM with no physical or chemical manipulation are unsuitable to study early intracellular trafficking events. A fluorescent tag for procollagen is needed to effectively achieve this.

1.3.2 Fluorescent Labelled Collagen-binding Proteins

Collagen can be indirectly labelled for laser scanning confocal microscopy by conjugating fluorophores to proteins which bind to collagen with high affinity. High affinity collagen binding proteins include synthetically derived CMPs or bacterial derived collagen binding probes.

1.3.2.1 CMPs

CMPs are small synthetic peptides typically 30 amino acids long. The primary sequence of a CMP is designed to closely mimic that of native procollagen, allowing the mimetic peptides to integrate into the procollagen triple helix (B. Sarkar et al., 2014). A fluorophore can be included into the CMP to permit confocal imaging of collagen *in situ*. By incorporating the fluorophore in the central section of the CMP, the CMP can incorporate with native collagen with high affinity (Cai et al., 2017). To integrate into an

existing procollagen triple helix, the bonds between the heterotrimer must first be broken. This can be achieved by heating which can damage the tissue (N. Sarkar et al., 2008).

In the literature, CMPs have been most successfully used to study collagen fibril assembly *in vitro* as part of an artificial biopolymer for tissue engineering (J. Luo & Tong, 2011; Parmar et al., 2016; A. Y. Wang et al., 2008). CMPs have been used in cell culture or *in vivo* to observe collagen dynamics in the ECM, but these studies are hindered by difficulties in synchronising CMP integration into existing collagen fibrils. CMPs have very little scope for visualisation of intracellular collagen trafficking due to problems surrounding delivery into the cell and the unknown behaviours of the structurally modified procollagen (Ellison et al., 2020; Xu & Kirchner, 2021).

1.3.2.2 Collagen Probes

CNA35 is a collagen binding toxin isolated from *Staphylococcus aureus* with high affinity for the collagen triple helix. CNA35 is conjugated to an Oregon-Green fluorescent probe allowing intracellular and ECM collagen to be visualised by confocal microscopy in real time with higher resolution and specificity than SHG (Krahn et al., 2006, 2006). CNA35 has since been successfully conjugated to a number of different coloured fluorophores (Aper et al., 2014). The CNA35 probe has shown to have highest affinity for collagen of all fluorescent probes currently available, but still undergoes non-specific binding with other fibrillary components of the ECM. Furthermore, the effect of probe binding and toxicity on the intracellular trafficking route of procollagen has not been investigated. The issues surrounding the use of the CNA35 probe and CMPs point to direct fluorescent labelling of procollagen as a more effective and accurate method of collagen visualisation.

1.3.3 Genetic Modification

Genetic engineering can be used to create DNA which when expressed by cells encodes procollagen fused with a fluorescent protein, allowing intracellular collagen trafficking to be easily observed. The location of the fluorescent protein insertion within procollagen will affect its assembly and trafficking. A number of collagen I fluorophore fusion constructs have been recently defined in the literature which feature a fluorophore inserted into the collagen peptide in different places, the efficacy of these different constructs will be discussed in this section.

1.3.3.1 Collagen1α1 GFP Fusion Constructs

In 2002, Stephens and Pepperkok inserted GFP into the C terminal of procollagen1α1 to investigate the dependence of collagen ER-to-Golgi trafficking on COPI and COPII. The synthesis of collagen1α1-GFP is AA dependent, implying that the construct is processed in the ER by P4HB in a similar fashion to native procollagen (section 1.2.1). The presence of GFP at the C terminus is likely to inhibit or alter procollagen

trimerisation, which is nucleated at the C terminus (section 1.1). This construct has limited potential to visualise extracellular fibril assembly due to placement of GFP downstream of the C terminal ADAM proteinase domain, resulting in GFP cleavage prior to secretion (Stephens & Pepperkok, 2002).

In 2019, McCaughy and colleagues designed a fusion construct with a GFP tag upstream of the N terminal cleavage domain of procollagen1α1, ensuring that triple helix formation occurs in a fashion more representative to that of native procollagen. The location of the tag upstream of the N terminus cleavage domain makes this construct suitable for intracellular investigation, as the tag will be cleaved by ADAM proteinases in the ECM. This fusion protein was instrumental in proving that collagen is not transported between the ER and Golgi in large COPII mediated vesicles (McCaughey et al., 2019).

1.3.3.2 Collagen1α2 GFP Fusion Constructs

Inserting GFP into collagen1α1 is an issue when studying intracellular trafficking, because there are 2 collagen1α1 subunits per procollagen heterotrimer, and collagen1α1 can homotrimerise (section1.1). This results in fluorescent signal amplification which can make results harder to quantify and interpret. By tagging collagen1α2, only one fluorophore will be present in each procollagen triple helix.

In 2018 Dallas and colleagues designed a GFP-collagen fusion construct in which GFP replaces the N terminal ADAM cleavage domain, preventing the fluorescent tag from being removed once procollagen was secreted. Deletion of the N terminal cleavage domain was demonstrated to not significantly alter the trafficking of collagen compared to wildtype in studies of Ehlers-Danlos patients, a genetic conditions characterised by the deletion of the N terminal ADAM cleavage domain. Therefore, the GFP-collagen fusion protein, designed by Dallas and colleagues, was determined to closely mimic the behaviour of wildtype collagen. The GFP-collagen fusion protein was used to observe deposition of collagen from osteoblasts in 2D culture. GFP tagged collagen moved around the nuclei of the cells below them as part of a dynamic process, and the deposition of tagged collagen was highly dependent upon the presence of fibronectin. Co-cultures of cells expressing GFP-collagen and mCherry-collagen show clearly for the first time that collagen fibres in the EMC are contributed to by multiple cells. Overall these studies confirmed that secretion and extracellular assembly of collagen is a highly dynamic process controlled by mechanical and chemical stimuli from the surrounding cells and ECM (Lu et al., 2018).

Martin and colleagues used the same construct to reveal collagen deposition at the tissue level in a zebrafish model. The deposition of GFP tagged collagen fibrils in zebrafish dermis following wounding to shed light on the nature of scarring and the role of collagen in wound healing in this organism (Morris et al., 2018). Constructs using an N terminal GFP tag to replace the ADAM proteinase domain can be used to visualise intracellular and ECM collagen both *in vitro* and *in vivo.*

1.4 mNG-COL1α2 fusion construct

In this thesis, the GFP-collagen1α2 construct used by Martin and colleagues has been adapted to provide a tool to study intracellular collagen trafficking in skin cells with high resolution in real time. This construct will use an mNG fluorophore rather than a GFP fluorophore, offering a number of advantages for image quality.

1.4.1 mNG vs GFP

mNG is a green/yellow fluorescent protein isolated from the marine invertebrate *Branchiostoma lanceolatum.* mNG is excited by blue light of 488 nm and has an emission of 518 nm. mNG far outperforms GFP as a protein tag: mNG is brighter than GFP, allowing it to be detected by lower laser intensities, over longer periods, or with a higher frame rate. mNG is less pH sensitive than GFP, preventing loss of signal as collagen is trafficked through intracellular compartments of varying pH (Shaner et al., 2013; Tanida-Miyake et al., 2018). The mNG fluorophore has a longer fluorescent half-life than GFP, facilitating confocal imaging for longer periods of time than have previously been described (Hostettler et al., 2017).

1.4.2 Plasmid and Fusion-Construct Design

A plasmid encoding a mNG-COL1α2 fusion construct has been generated. The expression of the fusion construct is controlled by one of three promoters: constitutively active CMV promoter to induce high levels of collagen expression, a TET inducible promoter to temporally control mNG-COL1α2 expression, or a NAT promotor to express mNG-COL1α2 in a fashion comparable to endogenous collagen1α2 (figure 1.3 A). Once expressed in living cells, the mNG tag will allow visualisation of collagen1α2 throughout the intracellular secretory pathway, and within the ECM. The location of the mNG tag on collagen1α2 will ensure that one fluorophore is found per triple helix, preventing signal amplification (figure 1.3 B).

The resultant collagen1α2 protein, expressed by the plasmid, has the N terminal pro-peptide entirely removed and replaced with mNG, flanked by GS linkers to confer flexibility to the fusion construct. Removal of the N terminal ADAM proteinase site will allow the mNG tag to be retained on collagen following secretion of the construct into the ECM, in a fashion which does not significantly alter the processing and/or trafficking of collagen (Section 1.3.3.2, Section 5). This will facilitate observation of fibre formation (figure 1.3 C). Construct design will be further discussed in section 3.

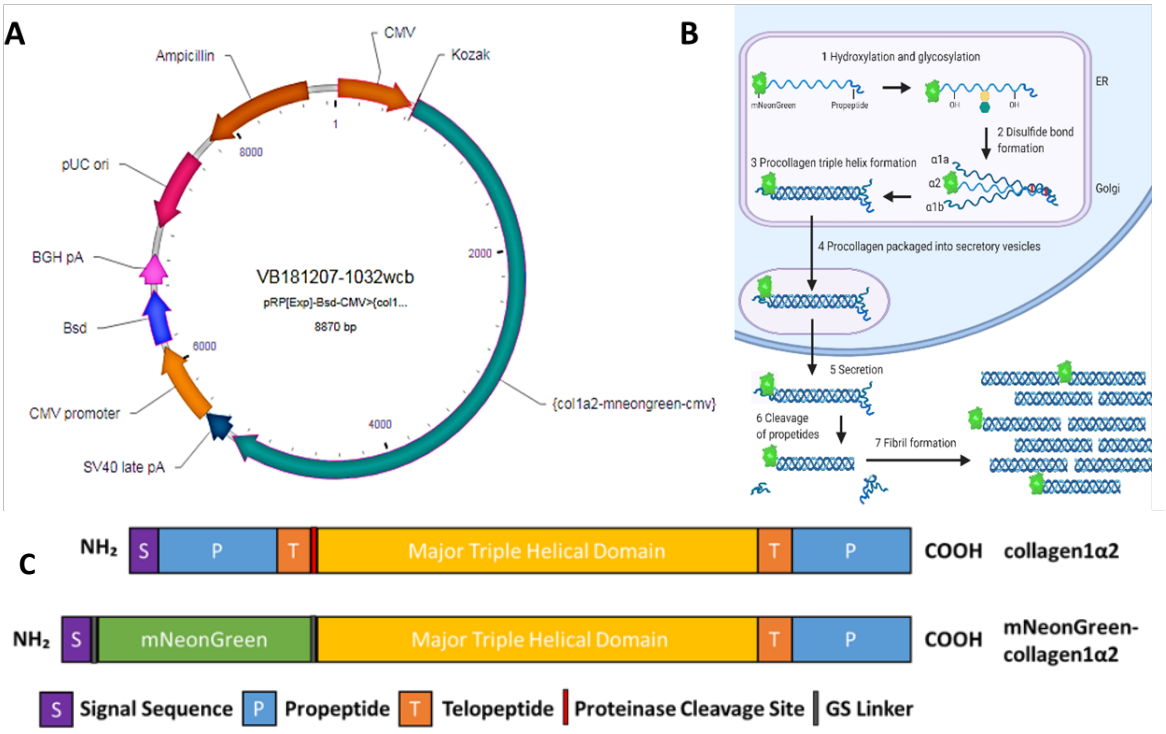

Figure 1.3 mNG-COL1α2 design. (A) Plasmid encoding Collagen1α2-mNeonGreen construct controlled by CMV promoter. TET inducible and native promoters also drive expression in similar alternative plasmids. (B) Intracellular trafficking and ECM processing of the mNG-COL1α2 construct to provide extracellular retention of mNeonGreen label and one label per procollagen I triple helix. (C) Comparison of domains of native collagen1α2 protein with mNG-COL1α2 fusion protein. mNG is inserted at the N terminus of the protein and flanked by GS linkers, removing all of the N terminal propeptide including the ADAM cleavage domain. Illustrations in part A and B made by Dr Max Brown.

1.5 Thesis aims

The aim of this research is to characterise a novel mNG-COL1α2 construct as a tool to visualise collagen trafficking in real time with high resolution. This will include all intracellular trafficking events and extracellular fibril assembly. The construct will be extensively characterised and will eventually be used to investigate biological, medical and industrial questions. This will be achieved by addressing the following aims:

1. Expression of mNG-COL1α2 will be characterised and controlled for in cell lines of interest.
2. mNG-COL1α2 will be used to visualise all stages of collagen trafficking and secretion.
3. Demonstration that mNG-COL1α2 can be used to investigate relevant biological questions.
4. Demonstration that the mNG-COL1α2 can be applied to relevant industrial investigations.

2 Materials and Methods

2.1 Plasmids

2.1.1 Plasmid design and manufacture

Three plasmids encoding the mNG-COL1α2 construct were designed using pDRAW32 (pDRAW32, version 1.1.102, 2009-05-13, AcaClone software, http://www.acaclone.com/). In each plasmid variation the mNG-COL1α2 construct is under the control of an alternative promotor; CMV for constitutive expression, TET inducible for temporal control of expression, and the native fibroblast promotor for collagen to observe natural expression. The plasmids also contain genes for resistance to ampicillin in *E. coli* and resistance to blastocidin in fibroblast cells. Both resistance genes are controlled by constitutive promotors. A further plasmid encoding histidine tagged mNG alone under the control of a CMV promotor (pNCS), and encoding an ampicillin resistance gene. Plasmids were manufactured and transfected into DH5α *E. coli* by VectorBuilder (Vector Builder, version 2.1.333, 2020-03-17, BioConnect life sciences software, https://www.bio-connect.nl/vectorbuilder/cnt/page/6374). *E. coli* expressing plasmids were stored at -80 ºC prior to expansion.

2.1.2 Plasmid expansion

Transformed *E. coli* expressing one of the plasmids for mNG-COL1α2 were plated on sterile 2.5% (w/v) LB agar plates (ThermoScientific, 15400675) made with 100 μgmL^{-1} ampicillin as diluted from a 100 $mgmL^{-1}$ stock (Sigma, A9518). After a 36 hr growth period at 37 ºC, two single colonies were inoculated into two sterile inoculation tubes (ThermoFischer, 50-809-216) each containing 3 mL sterile 25% LB broth; 20% Yeast extract, 40% sodium chloride, 40% peptones, casein (ThermoScientific, 10638013) with 100 μgmL^{-1} ampicillin. The tubes were incubated at 37 ºC with mild shaking for 8 hr to allow amplification of bacteria. Following 8 hr incubation the culture was split into two 1.5 ml aliquots which were transferred into four sterile conical flasks, containing 150 mL of 25% (w/v) sterile LB broth with 100 μgmL^{-1} ampicillin. The cultures were incubated at 37 ºC with mild shaking overnight. The following day the cultures were split into three 50 mL aliquots and transferred to eight 50 mL conical tubes (Greiner Bio-One, 227261). The aliquots were centrifuged at 20,000 g for 30 min at 4 ºC to pellet the bacteria and the supernatant discarded. All the above steps were carried out in sterile conditions around a Bunsen burner.

To obtain plasmid DNA, *E. coli* cells were lysed and pelleted by centrifugation to obtain soluble elements which were then filtered to isolate DNA. A Qiagen mini/midi/maxi prep kit (Qiagen, 12162) was used to isolate the plasmid from the combined pellets, following the manufacturer's instructions. DNA was dissolved in filter sterilised 1x TE buffer; pH 8, 10 mM Tris (Sigma Aldrich, T1503), 1 mM EDTA (ThermoScientific, AM9260G). The concentration of the DNA was determined using a NanoDrop 1000 Spectrophotometer (ThermoScientific). Plasmids were stored at -20 ºC prior to use.

2.2 Purification of mNeonGreen

2.2.1 Bacterial Lysis

E. coli transformed with the pNCS plasmid were grown at 37 ºC for 24 hr on sterile, agar plates, supplemented with 100 µgmL^{-1} ampicillin. Single colonies were inoculated in 3 mL LB broth with 100 µgmL^{-1} ampicillin. After an 8 hr incubation period at 37ºC with mild shaking, the inoculated bacteria were separated into 1 mL aliquots placed into Eppendorf tubes. The bacterial suspension was pelleted by centrifugation at 16,000 g at 4 ºC for 10 min and the supernatant discarded. The pellet was washed by re-suspension in a Tris buffer; 50 mM Tris, pH 7.4 then centrifuged at 16,000 g at 4 ºC for 10 min, the supernatant was once again discarded. The pellet was re-suspended in Tris buffer; pH 7.4, 50 mM Tris, 10 µgmL^{-1} proteinase inhibitor. Twenty percent (v/v) glass beads (Sigma Aldrich, G4649) were added to the suspension. The mixture was vortexed for 60 s then cooled on ice for 30 s 6 times to lyse the bacterial cells (section 3.1). The bacterial lysate was centrifuged again at 16,000 g at 4ºC for 10 min and the supernatant transferred to a fresh 1.5 mL tube. The pellet was discarded. The supernatant was flash frozen in liquid nitrogen, and stored at -20 ºC prior to either purification on NTA agarose beads or gel electrophoresis.

2.2.2 His purification of mNeonGreen

A suspension of 1 mL nickel agarose beads FIND OUT WHERE THE HIS TAG COMES FROM (Thermo Scientific, 88221) was placed in a 15 mL conical tube and washed by suspending in 10 mL Tris HCl Buffer, pH 4 then centrifuged at 16,000 g for 5 min at RT and the supernatant removed. One millilitre of bacterial lysate (section 2.2.1) was applied to the beads and incubated by gentle rocking on ice for 5 min. The beads were centrifuged at 16,000 g for 5 min at 4 ºC and the supernatant removed. The beads were then suspended in 1.5 mL elution buffer; Tris HCl, 200 µM imidazole, pH 7.4 (Sigma Aldrich, 56750). The beads were incubated on ice for 5 min with gentle shaking then centrifuged at 16,000 g for 5 min at 4 ºC. The supernatant was removed and the beads re-suspended in elution buffer. The elution process was repeated three times and each supernatant retained as a separate fraction. The four resulting fractions were flash frozen in liquid nitrogen and stored at -20 ºC prior to further investigation.

2.3 Cell Culture

Cultures of the human fibrosarcoma cell line HT1080 (ATCC, CCL-121^{TM}), human immortalized fibroblast cell line BJ hTERT (gifted by P&G), and primary human osteogenic sarcoma cell line Saos-2 (ECACC, 89050205) were grown in a humidified incubator at 37 ºC and 5% CO_2. Adherent cells were passaged with appropriate frequency in T75 flasks (TPP, 90076). Passage took place under sterile conditions in CL1 flow hood. HT1080 cells were grown in DMEM (Fischer Scientific, 11500596), BJ hTERTs were grown in MEM (Fischer Scientific, 11095080), and Saos-2 were grown in McCoy's 5A (modified) media (Fischer Scientific, 16600082). All media types were supplemented with 100 µgmL^{-1} penicillin and 100 µgmL^{-1}

streptomycin (Fischer Scientific, 15140122) and 10% GlutaMAX (Fischer Scientific, 35050038). DMEM, MEM and McCoy's were supplemented with 8%, 10% and 10% FBS (Fischer Scientific, 10082139), respectively.

To passage cells, spent media was removed from the flask and cells were washed once in 6 mL (for T75) of RT sterile PBS; pH 7.4, 1.5 mM KH_2PO_4, 155.2 mM NaCl, 2.7 mM Na_2HPO_4-$7H_2O$) (Fischer Scientific, 20012068). One millilitre of trypsin (Fischer Scientific, 11570626) was applied to the cells for 1 min, then 0.5 mL was removed and the cells were incubated at 37 ºC for 5 min. A single cell suspension was generated by adding pre-warmed media to trypsinised cells and aspirating. One millilitre or five millilitres of cell suspension was added to fresh flasks filled with 10 mL of warm sterile media to achieve the desired confluence; 1:10 for HT1080 and 1:2 for BJ hTERT and Saos-2. The sub-cultured cells were then returned to the incubator and allowed to grow for 3 – 7 days depending on the cell type.

2.4 Cell Transfection

2.4.1 Transient transfection of HT1080 cells

HT1080 cells between passage 1 - 30 were plated at 30% confluency 24 hr prior to transfection into either 35 mm glass bottom dishes (Ibidi, 81158) for live imaging, or into 6 cm dishes (TPP, 93060) for lysis. Immediately prior to transfection spent media was removed from the dish and cells were washed once in 1 mL PBS before 2 mL (35 mm dish) or 5 mL (6 cm dish) of pre-warmed DMEM, as described above, media was added to the cells. DNA was delivered into cells via JetPEI DNA transfection reagent (VWR, 101-10N). Transfection complexes; 90% NaCl, 8% JetPEI transfection reagent, 2% (w/v) plasmid DNA were applied to cells according to the manufacturer's instructions. After a further 24 hr incubation the cells were investigated by light microscopy or lysed.

2.4.2 Transient transfection of BJ hTERT cells

Twenty-four hr prior to transfection, BJ hTERT fibroblasts between passage 1 - 20 were plated at 60% confluency into a suitable dish for future experiments. Immediately prior to transfection spent media was removed from the dish and cells were washed once in 1 mL sterile PBS before 2 mL (35 mm dish) or 5 mL (6 cm dish) of pre-warmed MEM media, was added to the cells.

DNA was delivered to the cells via BJ transfection reagent (Altogen, 6210); Transfection complexes; 90% serum-free MEM, 8% Altogen transfection reagent, 2% (w/v) plasmid DNA were delivered into the cells according to the manufacturer's instructions. After 24 hr, spent media was removed to avoid prolonged exposure of cells to transfection reagent. Cells were washed in 1 mL PBS before 2 mL (35 mm dish) or 5 mL (6 cm dish) of pre-warmed MEM media was added to the cells with 100 µM transfection enhancer (Altogen, 6210). After a further 24 hr incubation the cells were investigated by light microscopy or lysed.

Alternatively, cells were transfected with JetPEI using the same method as for HT1080 cells (section 2.4.1). DNA was also delivered by JetPRIME (vwr, 712-60) according to manufacturer's instructions. Transfection complexes were made by diluting JetPRIME transfection reagent 1:20 in JetPRIME buffer and the solution supplemented with 1.5% (w/v) plasmid DNA according to the manufacturer's instructions. Finally, transfection complexes were made by diluting JetOPTIMUS (vwr, 117-01) transfection reagent 1:44 in JetOTPIMUS buffer and supplementing with 1.5 % (w/v) plasmid DNA, according to the manufacturer's instructions.

2.4.3 Transient transfection of Saos-2

Saos-2 cells between passage 1 – 30 were plated into a suitable dish for future experiments at 60% confluence. Immediately prior to transfection, spent media was removed and the cells briefly washed in 1 mL RT 1x PBS. DNA was delivered to the cells using lipofectamine 3000 transfection kit (Thermo Fischer, L3000), according to manufacturer's instructions. Lipofectamine 3000 reagent was diluted 1:17 in Opti-MEM reduced serum media (Thermo Fischer, 31985070). In a separate Eppendorf tube, P3000 reagent was diluted 1:25 in optimum media, this solution was supplemented with 1% (w/v) plasmid DNA. Both solutions were mixed well, combined and incubated for 5 min RT. The solution was then incubated with the Saos-2 cells for 1 hr at 37 ºC in the absence of media, before the addition of an appropriate volume of McCoy's growth media. Following a further 24 hr growth period the cells were investigated by further experimentation.

2.5 Cell Lysis

Prior to lysis, cells were plated and transfected in 6 cm dishes (TPP, 93060). Spent media was removed and cells were washed 3 times with RT, non-sterile PBS (Gibco, 100100023) then placed on ice. To lyse the cells, 150 µL of ice cold 1x MNT buffer; 20 mM MES (Sigma Aldrich, M8250), 30 mM Tris-HCl (Sigma Aldrich, T3253), 100 mM NaCl (Sigma Aldrich, S7653), pH 7.4, supplemented with 1% v/v Triton X-100 (Sigma Aldrich, X100) and 100 µLmL^{-1} protease inhibitor cocktail; 104 mM AEBSF, 80 µM Aprotinin, 4 mM Bestatin, 1.4 mM E-64, 2mM Leupeptin, 1.5 mM Pepstatin A) (Sigma Aldrich, P8340), was then added to the cells for up to 30 min. Alternatively cells were lysed in 150 µL of ice cold 1x RIPA buffer; 50 mM Tris HCl, 150 mM NaCl, 1.0% (v/v) NP-40 (Thermo Scientific, 13434269), 0.5% (w/v) sodium deoxycholate (Merk Life Science, D6750), 1.0 mM EDTA, 1.0% (w/v) SDS, 0.01% (w/v) sodium azide (Fischer Scientific, 10592211), pH 7.4, supplemented with 100 µLmL^{-1} proteinase inhibitor cocktail. Cells were extensively scraped with a cell lifter (Thermo Fischer, 11577692) and the lysate transferred into 1.5 mL Eppendorf tubes (Starlab, S1615-5550). Lysates were centrifuged at 16,000 g for 5 min at 4 ºC to pellet the nuclei. The post-nuclear supernatant was transferred to a fresh 1.5 mL Eppendorf tube, flash frozen in liquid nitrogen and stored at -20 ºC for further analysis. Pellets were discarded.

2.6 Acetone precipitation

The protein component of spent media removed from cells immediately prior to lysis was concentrated by acetone precipitation. Spent media was placed in a 50 mL falcon tube and 4x the sample volume of -20 ºC acetone (ThermoFischer, A/0600/17) was added. The tube was briefly vortexed prior to a 1 hr incubation at -20 ºC. The tube was vortexed 10,000 g for 30 min and the supernatant discarded. The pellet was air dried for 30 min, then re-suspended in an appropriate volume of lysis buffer to achieve the desired protein concentration.

2.7 Protein Concentration Estimation

2.7.1 BCA Assay

A BCA assay was performed on all cell lysates to calculate the post nuclear protein concentration using a QuantiPro^{TM} BCA Assay Kit (Fisher Scientific, 10678484) in a 96 well plate (Fischer Scientific, 10656853). Standards of the following concentrations: 0, 25, 125, 250, 500, 750, 1000, 1500, 2000 $\mu L mL^{-1}$ in distilled water were prepared from a 2 $mgmL^{-1}$ BSA (Sigma Aldrich, A7517) stock. Duplicate 10 µL aliquots of each standard and each cell lysate were added to individual wells. Two hundred microliters of working reagent were added to each well and the plate incubated at 37 ºC for 30 min. The absorbance of each well at 562 nm was subsequently measured on a standard plate reader. The standards were used to plot a standard curve of concentration against absorbance, which was used to determine the concentration of the cell lysates.

2.7.2 Bradford Assay

The Bradford assay was used as an alternative to the BCA assay in the case were compounds such as imidazole would interfere with the absorbance spectrum. Standards of; 0, 0.2, 0.4, 0.6, 0.8, 1.0 $mgmL^{-1}$ were made up in dH_2O from a 2 $mgmL^{-1}$ BSA stock solution. Ten microliters of standards and samples were placed in individual wells of a 96-well plate in duplicate. Two-hundred microliters of Bradford's reagent (Bio-Rad, 5000-0205) was added to each well and the plate was incubated at RT for 15 min. The plate was read at 595 nm. The standards were used to plot a standard curve of known protein concentration against absorbance, which was used to determine the protein concentration of the unknown samples.

2.7.3 Collagen Quantification Assay

A novel fluorescence assay was developed to quantify the amount of mNG-COL1α2 protein present in a cell lysate. Standards of; 10.00, 5.00, 2.50, 1.25, 1.00, 0.1, 0.01, 0.001 μgmL^{-1} in Tris HCl buffer were made up from 0.1 $mgmL^{-1}$ stock of purified mNG protein in Tris HCl (section 2.2.2). Fifty microliters of cell lysates and standards were added to individual wells of a black walled 96-well (Fischer Scientific, M33089), standards were loaded in duplicate. Fluorescence was read on a fluorescent plate reader; excitation 488 nm, emissions 518 nm, gain 50. The standards were used to plot a standard curve comparing

fluorescence to known mNG concentration. The standard curve was used to determine the mNG-COL1α2 concentration of the cell lysates.

2.8 Gel Electrophoresis

2.8.1 SDS PAGE gel electrophoresis

SDS PAGE 10% gels 1.0 mm thick were cast using a Bio-Rad Mini-PROTEAN® casting stand (Bio-Rad, 1658003FC). The resolving gel was comprised of; 4.8 mL dH_2O, 2.5 mL 40% acrylamide (Severn Biotech Ltd, 20-2400-10), 2.5 mL 1.5M Tris, pH 8.8, 0.1 mL 10% SDS (Severn Biotech Ltd, 20-4000-10), 0.1 mL 10% APS (Sigma Aldrich, A3678), 4 µL TEMED (Fischer Scientific, 10689543). The stacking gel was cast above the resolving gel with a 10-well comb (Bio-Rad, 1658003FC) and comprised; 1.5 mL dH_2O, 0.25 mL 40% acrylamide, 0.25 mL 1 M Tris pH 6.8, 20 µL 10% SDS, 15 µL 10% APS, 2 µL TEMED. A maximum volume of 20 µL of cell lysate was prepared for loading by mixing 1:1 with 2x Laemmli loading buffer (65.8 mM Tris-HCl, pH 6.8, 26.3% (w/v) glycerol, 2.1% SDS and 0.01% bromophenol blue) (Bio-Rad, 161-0737) supplemented with 50 mM DTT (Sigma Aldrich, 04689721) reducing agent and boiled at 91 ºC for 5 min. Samples were loaded onto the SDS PAGE gel alongside a pre-stained protein ladder (Bio-Rad, 1610374). The gel was run in a tank (Bio-Rad, 1658003FC) containing 1x Tris-Glycine running buffer; 25 mM Tris, 192 mM glycine, 0.1% SDS, pH 8.3, diluted from a 10x stock (Bio-Rad, 1610772) at 50 mA for 30 min.

The gel was stained with coomassie (section 2.10) or transferred to a PVDF membrane (Fisher Scientific, 88520). The membrane was activated by submersion in 100% methanol for 20 s, then submerged in 1X transfer buffer; diluted in 20% methanol from a 10X stock; 250 mM Tris Base, 1M Glycine. The gel was transferred to the activated PVDF membrane using a Mini Trans-Blot® cell (Bio Rad, 1703930) filled with 1X transfer buffer for 2.5 hr RT at 150 mA with an ice pack. The PVDF membrane was probed by western blotting (section 2.10).

2.8.2 Gradient gel electrophoresis

Gradient gels were used as an alternative to SDS PAGE gels to provide improved resolution of high molecular weight proteins (>100 kDa). Samples were prepared for loading by mixing 1:4 with NuPAGE™ LDS sample buffer (4X) (ThermoFisher Scientific, NP0007), supplemented with 50 mM DTT reducing agent and boiled at 91ºC for 5 min. Samples were loaded onto a NuPAGE™ 3 - 8% Tris-Acetate, 1.0 mm, mini protein gel, 10 well (Fisher Scientific, EA0375BOX) alongside a Hi-Mark™ pre-stained protein standard (Thermo Fischer, LC5699). The gel was placed into a XCell *SureLock*™ Mini-Cell (Fischer Scientific, EI0001) containing 1X NuPAGE™ Tris-Acetate SDS Running buffer; diluted from a 10X stock (Fisher Scientific, LA0041) and run for 1 hr at 150 V. The gel was then transferred to a PVDF membrane

in a 1X NuPAGE™ transfer buffer, as diluted in 10% methanol from a 20X stock (Fisher Scientific, NP0006) at RT for 2.5 hr at 150 mA. The PVDF membrane was probed by western blotting.

2.8.3 Native gel electrophoresis

Native gels were used as an alternative to SDS PAGE gels to investigate proteins under non-denaturing conditions. In preparation for loading, a maximum volume of 15 µL cell lysate was made up to a total volume of 20 µL by addition of 1x MNT lysis buffer, was mixed 1:1 with 2x Tris-Glycine native sample buffer (Fischer Scientific, LC2673). Samples were made up to a total volume of 30 µL with deionized water. Samples were loaded into chilled Novex™ 10% Tris-Glycine mini gels, WedgeWell™ format, 12-well gels (Fischer Scientific, XP00102BOX) alongside a NativeMark™ unstained protein standard (Fischer Scientific, LC0725). The gel was placed into a XCell *SureLock*™ Mini-Cell (Fischer Scientific, EI0001) containing an ice cold 1x Tris-Glycine native running buffer; diluted from a 10x stock (Fisher Scientific, LC2672). The gel was run for 60 min at 225 V at 4 ºC. Following running, the gel was immediately imaged with an Amersham Typhoon 500 gel imager; excitation 488 nm, emission 518 nm.

2.9 Coomassie Staining

The gel was fixed in a fixing solution comprised of; 5% acetic acid, 45% methanol, and 50% dH_2O, for 10 min RT with gentle shaking, then transferred to a colloidal Coomassie staining solution; 0.1% (w/v) Brilliant Blue G, 0.29 M H_3PO_4 and 16% $(NH_4)_2SO_4$ (Sigma Aldrich, B2025) overnight. Excess Coomassie was removed by soaking the gel in a de-stain solution; 10% acetic acid, 40% mL methanol, 50% mL dH_2O, for 10 min with gentle shaking. The gel was fixed at RT in a 25% methanol solution with gentle shaking before analysis.

2.10 Western Blotting

The PVDF membrane was blocked in 5% milk in TBST; pH 8, 10 mM Tris, 150 mM NaCl, supplemented with 0.1% Tween20 (VWR, 663684BP) at 4 ºC overnight. The membrane underwent 3 rounds of 5 min washes in TBST prior to a 1 hr incubation at RT with one of the following primary antibodies: type I collagen-UNLB raised in goat (Southern Biotech, 1310-01), mNG Tag raised in rabbit (Cell Signalling, 53061), mNG raised in mouse (Chromotek, 23f6-20), or β-actin (ProteinTech, 60008-1-Ig) raised in mouse. All antibodies were diluted 1:1000 in 5% milk in TBST.

After primary antibody incubation membranes underwent 5 x 5 min washes in TBST, prior to incubation with horseradish peroxidase conjugated secondary antibodies for 1 hr at RT. All secondary antibodies were diluted 1:3000 in 5% milk in TBST. SARPO (Aligent, D0306), RAGPO (Pierce, 31402), and GAMPO (Aligent, D0486) were used against primary antibodies raised in the relevant animal. Membranes underwent

4 x 5 min washes in TBST then were briefly dipped in TBS before reacting secondary antibodies with ECL (Amersham, RPN2209) and visualizing on film (Thermo Scientific, PI34090).

Following a first probe, the membranes were stripped of bound antibody by 2x 10 min washes in 1X stripping buffer (200 mM Glycine, 3.5 mM SDS, 1% (v/v) Tween20, pH 2.2), 2x 10 min washes in 1X PBS, and 2x 5 min washes in TBST. The stripped membrane was blocked in 5% milk in TBST at 4 ºC overnight and probed for β-actin to act as a loading control.

2.11 Immunofluorescence

Prior to fixation, cells were plated and transfected (section 2.4) on 16 mm round coverslips (Fischer Scientific, 12313138). Immediately before fixation, media was removed and cells were briefly washed in RT 1x PBS. Cells were fixed in 4% PFA, diluted in 1x PBS from a 16% (w/v) stock (Agar Scientific, AGR1026) for 10 min. Fixed cells were washed twice for 5 min in PBS before membrane permeabilization with 0.1% triton X 100 for 10 min. The cells underwent 3 x 5 min washes in 1x PBS before submersion in blocking solution; filtered 2% BSA, diluted in 1x PBS, for 30 min.

The coverslips were inverted onto parafilm in a foil covered incubation chamber with primary antibodies, overnight at 4ºC. Primary antibodies used were; P4HB [RL90] raised in mouse (ABCAM, ab2792) diluted 1:200 in blocking solution, or anti-alpha tubulin rabbit polyclonal (ab4074) diluted 1:100 in blocking solution. Following primary antibody incubation, coverslips were inverted into a fresh 12-well plate (TPP, 92012) to undergo 3 x 5 min washes in PBS. Coverslips were then inverted back onto the parafilm to incubate in the dark with Alexa Fluor 594 secondary antibodies diluted 1:500 in 2% BSA in PBS for 1 hr at RT. Donkey anti-rabbit (Invitrogen, A32740), and donkey anti-mouse (Invitrogen, A32744) secondary antibodies were used against primary antibodies raised in the relevant animal. Alternatively, the actin cytoskeleton was labelled with Alexa Fluor 568 phalloidin (Thermo Fischer, A12380) diluted 1:100 in blocking solution for 30 min RT.

Coverslips were placed back into the 12-well plate and underwent 2 x 5 min washes with PBS before being incubated with 4% DAPI for 10 min in the dark. Coverslips were briefly washed in PBS and placed face down onto microscope slides with soft-set Vectashield (Vector, H-1000). After drying for 10 min, the coverslips were sealed with nail varnish and stored in the dark at 4 ºC before imaging on a Zeiss 880 laser scanning confocal microscope.

2.12 Live Cell Imaging

2.12.1 Preparation for live imaging

Prior to imaging, cells were plated and transfected in 35 mm glass bottomed microscope dishes (section 2.4). The ER and PM were observed in real time during live cell imaging by the addition of 2 µL of 5

$mgmL^{-1}$ ER-Tracker™ blue-white (Fischer Scientific, E12353) for 20 min prior to imaging, or 2 µL of 5 $mgmL^{-1}$ CellMask™ Deep Red (Fischer Scientific, C10046) for 5 min prior to imaging, respectively.

Immediately prior to imaging, spent media was removed and the cells were briefly washed once in 1 mL RT PBS. The media was then replaced with 2 mL 37 ºC fluorobrite DMEM (Fischer Scientific, A1896701), supplemented with 100 μgmL^{-1} penicillin and 100 μgL^{-1} streptomycin, 10% glucamax and 10% FBS. Cells were imaged using a laser scanning confocal light microscope (Zeiss 880). During imaging cells were warmed to 37 ºC and exposed to 5% CO_2.

2.12.2 TIRF Imaging

Prior to imaging, cells were plated and transfected in 35 mm glass bottomed microscope dishes (section 2.4). Spent media was removed and the cells were briefly washed in 1x PBS, and placed in 2 mL warmed fluorobrite media. TIRF imaging was carried out in an Applied Precision OMX BLAZE Super-Resolution microscope (GE Healthcare). Prior to imaging the microscope was warmed to 37 ºC and CO_2 was increased to 5%. A 60X TRIF objective lens was used with 1514 oil, a BGR drawer, and conventional light path for TIRF microscopy.

2.13 Drug treatments and growth supplements

Cells were treated with the substances specified in table 1. The duration of drug treatment varied on an experiment-by-experiment basis as specified in results.

*Table 2.1 drug treatments. The name, working concentration and supplier of all drugs used to treat cells. *Some details of this product's use are not available due to P&G confidentiality.*

Substance	Manufacturer and Catalogue Number	Working Concentration
AA, Growth media	Sigma Aldrich, A7506	200 µM
ATPeptide*	P&G Ltd	2.5 ppm
BFA, Growth media	Sigma Aldrich, B5936	100 $ngmL^{-1}$
Colchicine, dH_2O	Sigma Aldrich, C9754	5 µM
CHX, 70% ethanol	Sigma Aldrich, C7698	200 µM
2-deoxy-d-glucose, dH_2O	Acros Organics, 111980010	50 µM
Lat B, dH_2O	Sigma Aldrich, L5288	5 µM
Sodium Azide, dH_2O	Sigma Aldrich, S2002	0.05%
Taxol, DMSO	Sigma Aldrich, PHL89806	5 µM
TET, 70% ethanol	Sigma Aldrich, T3383	1 $mgmL^{-1}$

2.14 Image analysis

All image data obtained by microscopy were analysed using Fiji (Schneider et al., 2012). Microscopy images were converted into figures for this thesis using the Fiji plugin 'QuickFigures' (Mazo, 2020).

2.14.1 Measurements

Vesicle diameter was measured by drawing a line across the vesicle and using the measure tool to obtain a calibrated measurement in microns. The area of a structure was calculated by drawing around it and measuring the resultant area. Cell and vesicle fluorescence were measured by selecting the area of interest with the selection tool and using the measure tool to obtain an average fluorescence, minimum and maximum fluorescence for the chosen area. The total number of certain structures or events were counted using the multi-point tool.

2.14.2 Colocalisation Analysis

Prior to colocalisation analysis, RGB images were split into component channels, and the unwanted channels closed. ROIs were selected based on biological context. The Fiji plugin Coloc 2 was used to perform Coste's regression to generate a 2D intensity histogram, calculate a Person's coefficient and perform Coste's significance test between the red and green channels of interest (Costes et al., 2004; Dunn et al., 2011).

2.14.3 Vesicle Movement Analysis and counting

Prior to measuring vesicle velocity, time lapse images obtained from the Zeiss 880 were thresholded in Fiji to obtain a black/white image with little background signal. Central regions of the cell which contained static structures were cropped out. The Fiji plugin TrackMate was used to provide quantitative data for mean velocity and displacement of particles within the cell, as well as a total count of collagen carriers (Tinevez et al., 2017). TrackMate2 software was calibrated using Zeiss image metadata. Intracellular structures were detected using the LoG detector. A blob diameter of 0.5 μm was chosen to detect structures of that size throughout the time lapse. A simple LAP detector was used to track the vesicle movement. Maximum linking distance and gap linking distance were selected between 1.5-0.5 μm based on the frame rate of the image and user discretion. Frame closing distance was set to 1. The results included the average velocity and displacement of all tracks identified within the time lapse. To calculate an average collagen carrier displacement and velocity for a given time lapse, the average displacement or velocity of all tracks identified in that cell were ordered from largest to smallest. The lowest 50% of values were then discarded to remove interference from static structures and user bias in thresholding. An average and standard error was calculated from the remaining values and determined to be the average velocity or displacement for that time lapse.

3 Designing a genetic construct to visualise collagen in living cells

3.1 Rationale

An mNG-COL1α2 genetic construct was designed based on a GFP-collagen1α2 construct used to study collagen deposition in zebrafish scar tissue formation (Morris et al., 2018; section 1.4). The construct used in this thesis uses the same design, with mNG in the place of GFP. mNG is a superior choice for a fluorescent tag due to its long half-life, pH stability, and increased brightness over GFP (Hostettler et al., 2017). A pNCS plasmid for the expression of mNG in bacteria was obtained as a positive control to be used in mNG assays.

3.2 Isolation, detection and characterization of mNeonGreen

To obtain a concentrated source of mNG, *E coli* were transformed with the pNCS plasmid. Single colonies of transformed bacteria were expanded in LB broth, then lysed by vortexing with glass beads. Glass beads were chosen as a lysis method over traditional detergent based lysis buffers to preserve the tertiary structure and fluorescent properties of mNG. Vortexing with glass beads had the potential to denature mNG through the generation of heat. To avoid potential heat damage to mNG, *E coli* were vortexed for 60 s, then placed on ice for 30 s. The number of 60 s vortex/30 s cooling periods were optimized to gain the most concentrated protein lysate, while ensuring enough bacterial lysis had occurred. After 6 rounds of 60s vortex/30 s cooling, a protein sample was taken and protein concentration measured by BCA assay. This was repeated until the sample had undergone 20 rounds of 60 s vortex/30 s cooling (figure 3.1 A). Six rounds of 60 s vortex/30 s cooling was found to be optimal.

The resulting bacterial lysates were centrifuged and the pellet discarded to obtain the proteins within the supernatant. The lysates contained a high concentration of mNG protein; which appeared yellow-green under while light, and emitted bright green fluorescence when excited by 488 nm blue light (figure 3.1 B-C).

To develop an mNG assay, and to test the specificity of commercial mNG antiboidies, a serial dilution of bacterial lysate (from 20 – 0.019 μg of protein) was prepared and separated by gel electrophoresis on two 8% SDS PAGE gels. The proteins in the gels were transferred to PVDF membranes and probed for mNG by western blotting. Two antibodies were compared for their ability to detect mNG: anti-mNG raised in rabbit from Cell Signalling Technologies, and anti-mNG raised in mouse from Chromo Tek. The antibodies were incubated with one of the membranes at 1:1000, in 5 % milk in TBST, for 1 hr RT. The Chromo Tek antibody was determined to be the better of the two, detecting as little as 0.078 μg of protein from a 30 s exposure, while the Cell Signalling antibody could only detect 0.313 μg after a 15 min exposure (figure 3.1 D). In subsequent western blotting experiments, 1.250 μg of bacterial lysate was used as a positive control with the Chromo Tek antibody.

A serial dilution of bacterial lysate was also separated by gel electrophoresis on a native tris-glycine gel, to retain the native conformation and fluorescent properties of mNeonGreen (Lau et al., 2018). The gel was scanned with 488 nm laser light in a Typhoon imager, with fluorescence detected with 0.156 µg of protein loaded (figure 3.1 E). The Typhoon imager calibrates to the strongest signal detected, so from this data, 0.156 µg of protein was chosen as a positive control in further studies.

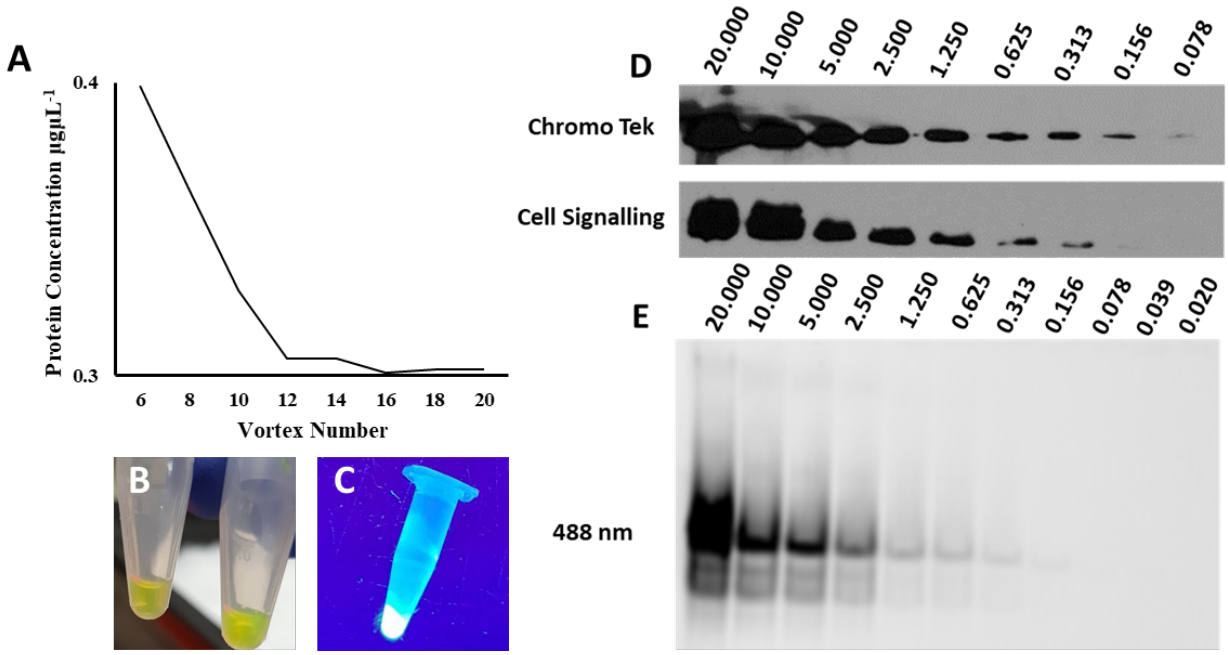

Figure 3.1 isolation and detection of mNG expressed by pNCS transformed E coli. (A) Graph showing total protein concentration, as determined by BCA assay, of pNCS transformed E coli lysate against number of 1 min vortexes with glass beads. (B) bacterial lysates under white light (C) bacterial lysate under 488 nm light. (D) western blot of pNCS transformed E coli lysate probed with Chromo Tek anti-mNG antibody with a 30s exposure, or Cell Signalling anti-mNG antibody with a 15 min exposure. (E) a serial dilution of pNCS transfected E coli lysates run on a native gel and excited under 488 nm light in a Typhoon gel imager. The numbers in (D-E) correspond to total weight of protein loaded in each well in micrograms.

3.3 Construct design, DNA sequence and plasmid design

Having characterised and detected mNG by gel electrophoresis, the mNG-COL1α2 fusion construct could be designed. As previously discussed, the fusion construct lacks the procollagen1α2 N terminal propeptide, telopeptide and cleavage domains, with mNG inserted immediately downstream of the signal peptide. GS linkers were inserted on either side of the mNG sequence to confer flexibility to the final protein (figure 3.2 A). DNA sequences for human collagen1α2, *Branchiostoma lenceolatum* mNG, and GS linkers were obtained from the National Centre for Biotechnology Information (ncbi.gov). The 5' end of the resulting DNA sequence has been colour coded according to the corresponding protein domains in fig 3.2 A (figure 3.2 B).

The DNA sequence for the mNG-COL1α2 fusion construct was translated *in silico* to identify any structural defaults or abnormalities. A primary amino acid sequence with one continuous open reading frame was translated from the DNA sequence (Gasteiger et al., 2003; figure 3.2 C). Phyre 2 was used to obtain a predicted tertiary structure for the mNG-COL1α2 construct (Kelley et al., 2015). The resultant N terminal of the protein was recognised in the Phyre2 database as mNG from *B lanceolatum*, and C terminal recognised as a human procollagen I triple helical domain, and has the typical coiled coil structure (figure 3.2 D).

After determining that the DNA sequence would code for the desired mNG-COL1α2 fusion protein; the sequence was incorporated into a plasmid. The plasmid was designed to be easily delivered and integrated into bacterial or mammalian genomes with standard transfection reagents and procedures. Three alternate plasmids were designed in pDRAW32, each with an alternative promoter to control expression (AcaClone Software, http://www.acaclone.com/). The CMV promoter allows for constitutive expression (Schlabach et al., 2010). The TET inducible promoter allows expression of mNG-COL1α2 by the addition of TET (Blau & Rossi, 1999). The native promoter allows expression of collagen in a similar fashion to that of endogenous collagen I in dermal fibroblasts.

All plasmids are just under 9000 base pairs (pb) and contain the same basic elements: the mNG-COL1α2 promoter (1-400 bp), the mNG-COL1α2 fusion construct DNA (400-5200 bp), SV40 late pA; a mammalian polyadenylation sequence to stop protein translation (5200-5600 bp). There is a CMV promoter from 5600-6200 bp to allow permanent expression of a DNA sequence between 6200-6600 bp for blasticidin resistance in mammalian cells, BGH pA, is a further mammalian polyA tail (6600-6800 bp). The pUC origin of replication (7600-7400 bp) allows for a high copy number when expressed by bacterial cells, allowing the plasmid to be amplified by maxi prep. An ampicillin resistance gene (8600-7800 bp) permits selection for plasmid expression in bacteria (figure 3.2 E). The plasmids were manufactured by vector builder (Vector Builder Inc, https://en.vectorbuilder.com/).

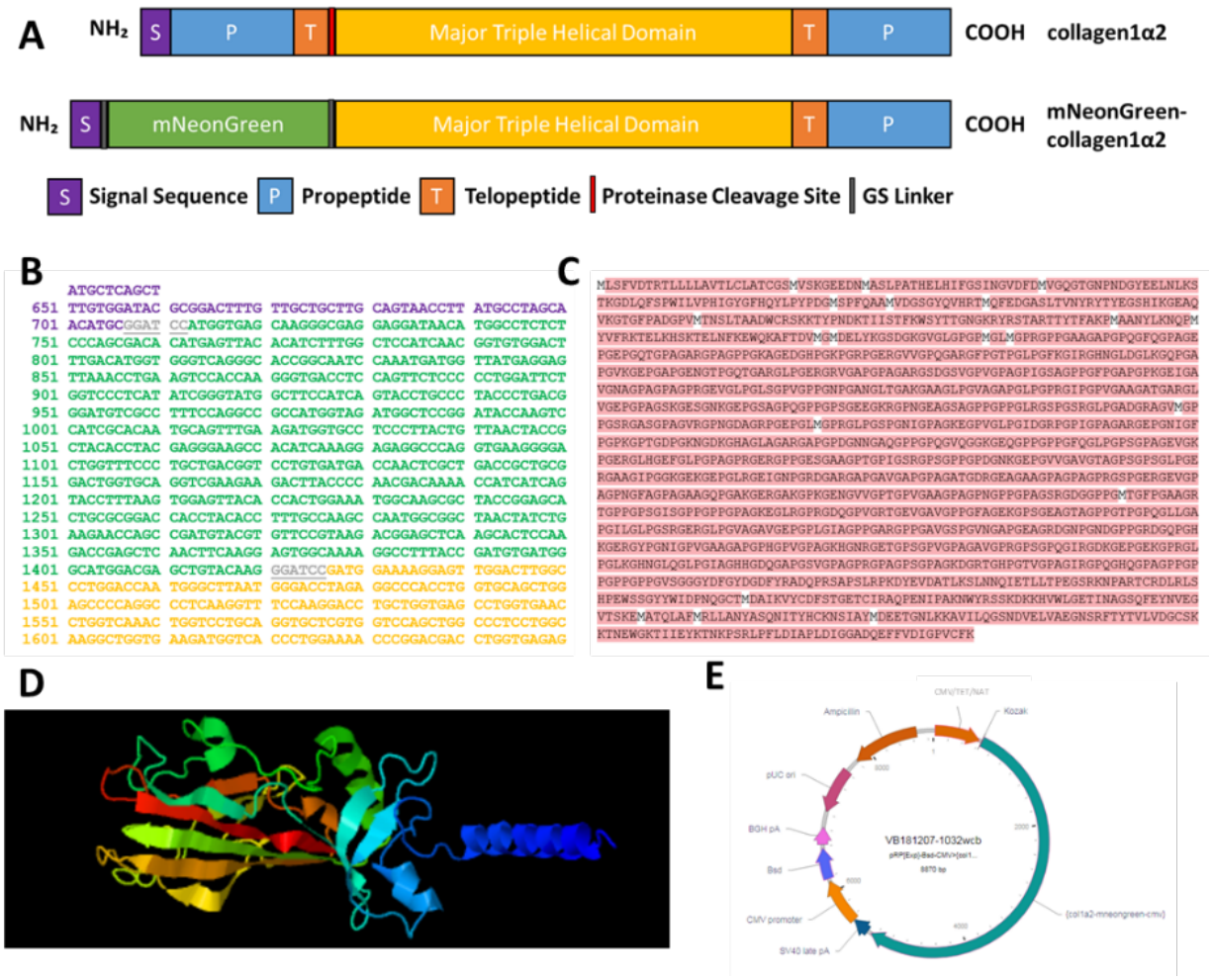

Figure 3.2 design of the mNG-COL1α2 construct. (A) the mNG fluorophore is inserted at the N terminal end of collagen1α2 in a fashion which omits the propeptides and telopeptide, GS linkers flank the inserted mNG protein in order to provide flexibility. (B) The 5' end of DNA designed to encode for the mNG-COL1α2 protein, DNA for signal peptide is in purple, GS linkers in grey, mNG in green, and major triple helical domain in yellow. (C) The DNA sequence was translated in silico to provide a full peptide sequence for the encoded mNG-COL1α2 protein shown in A. (D) A 3D structure of the primary peptide sequence in A and C predicted by Phyre2. (E) plasmid design for expression of the mNG-COL1α2 construct. Images in part B and E by Dr Max Brown.

3.4 Preliminary Data

Preliminary data, obtained by Dr Max Brown, showed that HT1080 cells transfected with the CMV promoter driven mNG-COL1α2 construct express mNG. The mNG signal was observed to be distributed throughout the cell in a fashion indicative of collagen I movement through the cell secretory pathway. HT1080 cells expressing CMV promoter driven mNG-COL1α2 were treated with P&G active ingredients (restricted information), or left untreated to act as a control, and live imaged by laser scanning confocal microscopy. This showed that bioactive treated cells had a significantly increased number of collagen vesicles present within the cell, as determined by one-way ANOVA. This indicated that in the presence of bioactives, collagen production and secretion increased.

4 Expressing mNG-COL1α2 in live fibrosarcoma and fibroblast cell lines

4.1 Rationale

Once the plasmid encoding mNG-COL1α2 had been created, its expression patterns and behaviour when introduced to cells of interest were characterised. mNG-COL1α2 expression in three immortalised cell lines of interest was characterised: the HT1080 fibrosarcoma cell line, the BJ hTERT dermal fibroblast cell line, and the Saos-2 osteosarcoma cell line. The HT1080 cells were chosen as a fast growing cell line in which to do preliminary experiments. The BJ hTERT and Saos-2 cell lines are professional collagen secreting cell lines, and can be used to study collagen deposition. Transfection of the plasmid into BJ hTERT cells was optimised in order to find a transfection reagent which would result in the highest rate of transfection, while causing the least amount of cell death (Rose, 2003). Once a transfection reagent had been chosen, live transfected cells were imaged to observe the distribution of mNG within the cell, and the dynamics of the mNG movement.

4.2 Optimising transfection of HT1080 and BJ hTERT cell lines

In order to optimise the transfection of BJ hTERT cells, both cell lines were grown on coverslips and transfected with the CMV promotor driven mNG-COL1α2 construct and the native promotor driven mNG-COL1α2 construct BJ hTERT only using a range of different transfection reagents. The transfection of HT1080 cells had been optimised by Dr Max Brown prior to this research, so HT1080 cells transfected with JetPEI were used as a positive control in this experiment. Twenty-four hours after transfection the cells were fixed in 4% PFA, the cell membranes permeabilized with Triton X100, and the nucleus stained with DAPI. The cells were then imaged on the Zeiss 880 laser scanning confocal microscope.

Low magnification photographs were taken of a field of cells at five randomly selected locations across the coverslip. The total number of cells in each image was counted using DAPI staining and the number of transfected cells was counted using the presence of significant 512 nm emission signal. The total cell count and transfected cell count were averaged across all five images. The resultant averages were used to calculate a percentage efficiency for each transfection reagent.

Expression of mNG-COL1α2 was lower under the native promoter compared to the CMV promoter, regardless of transfection reagent, due to a lower expression potential from the native promotor compared to the CMV promotor. The efficiency of each transfection reagent was therefore judged on transfection of CMV rather than native promotor driven mNG-COL1α2. A transfection reagent was considered to have a good transfection efficiency if it transfected >50% of the cells. From the criteria JetPRIME, JetOPTIMUS, and Altogen BJ transfection reagent were considered to have good BJ hTERT transfection efficiencies (table 4.1).

Table 4.1 transfection efficiency of CMV and native promoter driven mNG-COL1α2 in HT1080 and BJ hTERT cell lines with different transfection reagents, averaged over five repeats.

Transfection reagent and cell type	Percentage transfection efficiency with CMV promoter	Percentage transfection efficiency with native promoter	Suitable as a transfection reagent
HT1080 JetPEI	51	N/A	Yes
BJ hTERT JetPEI	37	47	No
BJ hTERT JetPRIME	62	43	No
BJ hTERT JetOPTIMUS	61	59	No
BJ hTERT Altogen	70	60	Yes

A good transfection reagent also needs to avoid causing cell death during transfection. To determine the overall health of the cells, five high magnification photographs were taken of individual cells transfected with each reagent. A representative image of cells transfected with the CMV promotor driven mNG-COL1α2 construct was selected for each transfection reagent (figure 4.1). The HT1080 cells transfected with JetPEI retain a similar size and morphology to the untransfected HT1080 cells, indicating that the JetPEI transfection reagent has few adverse effects on this cell line and overall cell health..

BJ hTERT cells transfected with JetPEI and Altogen BJ transfection reagent retained a morphology typical of untransfected BJ hTERT cells. BJ hTERT cells transfected with Jet PRIME or JetOPTIMUS were generally much smaller and had a rounded morphology. JetPRIME and JetOPTIMUS transfected cells had a granular distribution of collagen and were considerably more sparsely populated than control cells, indicating cell death had occurred. In order to maximise transfection efficiency and minimise cell death, Altogen BJ transfection reagent was used in all further experiments.

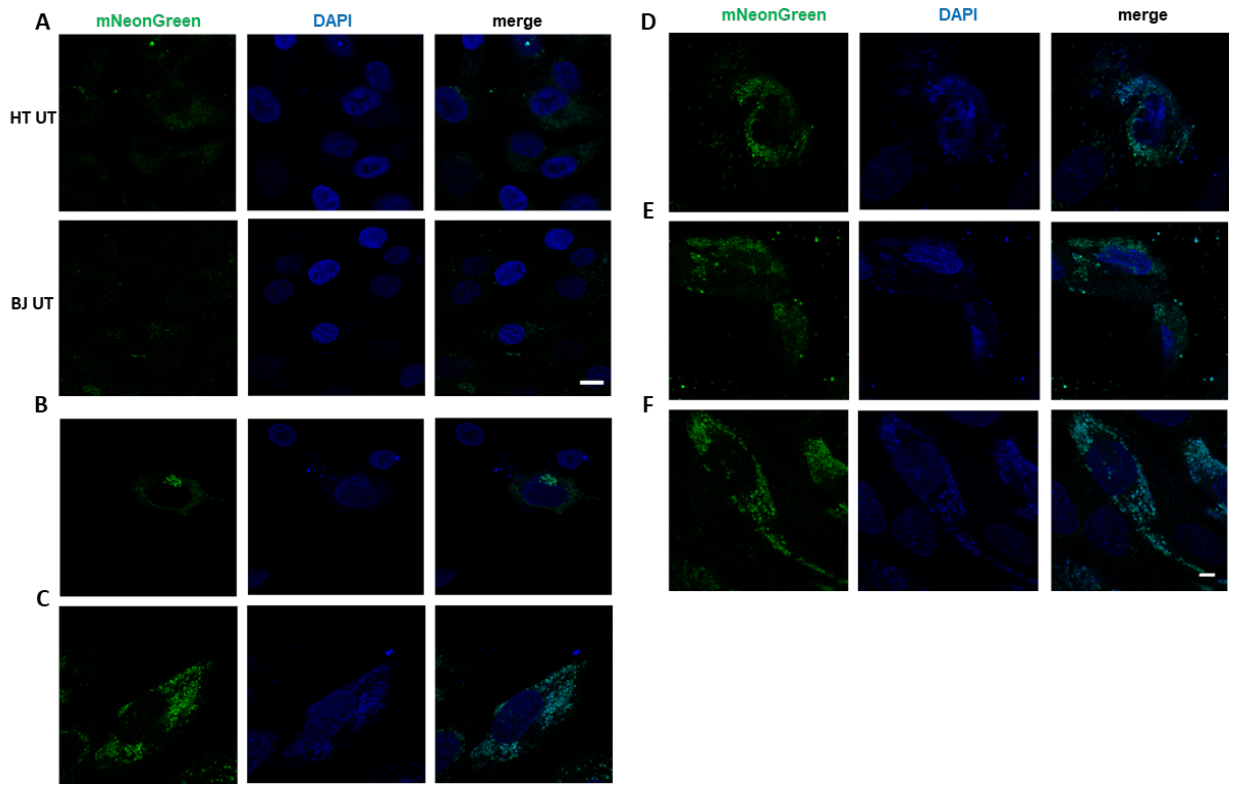

Figure 4.1 optimisation of HT1080 and BJ hTERT transfection with mNG-COL1α2. Images of HT1080 and BJ hTERT cells transfected with the CMV promoter controlled mNG-COL1α2 construct (green), fixed and DAPI stained (blue), before being imaged by confocal microscopy. Panel (A) UT HT1080 and UT BJ hTERT. Scale bar 10 µm. Panel (B) HT1080 transfected with JetPEI. Panel (C) BJ hTERT transfected with JetPEI. Panel (D) BJ hTERT transfected with JetPRIME. (E) BJ hTERT transfected with JetOPTIMUS. Panel (F) BJ hTERT transfected with Altogen transfection reagent. Scale bar 5 µm.

4.3 Characterising mNG-COL1α2 expression in HT1080 fibrosarcoma and BJ hTERT fibroblasts and Saos-2 osteosarcoma

The distribution and dynamics of mNG-COL1α2 in both cell lines of interest was analysed. Live HT1080, Saos-2, and BJ hTERT cells were transfected with CMV promoter driven mNG-COL1α2 and imaged with 488 nm laser light for 50 continuous frames. The first frame of each movie was used to compare typical mNG-COL1α2 distribution throughout the cell (figure 4.2 A). A hyperstack of all 50 recorded frames was generated, in which mNG-collagen signal from each frame was superimposed onto one image and assigned a different colour according to which frame the signal was from, to give an indication of collagen dynamics over the recorded 50 frames (figure 4.2 A). Structures in white are static, while a trail of colour indicates a dynamic structure.

In HT1080, a large, static perinuclear structure was observed. Regions of the structure with weaker mNG signal is likely to be the ER and the central region with a high mNG signal is likely to be the ERGIC. In the HT1080 cell periphery a large number of, small, highly dynamic structures were found, identified as

collagen vesicles. The vesicles have an average speed of 0.45 μms^{-1} as determined by the Fiji plugin TrackMate. Similar to the HT1080 cells, the Saos-2 cells were observed to have a number of static structures within the centre of the cell. There were fewer collagen vesicles observed in the Saos-2 cells compared to the HT1080 cells. In the Saos-2 cells the vesicles are found in the cell periphery where they are highly mobile, and have an area of approximately 0.5 μm^2. The average speed of the Soas-2 collagen vesicles was determined to be 0.3 μms^{-1} using TrackMate. ER, ERGIC and Golgi structures were absent from the BJ hTERT cells. Collagen was observed in larger, static vesicles throughout the cytoplasm. Average vesicle area, as determined in Fiji, was almost 3 times larger in BJ hTERTs (1.5 μm^2) compared to HT1080 or Saos-2 cells (0.5 μm^2).

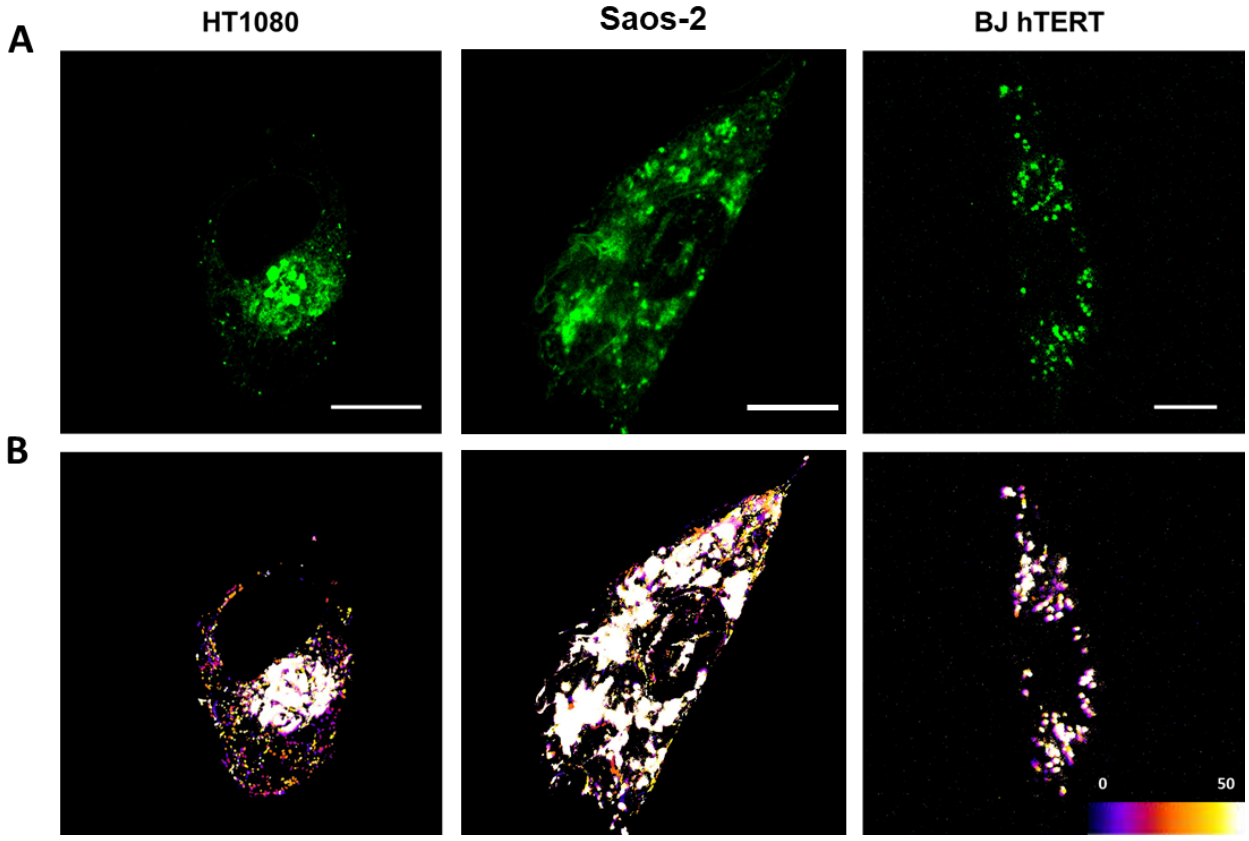

Figure 4.2 morphology and dynamics of mNG-COL1α2 in cell lines of interest. HT1080, Saos-2 and BJ hTERT cells transfected with the CMV promoter driven mNG-COL1α2 construct. Panel (A) the first frame of a 50 frame movie of an HT1080 cell, Saos-2 cell, and a BJ hTERT cell, expressing mNG-COL1α2 (green) to show the overall distribution of collagen throughout the cell. Scale bar 10 µm. Panel (B) all 50 frames in each image from (A) were combined into a hyperstack and given a colour depending on the frame number (scale bottom right).

FRAP was used to further assess the dynamics of collagen vesicles in an HT1080 cell expressing CMV promoter driven mNG-COL1α2 (Lippincott-Schwartz et al., 2018). In this experiment a small area of the cell periphery, highlighted in red, was photobleached with a short exposure to high intensity 488 nm laser in the course of 1 frame (figure 4.3 A). Following photobleaching, the cell was observed by time lapse

imaging for 5 min (figure 4.3 B). This allowed observation of mNG dynamics in the photobleached region and a control region, highlighted in grey (figure 4.3 A). The average fluorescence of the photobleached area in each frame (red), for 300 frames was plotted against the average fluorescence of a control region (grey) (figure 4.3 C). A total vesicle count was also obtained for both the control area and photobleached area in every frame and plotted against time (figure 4.3 D).

Between 2-50 s the average fluorescence intensity of the photobleached area gradually increased, despite the absence of vesicles from the region. Once vesicles re-entered the photobleached area, the average fluorescence began to fluctuate while increasing. Spikes in overall vesicle counts directly corresponded to sharp increases in average fluorescence, due to the higher fluorescence intensity of vesicles compared to the ER. After 500 s, there are the same number of vesicles in the photobleached area as there were in frame 1, with vesicle movement having completely recovered to regular levels by 200 s. However, the average fluorescence of the photobleached area did not reach the same level as the control or as in frame 1 by 500 s, implying that this experiment time was not enough to allow full recovery of fluorescence in the area. The control region of the cell shows that this result cannot be explained by overall photobleaching of the total fluorophore.

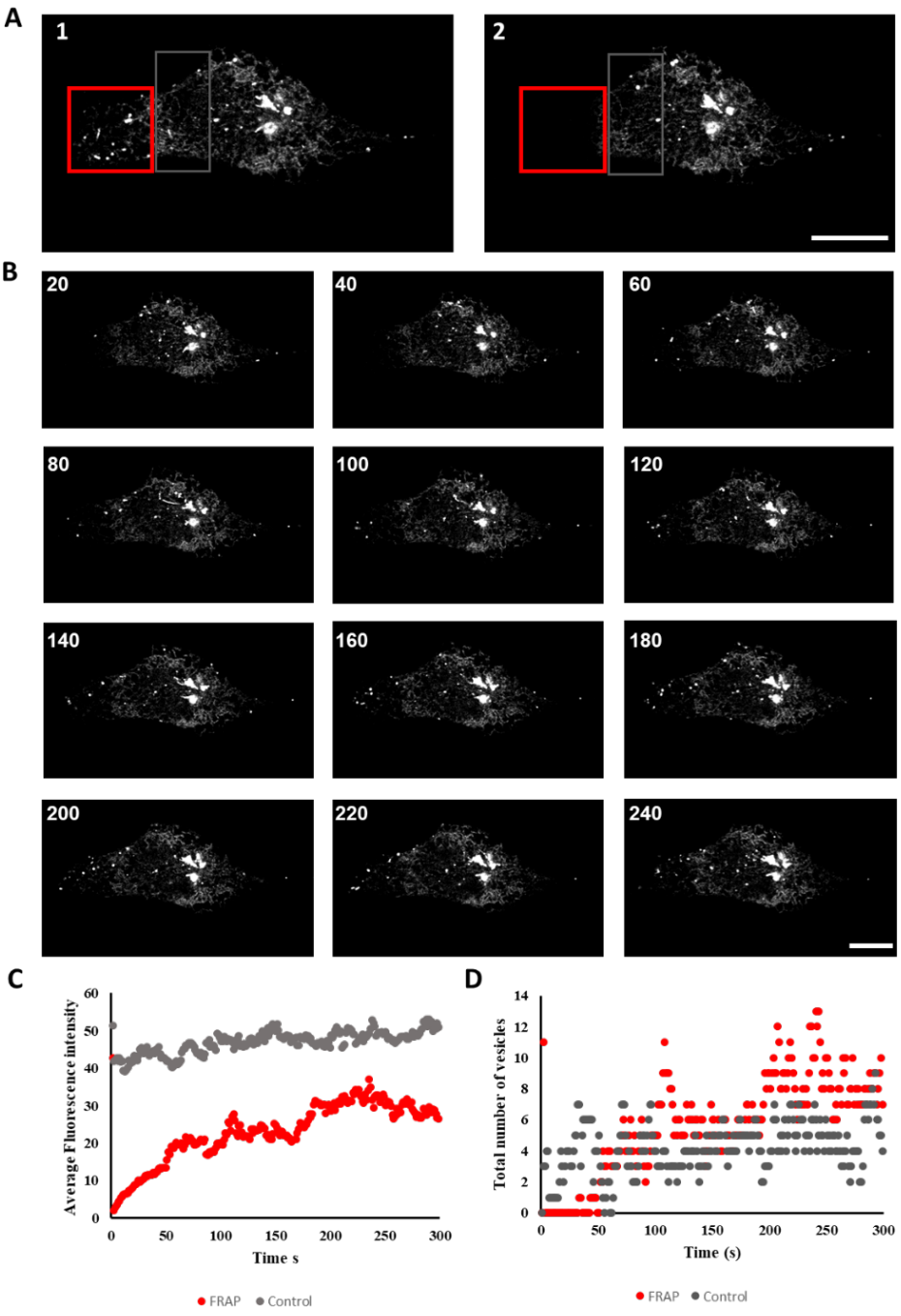

Figure 4.3 investigating the dynamics of mNG-COL1α2 movement. FRAP experiment on an HT1080 cell expressing CMV promoter driven mNG-COL1α2. A chosen cell was imaged for 242 frames, at a frame rate of 2.06 sframe^{-1}, giving a total imaging time of 500 s. Panel (A) frame 1 and 2 of FRAP time lapse of an HT1080 cell expressing CMV promoter driven mNG-COL1α2. An area exposed to a brief burst of high laser is marked in red. A control region of the same area, not affected by the laser is marked in grey. Scale bar 10 µm. Panel (B) every 20 frames of the cell from (A) recovering after photobleaching. Scale bar 10 µm. (C) the average fluorescence of the photobleached and control areas are recorded in each frame and plotted against time in seconds. (D) the total number of vesicles in the control and photobleached area is recorded in every frame using TrackMate and plotted against time in seconds. FRAP performed by Dr Tim Hawkins.

4.4 Time course of mNG-COL1α2 expression

To characterise the time taken by HT1080 cells to synthesise and secrete mNG-COL1α2, HT1080 cells were transfected with the TET inducible mNG-COL1α2 construct. The cells were placed in fluorobrite media 24 hr after transfection and treated with TET on the Zeiss 880 laser scanning confocal microscope. After the addition of TET, the cells were imaged at a low magnification for 50 frames, at a frame rate of 3.33 s, every 30 min for 3 hr (figure 4.4).

mNG-COL1α2 synthesis began between 30 and 75 min after the addition of TET. The ERs of multiple cells were observed slowly filling with mNG fluorescence during this time (figure 4.4 A-C). Between 90 and 165 min after the addition of TET, the cells began to package newly synthesised collagen into secretory vesicles, which were observed in the cell periphery (figure 4.4 D-F). Single cells were imaged at a higher magnification 85 and 185 min after TET addition (figure 4.4 G and H, respectively). These cells were representative of the typical cellular morphology at those time points after the addition of TET. After 85 min of induction, the perinuclear ER was filled, with few secretory vesicles present in the cell periphery (figure 4.4 G). After 165 min the ER was brighter and occupied a larger area of the cell with bright secretory vesicles observed in the cell periphery (figure 4.4 H).

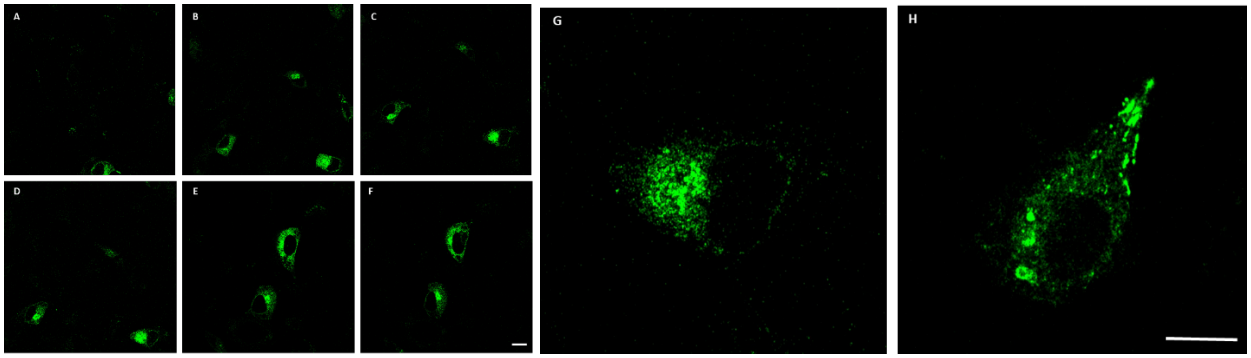

Figure 4.4 TET induction of mNG-COL1α2 in HT1080 cells. HT1080 cells transfected with the TET inducible promoter were treated with TET and imaged for 50 frames every 30 min. The first frame of each image is shown for (a) 0 – 15 min, (b) 30 – 45 min, (c) 60 – 75 min, (d) 90 – 105 min, (e) 120 – 135 min, (f) 150 – 165 min. Scale bar 10 µm. Single cells were imaged at a higher magnification after (g) 85 min, and (h) 185 min. Scale bar 20 µm.

4.5 Discussion

In order to characterise collagen expression from three immortalised cell lines of interest: HT1080 fibrosarcoma, BJ hTERT dermal fibroblasts, and Saos-2 osteosarcoma, the mechanism of transfection was firstly optimised. Lipid based transfection reagents were chosen over viral reagents or electroporation because of their high transfection efficiency, survival rate, and low risk of inducing off-target mutations (M. Lee et al., 2017). JetPEI had been determined as optimal for HT1080 transfection prior to this project by Dr Max Brown (section 3.4). Lipafectamine 3000 is widely used for transfection of Saos-2, and therefore also did not require optimisation (Z. Chen et al., 2017; M. Wang et al., 2017). The transfection reagent for

BJ hTERT cells was optimised and determined to be BJ transfection reagent, specially designed by Altogen (figure 4.1; table 4.1). Despite preventative measures, cell death was observed in all three cell lines following transfection, likely due to overproduction of collagen causing toxicity to the cells (Kumar et al., 2019).

To observe the intracellular distribution of mNG-COL1α2 expressed by each cell line of interest, one cell from each line was continuously imaged for 50 frames by confocal microscopy. The HT1080 cells and Saos-2 cells have very similar sized collagen vesicles, and the average velocity of these was similar for both cell lines. The BJ hTERT cells had a very different intracellular distribution of collagen, with collagen found in large, static structures throughout the cell (figure 4.2). In order to determine if these results were aberrant or standard, an immunofluorescence experiment should have been done to stain endogenous collagen I in non-transfected, wildtype cells. This would have provided insights into the native distribution of collagen throughout the cell and would have provided an indication if mNG-COL1α2 was found in aberrant locations.

The dynamics of mNG-COL1α2 were further investigated in HT1080 cells using FRAP (figure 4.3 A-B). Following photobleaching there was a slow overall increase in the average fluorescence intensity, compared to the control region. Although some fluctuations in fluorescence intensity occurred, this was determined to be due to the presence of collagen vesicles, which are highly mobile and have a high fluorescence intensity compared to the surrounding cell. The number of vesicles counted in each frame directly corresponded to average fluorescence fluctuations. Although vesicle number fully recovered over the time course of the FRAP experiment, the average fluorescence of the photobleached area did not. Background mNG-COL1α2 fluorescence might be achieved by the refilling of ER with collagen, which did not fully occur within the time course of this experiment. A further experiment using an ER tracker would be needed to confirm this theory, but could lead to interesting investigation of collagen dynamics within the ER.

An experiment using TET induction to observe the time course over which mNG-COL1α2 is expressed revealed that expression occurs over a period of 3 hr following induction. By this time the HT1080 cells had a similar morphology as the HT1080 cell from figure 4.2 A. This shows that the cell is able to produce and traffic collagen very rapidly through the secretory pathway. This rapid production and secretion might be important for the cells survival, by allowing quick changes to collagen production in response to external and internal stimuli. It important for example that collagen is quickly produced following wounding in order to allow a scar tissue to form and prevent further damage from being done to the tissue (Bainbridge, 2013; Zhao et al., 2017). Although current research suggests that *in vivo* collagen production may be much slower than this (Chang et al., 2020).

5 Identifying suitable controls for mNG-COL1α2

5.1 Rationale

In order to act as a robust and reproducible tool to study collagen trafficking, expression of the mNG-COL1α2 construct must be controlled for. The construct must retain the mNG tag fused to collagen I at all stages of trafficking. The mNG tag should not significantly alter the trafficking of collagen through the ER, Golgi, and post-Golgi stages of the secretory pathway. If these conditions are met, the mNG-collagen construct can be considered a valid, robust tool with which to study collagen trafficking.

5.2 mNG is retained on collagen1α2 expressed by transfected cells

To ensure that the mNG visualised in the microscopy studies is attached to collagen1α2, HT1080 and BJ hTERT cells were transfected with the mNG-COL1α2 construct under control of TET inducible, CMV and native (BJ hTERT only) promoters. The cells were lysed in 1x MNT buffer, to ensure that the tertiary structure and fluorescent properties of mNG would be retained within the lysate. Ten micrograms of each of the resultant lysates were separated by gel electrophoresis on an 8% SDS PAGE gel or native tris-glycine gel, alongside a pNCS transformed *E coli* lysate to act as a positive control for mNG. The SDS PAGE gel was transferred to a PVDF membrane and probed for collagen I and the native gel was scanned by 488 nm laser to detect the presence of fluorescent mNG bands in the gel (Lau et al., 2018).

Collagen I was absent from the UT HT1080 negative control, an expected result as HT1080 cells do not express this protein. A band of approx. 150 kDa, with less abundant molecular weight break down products below, was present in both the CMV and TET HT1080 cells. The UT BJ hTERT cells had a conventional collagen I band pattern: a collagen1α1 band at 200 kDa and a collagen1α2 band at 150 kDa, and less abundant isoforms at lower molecular weight (Iannarone et al., 2019). The CMV, TET and NAT BJ hTERT cells expressed less collagen1α2 than the UT BJ hTERT cells, and almost no collagen1α1 at all (figure 5.1 A). On the native gel, mNG was strongly detected in the *E coli* positive control at a low molecular weight. A high molecular weight fluorescent signal, likely to be mNG-COL1α2, was found in the CMV and TET HT1080 cells, but not in any of the BJ hTERT cells (figure 5.1 B).

Due to the low expression of mNG-COL1α2 by BJ hTERT cells, collagen I production in the professional collagen secreting Saos-2 cell line was also investigated, by comparing UT and CMV Saos-2 lysates on an 8% SDS PAGE gel alongside HT1080 and BJ hTERT lysates. The Saos-2 cells have a similar collagen I banding pattern to BJ hTERT cells (Fernandes et al., 2007; Rodan et al., 1987). Unlike the BJ hTERT cells, transfection with mNG-COL1α2 did not affect the expression of endogenous collagen in Saos2 cells, as the banding pattern following western blotting for collagen I remained the same in UT and CMV Saos2 lysates. Following western blotting for collagen I, the membrane was stripped and re-probed for mNG. The mNG Cell Signalling antibody bound non-specifically with a number of proteins expressed by all cell types,

including the UT HT1080, Saos-2 and BJ hTERT cells. In the CMV and TET HT1080 and CMV Saos2 lysates a band with a higher signal intensity was observed at 150 kDa, the same molecular weight as Col1α2. This experiment indicated the presence of mNG-COL1α2 in these lysates (figure 5.1 C).

Lysates from UT and CMV HT1080 and Saos2 cells were separated by electrophoresis on a native tris-glycine gel. When scanned with 488 nm laser, high molecular weight bands were detected in the CMV but not UT lysates. The bands had a higher molecular weight than the band for mNG in the positive control (figure 5.1 D). This data provides evidence that mNG is retained on collagen1α2 expressed by HT1080 and Saos-2 cells following transfection with the CMV promoter driven mNG-COL1α2 construct in both lines, and TET inducible cell line in HT1080.

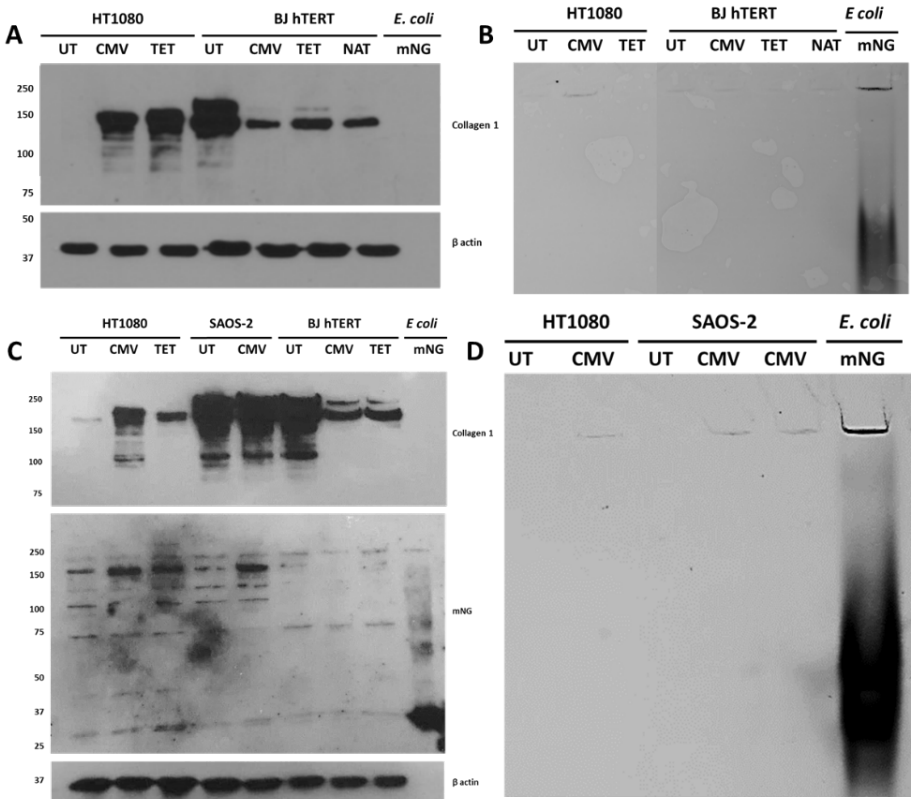

Figure 5.1 retention of mNG on collagen1α2 expressed by transfected cells. Cells were untransfected (UT), transfected with CMV promoter driven mNG-COL1α2 (CMV) TET inducible mNG-COL1α2 and induced for 8 hr (TET) or native promoter driven mNG-COL1α2 (NAT) 24 hr before lysis in 1x MNT buffer. pNCS transformed E coli lysate acted as a positive control for mNG (mNG). (A) Ten micrograms of protein from cell lysates were denatured by boiling with DTT and separated by gel electrophoresis on an 8% SDS PAGE gel, transferred to a PVDF membrane and probed by western blotting for collagen 1, and β-actin loading control. (B) 10 µg of protein from cell lysates separated by gel electrophoresis on native tris-glycine gel and scanned with 488 nm laser using a Typhoon gel imager. (C) 10 µg of protein from cell lysates were denatured by boiling with DTT separated by electrophoresis on an 8% SDS PAGE gel, transferred to a PVDF membrane and probed for collagen I, and mNG by western blotting, with β-actin loading control. (D) 10 µg cell lysates separated by gel electrophoresis on a native tris-glycine gel and scanned with 488 nm laser using a Typhoon gel imager. Experiment was repeated in triplicate.

5.3 mNG is co-translationally secreted into the ER

The primary amino acid sequence of procollagen1α2 contains a N terminal signal peptide to facilitate its co-translational secretion into the ER (Choo et al., 2009). In order to ensure that mNG-COL1α2 acts as a biologically relevant tool to study collagen trafficking, the addition of the mNG in the N terminus of the protein should not affect co-translation of collagen into the ER (Section 1.2.1).

To test this, HT1080 cells expressing CMV promoter driven mNG-COL1α2 were left untreated as a control group, or treated for 4 hr with 200 μM CHX. CHX acts upon ribosomes to block protein translation from mRNA (Schneider-poetsch et al., 2010). Following CHX treatment, the cells were fixed in 4% PFA, stained for the ER resident protein P4HB (PDI) by immunofluorescence, and nuclei stained with DAPI.

Treatment for 4 hr with CHX resulted in decreased mNG-COL1α2 from both the ER and cell periphery, when compared to the control cells. Some mNG can be seen in the periphery of the CHX treated cells, showing that the transfection was successful, and that lack of mNG signal was due to CHX treatment (figure 5.2 A).

To observe the dynamics of collagen vesicle movement following treatment with CHX, HT1080 cells expressing CMV promoter driven mNG-COL1α2 were stained with ER tracker blue, in order to observe the ER dynamics. Three HT1080 cells were imaged for 50 frames prior to, and every 10 min after the addition of 200 μM CHX for a total of 60 min. The timescale of this experiment was too short to see a decrease in mNG-COL1α2 presence in the cell periphery or ER (figure 5.2 B). Although it is expected that over a longer imaging time of 4 hr, mNG intensity in the cell would decrease. Further experimentation using longer imaging times should be done to confirm this. The time lapse movies obtained of each of the three cells at 0, 30, and 60 min after the addition of CHX were analysed using TrackMate to quantify the movement of post-Golgi collagen carriers. An average across all 3 repeats showed a decrease in average velocity and displacement of vesicles (figure 5.2 C-D). However, in the absence of a longer time course experiment, it is unclear if this is caused by decreased collagen synthesis, or overall decrease in cell health.

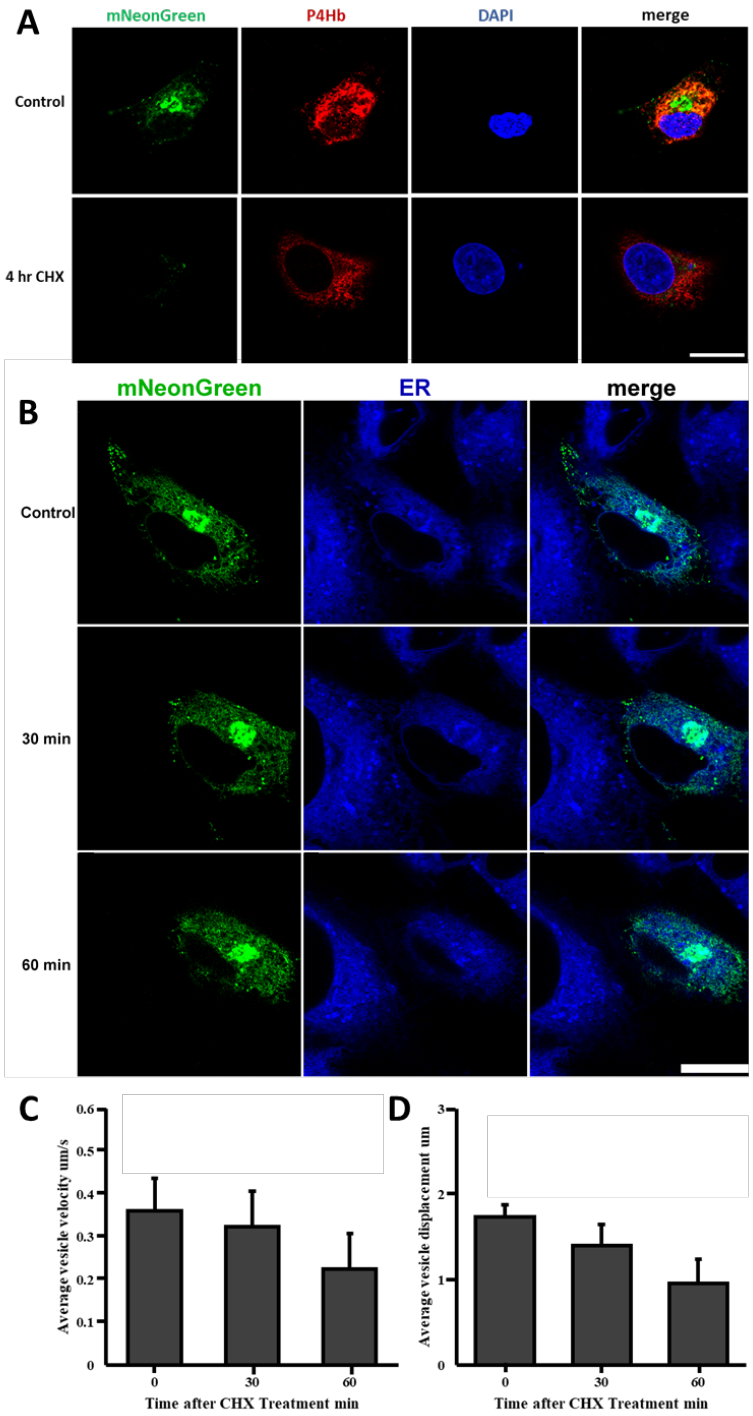

Figure 5.2 treatment with CHX results in a decrease in mNG-COL1α2 expression. Panel (A) HT1080 cells expressing CMV promoter controlled mNG-COL1α2 (green) were left untreated or treated for 4 hr with CHX prior to fixation in 4% PFA. The ER resident protein PDI was stained by immunofluorescence (red) and the nucleus was stained with DAPI (blue). Scale bar = 20 µm. Panel (B) HT1080 cell expressing the CMV promoter driven mNG-COL1α2 construct (green) were stained with ER-tracker blue-white (blue) frame 1 of 50-frame time lapse movies taken at 0 min, 30 min, and 60 min after the addition of 200 µM CHX. Scale bar, 20 µm. Vesicle movement in the 50 frame movies for 0, 30, and 60 min was quantified using Fiji plugin TrackMate for 3 cells. (C) average vesicle velocity over time, with standard error bars. (D) average vesicle displacement over time, with standard error bars.

5.4 mNG-COL1α2 is trafficked through ER

Native procollagen I is co-translationally inserted into the ER, where it undergoes extensive and essential modifications such as trimerisation, triple helix formation, and proline hydroxylation. In the ER, mNG-COL1α2 will be able to interact with key ER resident chaperones to ensure correct folding and function prior to exit (Section 1.2.1). To determine if mNG-COL1α2 is trafficked from the ER as expected, cells were treated with BFA, a drug which inhibits the exit of proteins from the ER. HT1080 cells expressing CMV promoter driven mNG-COL1α2 were untreated or treated with 100 $ngmL^{-1}$ BFA for 1 hr (Chardin & Mccormick, 1999). The cells were fixed in 4% PFA and stained by immunofluorescence for ER resident protein PDI and with the nuclear stain DAPI, then imaged by confocal microscopy.

The BFA treated cells show and increased colocalisation of mNG-COL1α2 with PDI, indicating retention of mNG-COL1α2 within the ER (figure 5.3 A). The Fiji plugin Coloc2 was used to quantify the colocalisation between the two channels in the Z stacks obtained from each cell imaged. This showed that there was a statistically significant increase in colocalisation between mNG and PDI following treatment with BFA (figure 5.3 B-C). This was further shown with Pearson's R value; a value of 0.26 was calculated for the control cells, showing that there is a slight colocalisation between red and green channels within the cell. This corresponds to the images obtained, with a small amount of mNG-COL1α2 found in the ER, but the majority of mNG found throughout the cell periphery. Pearson's R value for the BFA treated cell was 0.96, showing an almost perfect colocalisation between mNG and PDI, indicating that nearly all mNG-COL1α2 in this cell is localised to the ER (Dunn et al., 2011). Coste's P value for both results is 1.00, showing that both results are statistically significant (Costes et al., 2004). This shows that BFA treatment results in a significantly increased retention of mNG-COL1α2 within the ER and loss of mNG-COL1α2 from the Golgi. Therefore, mNG-COL1α2 is translated into the ER and moves from ER to Golgi, in a similar fashion to native collagen.

To observe the dynamics of vesicle movement following treatment with BFA, HT1080 cells expressing CMV promoter driven mNG-COL1α2 were stained with ER tracker blue, in order to observe the ER dynamics. Three HT1080 cells were imaged for 50 frames prior to, and every 5 min after the addition of 100 $ngmL^{-1}$ BFA for 45 min. Images at 0, 25, and 45 min after the addition of BFA show that the colocalisation of ER and mNG-COL1α2 increased over this time, similar to the fixed cells (figure 5.3 D). The time lapse movies of three cells obtained at 0, 25 and 45 min after the addition of BFA were analysed using TrackMate to quantify the dynamics of post-Golgi carriers. An average across all three repeats shows that there was a decrease in both average vesicle velocity and vesicle displacement although this was not statistically significant (figure 5.3 E-F). Treatment with BFA therefore did not affect vesicle dynamics.

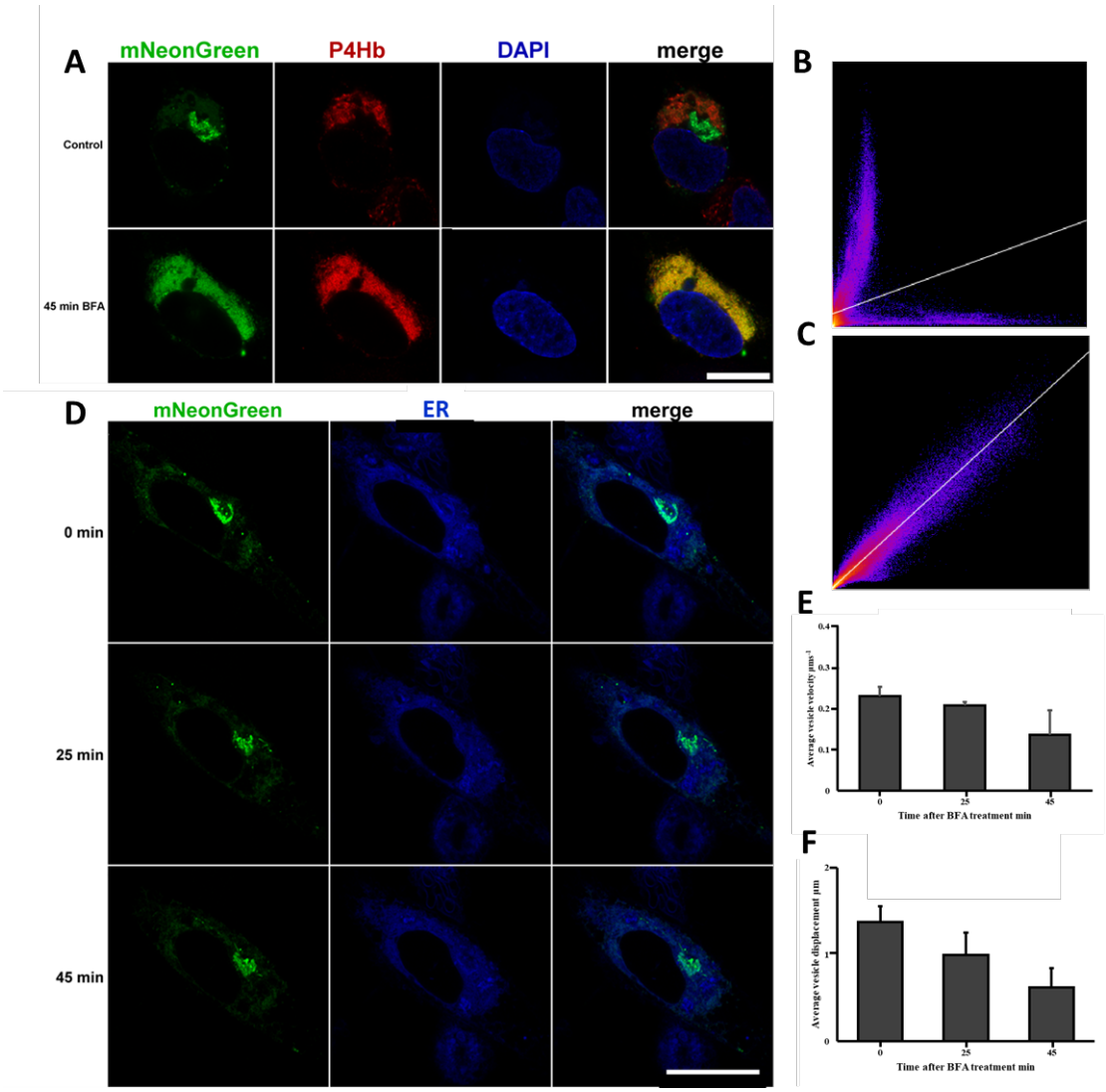

Figure 5.3 treatment with BFA results in collagen I retention in the ER. Panel (A) HT1080 expressing CMV promoter driven mNG-COL1α2 (green) were left untreated or treated with 100 ngmL^{-1} BFA for 45 min prior to fixation in 4% PFA. The ER resident protein PDI was stained by immunofluorescence (red) and the nucleus was stained with DAPI (blue). Scale bar = 20 µm. (B) 2D intensity histogram for control cell, showing green pixel saturation (x) against red pixel saturation (y) Pearson's R value = 0.27, Coste's P value = 1.00. (C) 2D intensity histogram for BFA treated cell, showing green pixel saturation (x) against red pixel saturation (y). Pearson's R value = 0.96. Coste's P value = 1.00. Panel (C) HT1080 cell expressing the CMV promoter driven mNG-COL1α2 construct (green) were stained with ER tracker blue-white to identify the ER (blue) frame 1 of 50 frame time lapse movies taken at 0, 30, and 60 min after addition of 100 ngmL^{-1} BFA. Scale bar 200 µm. Vesicle movement in the 50 frame movies for 0, 30, and 60 min was quantified using Fiji plugin TrackMate for 3 cells (E) average vesicle velocity over time, with standard error bars. (F) average vesicle displacement over time, with standard error bars.

5.5 Discussion

5.5.1 mNG is retained on Col1α2 expressed by transfected cells

Figure 5.1 shows that the mNG tag is retained on mNG-COL1α2 expressed by HT1080 and Saos-2 cells following transfection (figure 5.1 C-D). This provides confidence that mNG signal is representative of collagen1α2 in the cell, not mNG alone. It was consistently observed that BJ hTERT cells expressed mNG-

COL1α2 at a lower level than HT1080 cells or Saos-2. Resulting in a concentration of mNG-COL1α2 that was below the detection of the mNG antibody and Typhoon imager in these lysates (figure 5.1 A-D).

It was also observed that transfection of BJ hTERT cells with mNG-COL1α2 decreased endogenous collagen I expression compared to the UT control group (figure 5.1 A). The mechanism underlying the decreased expression of endogenous collagen following transfection with mNG-COL1α2 is not currently known. Further investigation is needed in order to fully investigate this phenomenon and the underlying mechanism controlling it, before the BJ hTERT cell line can be used to accurately model collagen trafficking within the skin.

5.5.2 mNG-COL1α2 is trafficked through ER and Golgi

In experiments in which HT1080 cells expressing CMV promoter driven mNG-COL1α2 were treated with CHX or BFA, vesicle number in the cell periphery decreased and those which remained were significantly less dynamic than those present prior to treatment (figure 5.3-5.4). As CHX blocks ribosome activity, or BFA blocks egress of mNG-COL1α2 from the ER, fast moving vesicles from the cell periphery will eventually be lost by exocytosis. With no newly synthesised mNG-COL1α2 able to exit the ER to replace it, vesicle number and average vesicle speed and displacement decline. These experiments together provide evidence consistent with the idea that mNG-COL1α2 is synthesised by ribosomes and passes through the ER and Golgi before being packaged into secretory vesicles which can be released from the cell by exocytosis. The timings of these experiments fit with those observed in figure 4.4, where all collagen is secreted from the cell within 3 hr of synthesis. Therefore, mNG-COL1α2 is likely trafficked through the standard cell secretory pathway in a similar fashion to collagen (section 1.2). Further investigation should be carried out to identify loss of collagen through degradation. Further proteomics based mass spectrometry studies should be carried out to determine if mNG- COL1α2 is able to form trimers with endogenous collagen1α1.

6 Studying post-Golgi trafficking of collagen using mNG-COL1α2

6.1 Rationale

The mechanism underlying transport of procollagen from the Golgi to the PM is currently poorly understood within the field of collagen biology (section 1.2.4). The large size and bulky mechanical properties of collagen I require transport in large, tubular post-Golgi carriers, which have been characterised by light and electron microscopy (Polishchuk et al., 2000). The high resolution, real time imaging of collagen achieved with the mNG-COL1α2 construct provides a novel method to observe post-Golgi collagen carriers. The use of airyscan for super-resolution confocal imaging and the mNG fluorophore for long term imaging allows the morphology and dynamics of post-Golgi collagen carriers to be observed in

better detail than has previously been achieved in other studies. In this section, the mNG-COL1α2 construct was used to characterise collagen carriers, and investigate their dependence upon the cell cytoskeleton and ATP, following current research that the transport of large pleomorphic carriers is dependent upon microtubule motors (Kalson et al., 2013; Kamata et al., 2017).

6.2 Characterisation of pleomorphic Golgi-to-PM carriers

To characterise the post-Golgi collagen I carriers, five HT1080 cells expressing CMV promoter driven mNG-COL1α2 were studied by laser scanning confocal microscopy 24 hr following transfection. It was often observed throughout the project that cells grown within the same dish had variable post-Golgi collagen I carrier morphology, size and dynamics. Five independent HT1080 cells expressing CMV promoter driven mNG-COL1α2 were imaged under the same conditions by time-lapse confocal microscopy. Selected regions of interest were enlarged to observe the post-Golgi carriers (figure 6.1 A). In all five cells, it was observed that the post-Golgi carriers were found in the cell periphery, and their bulk movement was toward distinct regions of the PM.

Ten post-Golgi carriers in each of the five cells displayed in figure 6.1 A were selected at random and measured. During measurement it was also recorded if the carrier was spherical or tubular in shape. The worm-like carriers accounted for 20-40% of all carriers observed (table 6.1). The diameter of the spherical carriers only varied slightly between cells, with a total range of vesicles found being 0.357 – 0.748 μm in diameter (table 6.1). This result rules out a clathrin-dependent system, in which spherical vesicles have diameters of 0.06 – 0.1 μm, and is more in line with observations of large carriers which can range in morphology and length from 0.3 – 1.7 μm and are often tubular rather than spherical (Kirchhausen et al., 2014; Polishchuk et al., 2000). The longest length of a tubular structure, measured in cell 4, had a major diameter of 2.507 μm, larger than any previous observations from the literature. In all five cells, the post-Golgi carriers were found in the cell periphery and had a bulk movement toward specific regions of the PM.

The tubular carriers were observed to move at a lower velocity and travel less distance than the spherical carriers, likely due to their smaller size and regular shape allowing a faster average velocity than the tubular structures. Cell 4 was chosen to further investigate the dynamics of spherical versus tubular carriers, due to the large average vesicle size and grouping of post-Golgi carriers in the cell periphery making it easier to manually count spherical and pleomorphic carriers. A region of interest at the cell periphery rich in both tubular and spherical post-Golgi carriers was chosen to more closely observe post-Golgi dynamics (figure 6.1 B). The number of spherical and the number of tubular vesicles was counted every 5 frames in the region of interest. The total number of spherical collagen carriers fluctuated throughout the time lapse, while the number of tubular collagen carriers remained reasonably stable (figure 6.1 C).

The number, size and morphology of post-Golgi collagen carriers was highly variable. The morphology and dynamic movements of the observed carriers is consistent with the limited observations of collagen trafficking and large tubular carriers in the literature. The mNG-COL1α2 construct will now be used to investigate the role of the cell cytoskeleton and intracellular production of ATP on the morphology and dynamics of post-Golgi collagen carriers.

Table 6.1 dimensions of post-Golgi carriers for five HT1080 cells (depicted in figure 6.1 A). Measurements are averages of 10 randomly selected vesicles throughout the peripheral cytosol measured in Fiji.

	Average area of post-Golgi carrier (μm^2)	**Average perimeter of post-Golgi carrier (µm)**	**Average diameter of spherical carriers (µm)**	**Tubular collagen carriers (% of total)**
Cell 1	0.267	1.914	0.513	20
Cell 2	0.371	2.623	0.491	40
Cell 3	0.291	2.230	0.472	30
Cell 4	0.435	2.678	0.648	30
Cell 5	0.169	1.578	0.426	20

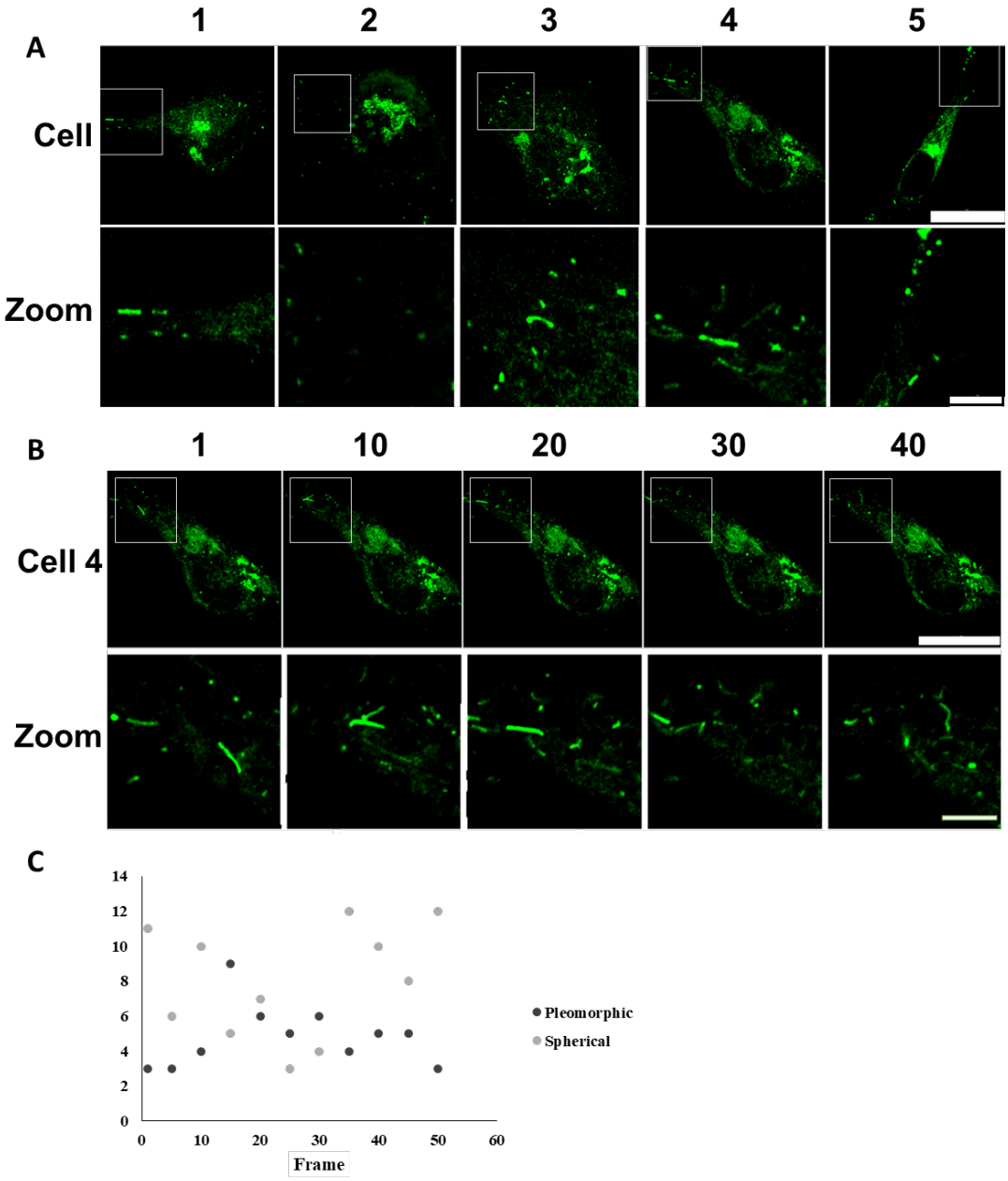

Figure 6.1 post-Golgi collagen I carriers. (A) a single frame of five HT1080 cells expressing CMV promoter driven mNG-COL1α2 (green) imaged as time-lapse movies. Scale bar = 100 µm. An area of interest in each cell is highlighted and displayed below the original image. Scale bar = 5 µm. (B) Frame 1, 10, 20, 30 and 40 of Cell 4 from (A). An area of interest is highlighted in grey and displayed below the original image. (C) counts of the number of pleomorphic and spherical vesicles from the zoom panel in (B) against frame number.

6.3 The microtubule dependence of Golgi-to-PM carriers

Large pleomorphic post-Golgi carriers have been closely associated with the microtubule cytoskeleton with a body of evidence suggesting that their movement is microtubule dependent (Toomre et al., 1999). To determine the dependence of post-Golgi traffic on the microtubule cytoskeleton, HT1080 cells expressing

the CMV promoter driven mNG-COL1α2 construct were treated with drugs to interrupt the microtubule cytoskeleton. The transfected cells were treated with 5 μM taxol for 15 min, a drug which blocks de-polymerisation of the microtubule cytoskeleton (Liebmann et al., 1993; L. M. Luo et al., 2013). Alternatively 5 μM colchicine was administered for 2 hr, a drug which completely de-polymerises the microtubule cytoskeleton (Ameri et al., 2018; Atkinson et al., 2010). Following treatment, the taxol or colchicine treated cells were fixed in 4 % PFA alongside a group of untreated control cells. Tubulin was stained by immunofluorescence and DNA stained by the addition of DAPI. Three cells for each treatment type were then imaged as z stacks by laser scanning confocal microscopy.

In the control cells, collagen filled carriers were found in abundance throughout the cell periphery with particular accumulation in cell projections, as previously observed (figure 6.1; figure 6.2 A). The majority of collagen carriers were closely associated with the microtubule cytoskeleton, and in many, but not all cases, appear to be tracking along the tubulin (figure 6.2 B). Following treatment with colchicine the tubulin was dispersed throughout the cytosol, indicating that depolymerisation occurred (figure 6.2 C). Following treatment with taxol, the tubulin was found exclusively in tubules which were brighter than the control, indicating that cytoskeletal stabilisation has occurred (figure 6.2 D).

Treatment with taxol or colchicine appeared to reduce the total number of vesicles found in the cell periphery (figure 6.2 C-D). To investigate this further, Z projections were made for three cells of each treatment type to observe the total vesicles throughout the cell (figure 6.2 E). The total number of vesicles found in three Z projections were counted, the control cells generally had the most vesicles, taxol cells generally had fewer, but the numbers were still comparable. However, the colchicine treated cells had a greatly decreased number of vesicles in the cell periphery (figure 6.2 F). The average vesicle area, as determined by measuring 10 randomly selected vesicles in each cell, also decreased following the disruption of the microtubule cytoskeleton, with colchicine treated cells having the lowest average vesicle area (figure 6.2 G).

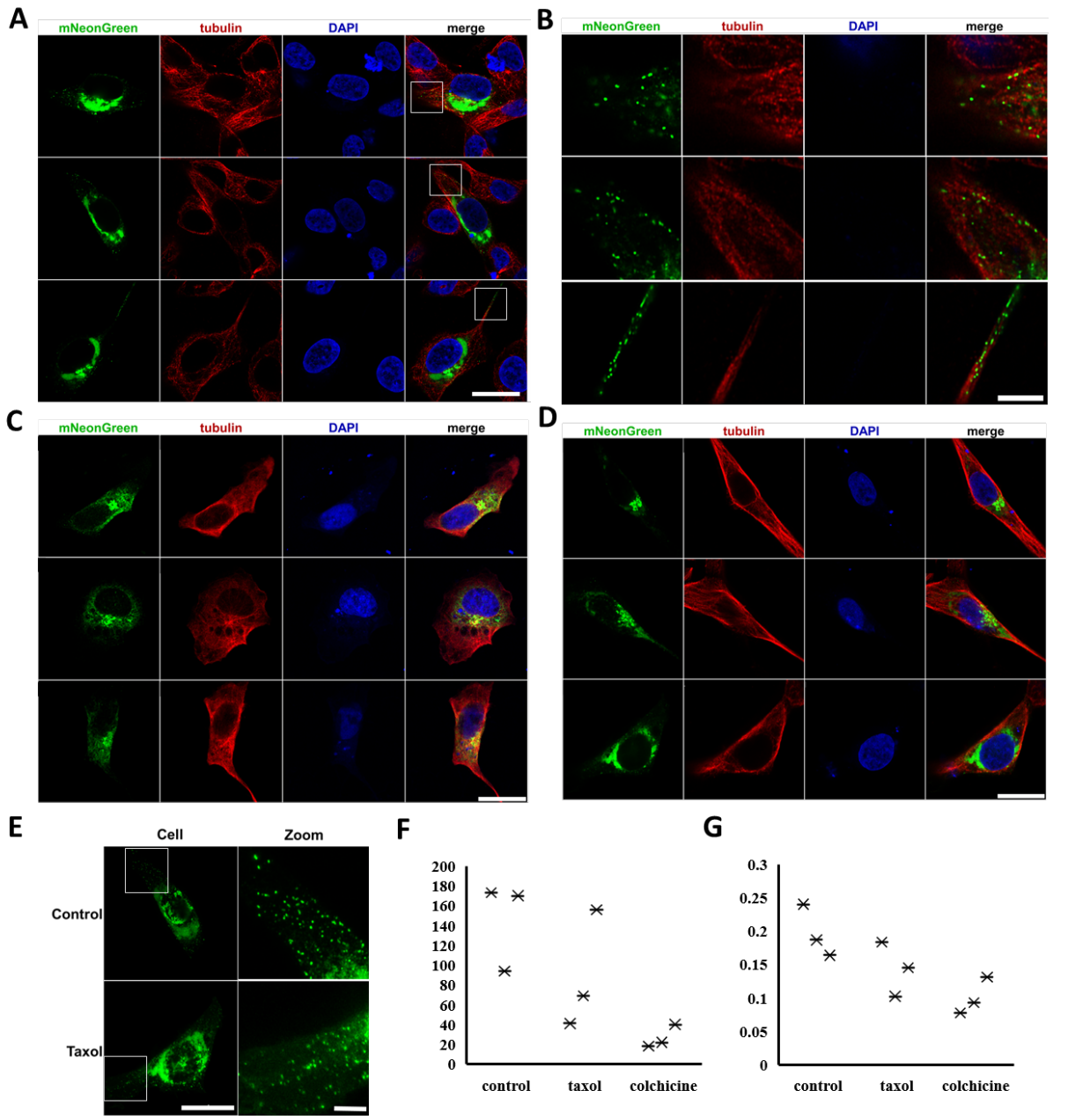

Figure 6.2 microtubule dependence of post-Golgi collagen carriers. HT1080 cells expressing CMV promoter driven mNG-COL1α2 (green) were fixed and probed for tubulin by IF (red) and DNA with DAPI (blue). Panel (A) three untreated cells were imaged by laser scanning confocal microscopy, a slice through the centre of the cell is shown with highlighted regions of interest. Scale bar 20 µm. Panel (B) regions of interest from (A). Scale bar 5 µm. Panel (C) three HT1080 cells treated with 5 µM colchicine for 2 hr immediately prior to fixation were imaged by laser scanning confocal microscopy, a slice through the centre of the cell is shown. Scale bar 20 µm. Panel (D) three HT1080 cells treated with 5 µM taxol for 15 min immediately prior to fixation were imaged by laser scanning confocal microscopy, a slice through the centre of the cell is shown Scale bar 20 µm. Panel (E) Z projections of one control cell and one taxol treated cell with regions of interest highlighted and displayed on the right of the panel. Scale bar 20 µm (cell) and 5 µm (zoom). (F) Total number of periphery vesicles counted in Z projections of three independent cells for control, colchicine and taxol treated cells. (G) Average vesicle area in Z projections of three independent cells for control, colchicine and taxol treated cells.

Given the reliance on the microtubule cytoskeleton established in figure 6.2, live HT1080 cells expressing CMV promoter driven mNG-COL1α2 were treated with taxol and colchicine, to determine if changes to collagen trafficking and distribution could be observed during the treatments timecourse. Three single cells were imaged prior to and continuously for 30 min after the addition of 5 μM taxol, or prior to and every 10 min for 2 hr after the addition of 5 μM colchicine. As the microtubule cytoskeleton is de-polymerised in the presence of colchicine, the cell became more rounded (figure 6.3 A). Of particular note, cell projections where collagen is trafficked to were lost, implicating a role of the cytoskeleton in directed trafficking, and confirming the idea that collagen is trafficked to particular regions of the cell (figure 6.3 A (arrows), B). Some morphological changes were also seen during taxol treatment, although overall directed trafficking is maintained in these cells (figure 6.3 C (arrows)).

To quantify the vesicle movement, the Fiji plugin TrackMate was used, which allowed an average collagen carrier velocity and displacement to be obtained during the time course of drug treatment for each cell. For the colchicine treatment, two cells underwent a significantly decreased average vesicle velocity and displacement following 120 min colchicine treatment. Whereas all three taxol treated cells saw a significant decrease in average vesicle velocity and displacement following 30 min treatment with taxol (figure 6.3 D-G; table S1-4).

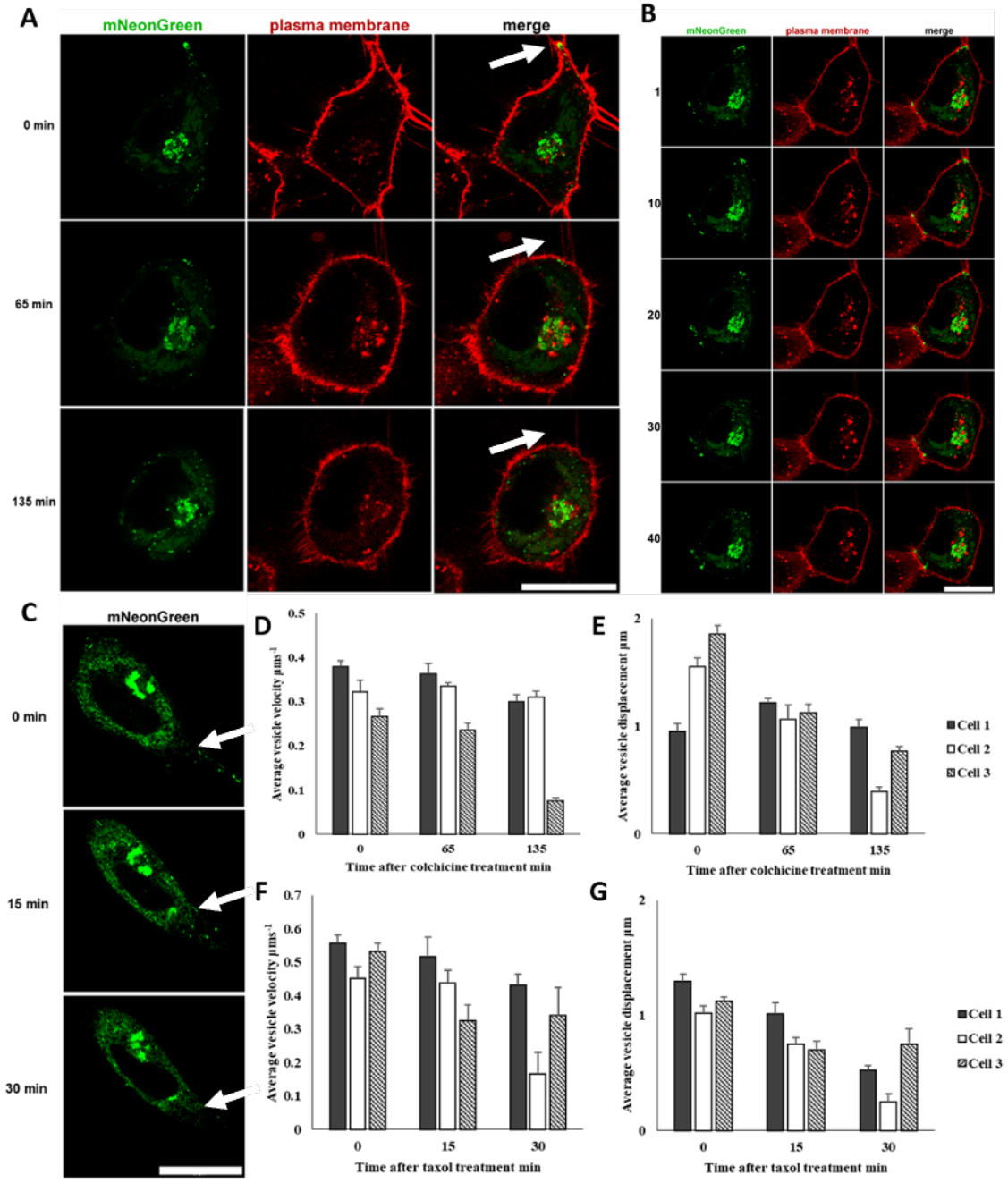

Figure 6.3 the effects of colchicine and taxol on live cells. (A) An HT1080 cell expressing mNG-COL1α2 (green) were stained with cell mask to identify the PM (red) and treated with 5 µM colchicine. The first frame of each 50 frame time-lapse taken every 10 min after the addition of colchicine is shown. Arrows show vesicle trafficking points. Scale bar 50 µm. (B) Time lapse of the cell from (A) 55 min after the addition of colchicine. Frames 1, 10, 20, 30 and 40 from the 50 frame time lapse are shown. Scale bar 50 µm. (C) An HT1080 cell expressing mNG-COL1α2 (green) imaged at 0, 15 and 30 min after the addition of 5 µM taxol. Arrows show vesicle trafficking points. Scale bar 20 µm. (D) bar graph to show the average vesicle velocity in 3 cells after the addition of colchicine. (E) bar graph to show the average vesicle velocity in 3 cells after the addition of taxol bar graph to show the average vesicle displacement in 3 cells after the addition of colchicine. (G) bar graph to show the average vesicle displacement in 3 cells after the addition of taxol.

6.4 The actin dependence of Golgi-to-PM carriers

The actin cytoskeleton is also implicated in the movement of post-Golgi carriers. To investigate the extent to which the actin cytoskeleton is involved in the movement of post-Golgi collagen carriers, HT1080 cells expressing CMV promoter driven mNG-COL1α2 were treated with lat B (Kazami et al., 2011; Nishimura et al., 2011; Soltaninassab et al., 2008). Lat B is a G-actin binding toxin, the presence of which prevents the polymerisation of G-actin monomers into F-actin fibrils within the cell (Wakatsuki et al., 2001). To observe collagen distribution in the presence of a de-polymerised actin cytoskeleton, HT1080 cells were left untreated to act as a control, or treated with 5 μM lat B for 2 hr prior to fixation in 4% PFA. The fixed cells were stained with the actin binding protein phalloidin conjugated to a 568 nm fluorophore, and the nuclear stain DAPI (Chazotte, 2010). Z stacks of three cells and three lat B treated cells were then obtained by laser scanning confocal microscopy.

A 2 hr treatment with 5 μM lat B resulted in a redistribution of the actin cytoskeleton. In the control cell, actin was found predominantly at the cell periphery, with a few clusters throughout the cytosol. In the lat B treated cells, actin was dispersed throughout the cytosol and formed large aggregates at the cell periphery (figure 6.4 A). Z stacks of three control, and three lat B treated cells were processed to obtain a Z projections. Ten vesicles from the Z projections for the lat B and control cells were chosen at random and measured. This showed that the average vesicle area was typically larger in the Lat B treated cells, compared to the control cells (figure 6.4 B). Although total vesicle counts from Z projections showed that the control cells had a greater number of collagen vesicles (figure 6.4 C).

The effect of lat B treatment was also observed in live HT1080 cells. Three HT1080 cells expressing CMV promoter driven mNG-COL1α2 were imaged at 0, 30, 60, and 90 min following treatment with 5 μM lat B. As expected the gross morphology of all three cells changed during lat B treatment as peripheral actin filaments were de-polymerised, this also resulted in some loss of cell size. In cell 2 and cell 3, a change to the shape of the Golgi was observed after 30 min of lat B treatment, with the Golgi cisternae appearing to become more dispersed and ribbon-like (figure 6.4 D). Quantification of average vesicle velocity and displacement using TrackMate showed that only one cell saw a significant decrease in average vesicle velocity following 90 min lat B treatment, and no cells saw a significant decrease in vesicle displacement (figure 6.4 E-F; table S5-6). Although it should be noted that the number of vesicles detected in all three cells decreased over time.

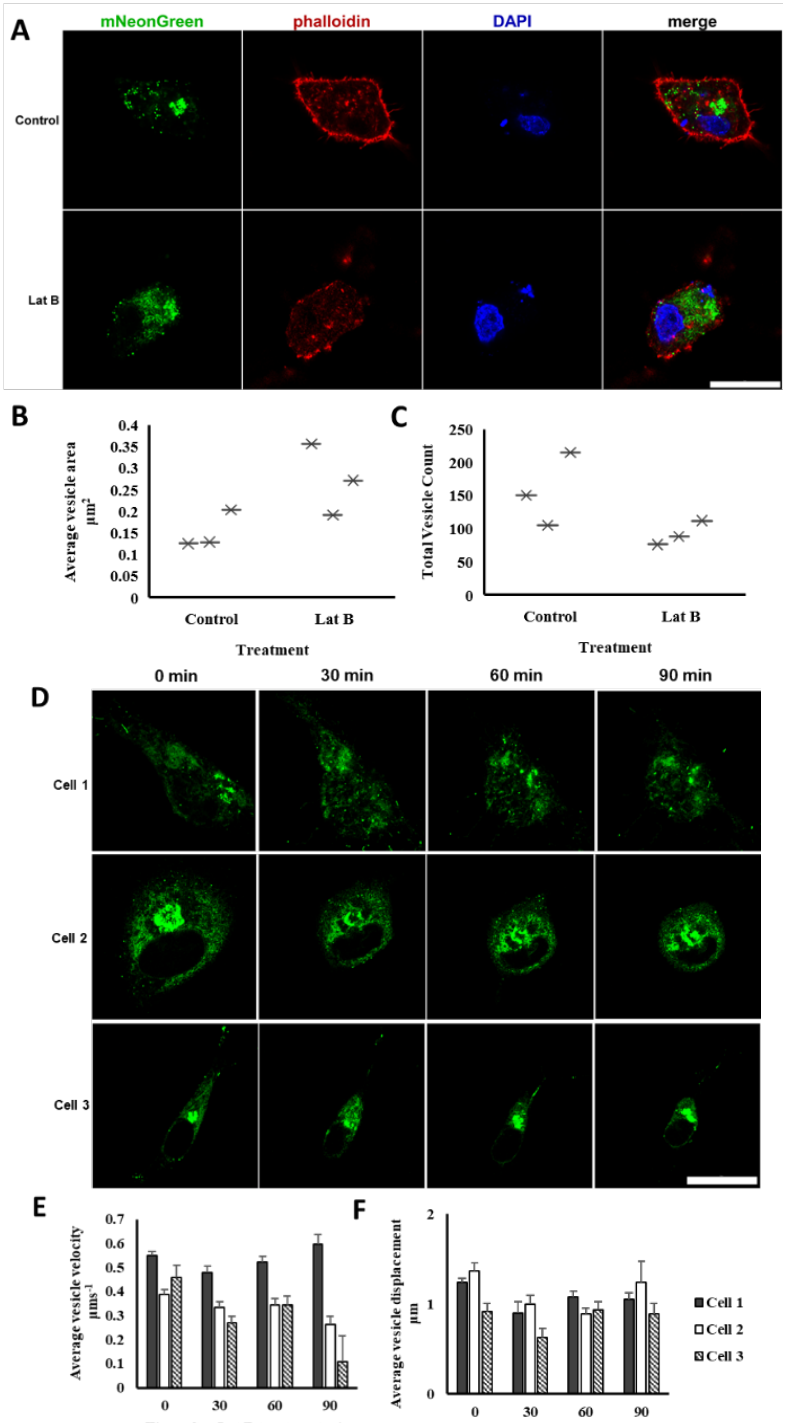

Figure 6.4 the actin dependence of collagen trafficking. Panel (A) HT1080 cells expressing CMV promoter driven mNG-COL1α2 (green) were left untreated as a control, or treated with 5 µM lat B for 2 hr prior to fixation and staining with phalloidin (red) and DAPI (blue). Scale bar 20 µm. (B) The average area of 10 vesicles measured in three control and three lat B treated cells. (C) The total number of vesicles counted in the cell periphery of three control and three lat B treated cells. Panel (D) three HT1080 cells expressing CMV promoter driven mNG-COL1α2 were treated with 5 µM lat B and 50 frame time lapses captured every 10 min after the addition of 5 µM lat B for 90 min. Scale bar 20 µm. (E) the average vesicle velocity in each cell at 0, 30, 60 and 90 min after addition of lat B with standard error bars. (F) the average vesicle displacement in each cell at 0, 30, 60 and 90 min after addition of lat B with standard error bars.

6.5 The energy dependence of Golgi-to-PM carriers

Cytoskeletal motor proteins, such as myosin on the actin cytoskeleton and kinesins on the microtubule cytoskeleton, are closely involved in the traffic of large post-Golgi carriers. Both myosins and kinesins are ATPases, with hydrolysis of ATP to ADP required to facilitate movement along the actin or microtubule cytoskeleton, respectively (Lee Sweeney & Holzbaur, 2018). By blocking the production of ATP within the cell, the role of cytoskeletal motor proteins on collagen trafficking could be investigated.

Three HT1080 cells expressing CMV promoter driven mNG-COL1α2 were treated with 0.05% sodium azide and 50 μM 2-deoxy-d-glucose to block all intracellular production of ATP (Zhang et al., 2014). Sodium azide inhibits cytochrome C in the mitochondria to prevent the aerobic production of ATP (Zuo et al., 2019). 2-deoxy-d-glucose is a d-glucose analogue preferentially hydrolysed by the cell in anaerobic respiration in a fashion which does not result in ATP production (Pajak et al., 2020). The three treated cells were then imaged every 10 min for 2 hr following the addition of ATP blocking drugs.

Sodium azide/2-deoxy-d-glucose treatment resulted in changes to gross cell morphology, with the cell become smaller and more rounded. This potentially was partly due to toxicity from the reduction of cellular ATP. Collagen within the Golgi is re-distributed during sodium azide treatment, forming ribbon-like structures within the perinuclear region 60 min after treatment (figure 6.4 D, 6.5 A). This was consistently observed in multiple cells imaged following 140 min treatment with sodium azide and 2-deoxy-d-glucose.

Unlike the taxol, colchicine or Lat B treated HT1080 cells, there was a significant decrease in the average collagen carrier velocity and displacement of in all three cells imaged between 0 and 120 min of treatment with sodium azide / 2-deoxy-d-glucose (figure 6.5 B-C; table S7-8). This was determined by TrackMate analysis of collagen carriers in the cell periphery over time, of each cell imaged.

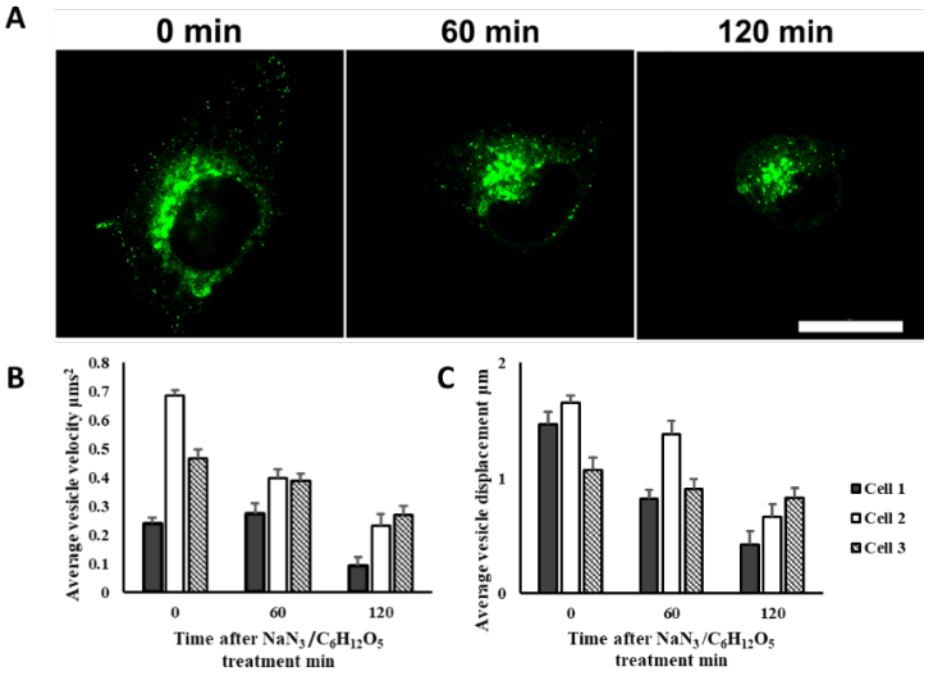

Figure 6.5 the energy dependence of post-Golgi collagen I carriers. (A) an HT1080 cell expressing mNG-COL1α2 under control of the CMV promoter (green) treated with 0.05% sodium azide and 50 µM 2-deoxy-d-glucose and imaged for 50 frames. The first frame of the resultant time lapse at 0, 60, and 120 min after treatment is shown. Scale bar 20 µm. (B) Vesicle movement was quantified across three repeats using TrackMate and average vesicle velocity against time (B) and average vesicle displacement against time (C).

To further investigate the energy dependence of vesicle trafficking, HT1080 cells expressing CMV promoter driven mNG-COL1α2 were treated with 2.5 ppm of the P&G bioactive ATPeptide for 24 hr, or left untreated to act as a control. ATPeptide acts to stabilise energy production within cells and is used by the skincare industry for its ability to 'revitalise aging skin' (Ashland Industries Ltd). To determine the effect of ATPeptide on the cells, fifteen ATPeptide treated cells and fifteen untreated cells: allowing for five biological repeats within three technical repeats, were imaged for 50 frames using time lapse laser scanning confocal microscopy. The same magnification and laser power were used to acquire all images. A large sample size was used to account for cell to cell variability as the ATPeptide required a long treatment time, so could not be imaged continuously throughout treatment.

Treatment with ATPeptide did not result in any obvious changes to cell morphology, or have significant visual effects on cell or vesicle size. Variation between cells occurred both within the ATPeptide and untreated cells, this was not deemed significant due to high variability between cells in the same culture observed throughout the project (figure 6.7 A). TrackMate was used to quantify the vesicle velocity, vesicle displacement, and vesicle number in each of the fifteen repeats for both treatments. This showed that treatment with ATPeptide did not result in a statistical difference to total vesicle number, vesicle velocity, or vesicle displacement (figure 6.7 B-D; table S9). The average fluorescence intensity of the total cell and

of ten vesicles per cell was also measured in Fiji. This showed that treatment with ATPeptide significantly increased the average fluorescence intensity of the whole cell and of the individual collagen vesicles when compared to the control (figure 6.7 E-F; table S9).

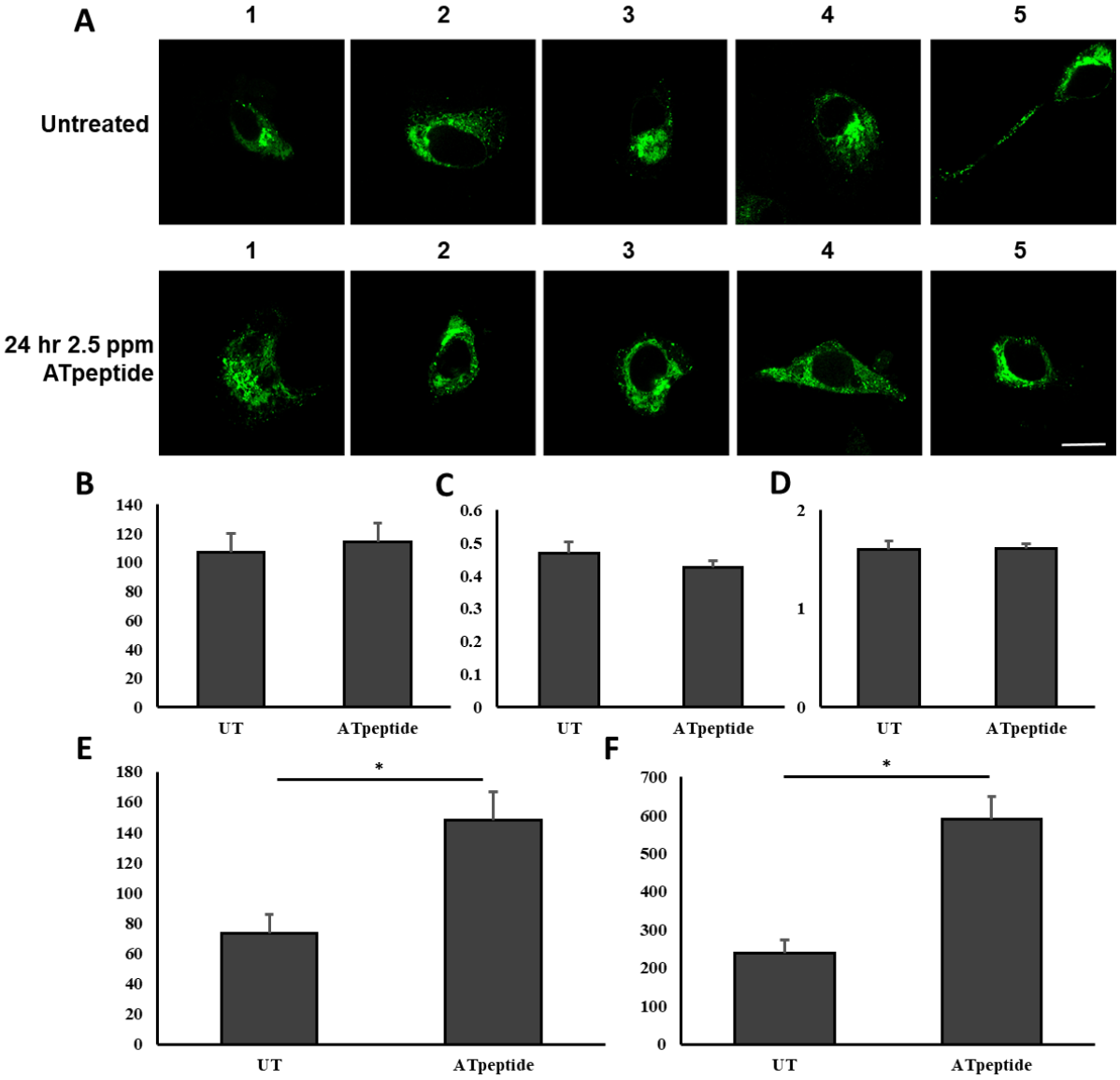

*Figure 6.6 the effect of ATPeptide on post-Golgi collagen I trafficking. (A) HT1080 cells expressing CMV promoter driven mNG-COL1α2 (green) were untreated (top) or treated for 24 hr with 2.5 ppm ATPeptide (bottom), then imaged for 50 frames by laser scanning confocal microscopy. The first frame of the resultant time lapses is shown for five cells for untreated and ATPeptide treated, and are labelled 1-5. Scale bar 20 µm. (B) bar graph to show the effect of ATPeptide on total vesicle number. (C) bar graph to show the effect of ATPeptide on average vesicle velocity in µm². (D) bar graph to show the effect of ATPeptide on average vesicle displacement in µm. (E) bar graph to show the effect of ATPeptide treatment on average cell fluorescent intensity in arbitrary units. (F) bar graph to show the effect of ATPeptide treatment on average vesicle fluorescence intensity in arbitrary units. * statistically significant as determined by student's T test.*

6.6 Discussion

6.6.1 Characterisation of post-Golgi collagen carriers

Post-Golgi collagen carriers were observed throughout the cell periphery. The carriers were typically spherical, with a range of diameters observed between 0.357 – 0.748 μm (figure 6.1 A). Some carriers had a tubular morphology, with the largest diameter measured being 2.507 μm. The size, number and morphology of post-Golgi collagen carriers varied greatly within single cells. The large vesicle size makes it unlikely that all collagen carriers are packaged in a clathrin dependent system, as clathrin vesicles have uniform morphology and diameters ranging between 0.06 - 0.1 μm (Kirchhausen et al., 2014). This is in keeping with similar observations within the literature of variable post-Golgi collagen carriers (section 6.2).

In future experiments, the movement of the carriers will need to be quantified to further investigate the relationship between carrier morphology and velocity/displacement. As well as confirming the observation that carriers have a bulk movement toward discrete regions of the PM. This could not be achieved using TrackMate in this research, as the tubular carriers were often identified as multiple vesicles moving together rather than a discrete single structure. Super resolution imaging would be helpful here to determine how many of the identified tubular structures are truely large vesicles and how many are strings of vesicles. Manual tracking was too prone to user bias to have been viable option to track the tubular structures. More sophisticated tracking technologies such as deep learning will need to be used in the future to fully quantify the movement of tubular collagen carriers. Staining with markers of endosomes, lysosomes, and the Golgi will also have to be carried out to confirm that all collagen carriers observed are Golgi derived.

6.6.2 The actin cytoskeleton and the Golgi

A change in collagen distribution was observed in the perinuclear region of the cell – likely within the ER or GOlig, although further staining experiments would be needed to confirm this (figure 6.4-6.5). The actin cytoskeleton and its motor protein non-muscle myosin II are closely implicated with the Golgi structure and function. When the actin cytoskeleton is disrupted by the addition of drugs such as cytochalasin D or lat B, the Golgi forms ribbon like structures which are re-organised to juxtapose the ER as part of a microtubule dependent process (Di Campli et al., 1999; Egea et al., 2013; Lázaro-Diéguez et al., 2006). This body of literature is consistent with the morphological changes to the Golgi observed in this research following lat B and sodium azide/2-deoxy-d-glucose treatment. Supporting that notion that the actin cytoskeleton and non-muscle myosin II are important in maintaining Golgi structure (figure 6.4, figure 6.5). To confirm that morphological changes to the Golgi were caused by disruption of the actin cytoskeleton and non-muscle myosin, Lat B treatment and sodium azide/2-deoxy-d-glucose treatments could be imaged live using an actin stain.

6.6.3 The role of the microtubule and actin cytoskeletons

Experiments using Lat B and colchicine to de-polymerise the actin and microtubule cytoskeletons, respectively, have shown that an intact actin and microtubule cytoskeleton are highly important to regulate collagen carrier formation at the TGN. Treatment with colchicine has resulted in a decrease in the number of collagen vesicles and their overall size (figure 6.2 F-G). Treatment with Lat B has resulted in a decrease in the total number of collagen carriers, but an overall increase in their average size (figure 6.4 B-C). Treatment of cells with taxol to stabilise the microtubule cytoskeleton did not result in a change to the size or number of vesicles released from the TGN.

The actin and microtubule cytoskeletons and their motor proteins are known to have a role in the fission of secretory bodies from the TGN, explaining why their disruption results in aberrant carrier sizes. Experiments involving the deletion or knock down of actin interacting proteins including myosin II and Rab 6 show that deleting these components results in an increased vesicle size from the TGN (Li et al., 2018; Miklavc & Frick, 2020; Stow et al., 1998; Valente et al., 2010). In particular the total deletion of non-muscle myosin II completely prevented fission of carriers from the TGN (Vicente-Manzanares et al., 2009). The microtubule motor protein KIF20A has also been shown to be important in the control of vesicle fission from the TGN, and helps to anchor newly budded Rab 6 positive vesicles to sites of microtubule nucleation (Miserey-Lenkei et al., 2017).

Experiments imaging live cells show that the microtubule cytoskeleton is more important in the Golgi-to-PM trafficking of collagen carriers than the actin cytoskeleton. Treatment with Lat B did not change the average velocity or displacement of the post-Golgi collagen carriers (figure 6.4 E-F). Both colchicine and taxol treatment resulted in a significant decrease in collagen carrier velocity and displacement in at least two cells (figure 6.3). This showed that the trafficking of collagen carriers through the cell periphery requires both an intact and dynamic cytoskeleton. There was a large variation observed in carrier dynamics for colchicine, taxol and Lat B treated cells, and more repeats are needed to establish a firm pattern.

6.6.4 The role of cytoskeletal motor proteins

Cytoskeletal motor proteins have been shown to be closely involved in the traffic of large post-Golgi carriers. Myosin II and the kinesin KIF20A have both been shown to be essential for the fission of large post-Golgi carriers at the TGN (Miserey-Lenkei et al., 2017; Vicente-Manzanares et al., 2009). The kinesin KIF5A has been shown to be involved in the trafficking of collagen carriers along the microtubule cytoskeleton to the cell membrane (Kamata et al., 2017). Live HT1080 cells were treated with sodium azide and 2-deoxy-d-glucose in order to prevent the production of ATP both by aerobic or anaerobic respiration (Pajak et al., 2020; Zhang et al., 2014; Zuo et al., 2019). This resulted in a significant decrease in the average

vesicle velocity and displacement of all three cells imaged after 120 min, consistent with the notion that microtubule and actin motor proteins are essential in collagen trafficking (figure 6.5).

Depletion of intracellular ATP might have resulted in decreased collagen carrier dynamics by preventing the ATPase activity of cytoskeletal motor proteins involved in the trafficking of collagen carriers (Tafoya & Bustamante, 2018; Takaki et al., 2019). Depletion of cellular ATP likely affected the activity of a range of proteins. A further experiment which inhibits only the activity of the cytoskeletal motor proteins should be carried out to determine the extent to which the observed morphology is due to altered cytoskeletal trafficking. An orangu assay should also be carried out to determine the extent of sodium azide/2-deoxy-d-glucose toxicity on cell viability. The sodium azide/2-deoxy-d-glucose treated cells should also be fixed to determine whether any changes to the size and number of collagen carriers occurred following treatment. This would also control for any potential toxicity from prolonged live imaging. Once these controls have been carried out, lat B and colchicine should be added together to HT1080 cells expressing CMV promoter driven mNG-COL1α2. A combined treatment to depolymerise both microtubule and actin cytoskeletons should result in the same morphology and dynamics blocking ATP production.

6.6.5 Directed trafficking of collagen carriers

Throughout section 6, it was consistently observed that collagen carriers were trafficked to distinct points at the cell periphery (figure 6.1-6.5). Throughout the literature, regions of bulk exocytosis which post-Golgi carriers are trafficked to, particularly of fibrillar ECM proteins, have been termed fibripositors. This phenomenon was first observed in the transport of fibronectin (Heggeness et al., 1978; Louvard, 1980). The directed transport was later proposed to be a result of trafficking of carriers along microtubules to focal adhesions for mass exocytosis, a process coordinated by the actin cytoskeleton (Hirschberg et al., 1998; Kalson et al., 2013). These studies are consistent with findings in this thesis that trafficking of collagen carriers through the cytosol is highly dependent upon the microtubule cytoskeleton. Further experiments imaging live cells with a tubulin tracker would provide confirmation that vesicles are trafficked along the microtubule cytoskeleton. An actin tracker could be used to confirm the role of actin at the PM.

6.6.6 ATPeptide

When cells were treated with the ATPeptide, a compound which stabilises the energy production of a cell, there was no significant change to the average displacement or velocity of collagen carriers. This showed that ATPeptide did not have a significant effect on the underlying biological processes occurring in the cell. Following ATPeptide treatment the fluorescence intensity of the whole cell and individual vesicles was significantly increased compared to the control cells. Implying a role of ATPeptide in increasing collagen production and increasing the rate of packing into secretory vesicles through the role of cytoskeletal motor proteins.

Overall, experiments with ATPeptide provide good confidence that its use increases collagen production in the cell. Nevertheless, further experiments need to be done. ATPeptide washout experiments would determine if the effect can be reversed once the bioactive is no longer present in the system. An experiment with hydrogen peroxide would show whether damage by reactive oxygen species can reverse the effect of the ATPeptide. The mechanism of ATPeptide action also needs to be further investigated to provide functional insight.

7 Collagen deposition

7.1 Rationale

Collagen proteins are the most abundant ECM component of connective tissues (McKee et al., 2019). Collagen fibrils self-assemble from procollagen peptides in the ECM, forming a mesh to provide support and structure to cells, as well as mediating cell adhesion, migration, signalling and development (Gelse et al., 2003; Goldberga et al., 2018; Gordon & Hahn, 2010). Collagen fibril self-assembly into mature ECM fibrils is dependent upon the cleavage of N and C propeptides from the procollagen peptide, in a process mediated by ADAM proteases (Le Goff et al., 2006). The mNG-COL1α2 peptide has been designed so that the mNG fluorophore occludes the native N terminal cleavage site, allowing mNG to be retained on secreted collagen1α2 (section 1.4; section 3.1.2). Visualisation of extracellular collagen in the ECM is essential for the use of the mNG-COL1α2 construct as a tool for both industrial and academic applications. This section provides evidence that the mNG-COL1α2 construct can be used to successfully visualise collagen deposited from cells in a 2D culture.

7.2 Optimising AA treatment

It is widely accepted that synthesis of mature collagen fibrils requires AA (Clark et al., 2002; Murad et al., 1981; Pinnell, 1985). AA is derived from vitamin C and acts as an essential cofactor for P4HB, the ER resident complex responsible for hydroxylation of proline residues on procollagen (Timmins et al., 2017; Vasta & Raines, 2016). In order to visualise deposition of mNG-COL1α2 around cells a concentration of 200 μM AA in growth media was determined to be optimal for collagen deposition (Diomede et al., 2019; Qiao et al., 2008). The length of treatment then had to be optimised in the professional collagen secreting cell line BJ hTERT, and HT1080 which do not secrete collagen I, to maximise collagen deposition from both cell types.

To optimise AA treatment, six dishes of BJ hTERT cells were plated at the same time and confluency and left untransfected to observe changes in endogenous collagen production. The cells were left to grow for 2 days and then the media was changed to remove any collagen secreted during the growth period. It was theorised that collagen would be soluble in this media rather than being deposited into an insoluble matrix

because the other components of the ECM were not present for collagen to be incorporated into. The cells were treated with AA for 5, 4, 3, 2, 1, or 0 days. HT1080 cells were transfected with CMV promoter driven mNG-COL1α2 or untransfected and then treated with AA for 1 or 0 days. Following the treatments, the growth medium the cells had been in for 5 days (BJ hTERT) or 1 day (HT1080) was removed and the proteins concentrated 20x by acetone precipitation. Ten microliters of the media prior to and following concentration for each group of cells were run on an 8% SDS PAGE gel, which was subsequently stained with Coomassie blue as a control to show that the concentration was successful. The bands were much darker and more intense in the acetone precipitated samples, showing that that more protein is present (figure 7.1 A). The cells were subsequently lysed in 1x RIPA buffer for intracellular protein analysis.

Ten micrograms of protein from the cell lysates and the concentrated media from both the HT1080 cells and the BJ hTERT cells were separated by electrophoresis on 8% SDS PAGE gels. The gels were transferred to PVDF membranes which were probed for collagen I and β actin by western blotting. The presence of collagen I in all lysates showed that treatment with AA did not increase collagen production within the cell in either the transfected HT1080 cells or the BJ hTERT cells. The longer the BJ hTERTs were treated with AA for, the fewer low molecular weight bands were present. The β actin loading control shows that less protein from the 0 day AA treated cells was loaded on the gel, which might be affecting this outcome (figure 7.1 B).

The presence of AA has a big impact on the secretion of collagen from the HT1080 cells transfected with CMV promoter driven mNG-COL1α2. In the BJ hTERTs the intensity of the collagen1α1 and collagen1α2 bands remained the same, independent of the time of AA treatment. In the presence of AA, there was an increase in higher molecular weight structures and a decrease in low molecular weight structures below the collagen1α2 isoform (figure 7.1 C).

From these results, a 1-day treatment with AA was determined to be optimal to visualise mNG-COL1α2 deposition. By treating cells with AA for 24 hr prior to imaging, the maximum amount of deposited collagen could be observed while preventing cell death and ensuring that mNG-COL1α2 expression was at its peak.

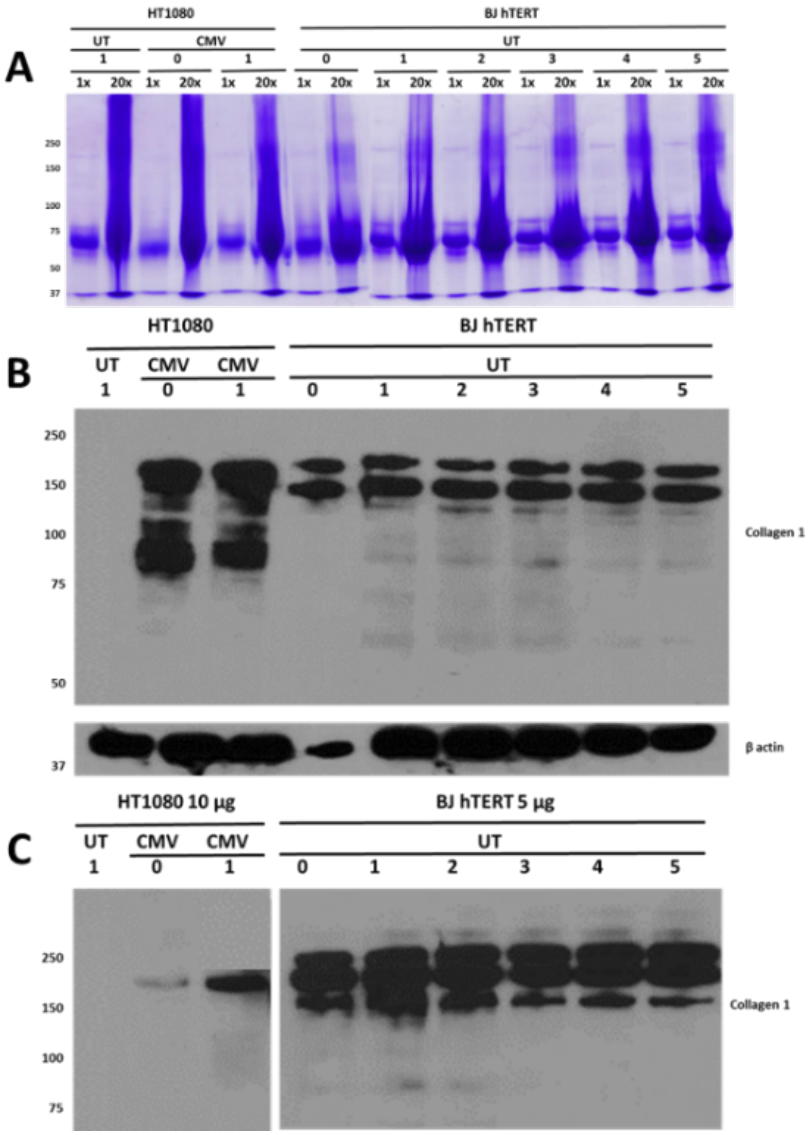

Figure 7.1 optimising AA treatment to observe collagen I deposition. Untransfected (UT) BJ hTERT cells and HT1080 cells UT or expressing CMV promoter driven mNG-COL1α2 (CMV) were treated with AA for 5, 4, 3, 2, 1, or 0 days. Following treatment, the growth media was harvested and concentrated 20x and the cells were lysed in RIPA buffer. (A) 10 µL of primary and concentrated media were separated by electrophoresis on an 8% SDS PAGE gel which was stained with coomassie to identify protein bands. Ten micrograms of cell lysates (B) or ten micrograms of concentrated media (C) separated by electrophoresis on an 8% SDS PAGE, transferred to a PVDF membrane then probed for collagen 1 by western blotting.

7.3 Collagen bursts

TIRF microscopy is a type of fluorescence microscopy which provides the best resolution on the Z axis. For TIRF imaging, a laser is directed at the specimen at such an angle that a very thin slice through the cell of approx. 100 nm in depth can be observed (Guo et al., 2018; Mattheyses et al., 2010). This allows real time visualisation of objects at the PM. TIRF has been used to provide insights into the movement of organelles and single molecules at the PM (Kudalkar et al., 2016). Recently, TIRF has been used

successfully to observe the moment of exocytosis of synaptic vesicles containing neurotransmitter into the synaptic cleft (Midorikawa, 2018). In this section, TIRF microscopy is used to visualise exocytosis of collagen into the ECM, something which has not been achieved in the field.

To observe exocytosis of collagen from post-Golgi collagen carriers, HT1080 cells expressing CMV promoter driven mNG-COL1α2 were imaged by TIRF microscopy, at a rate of 5 frames^{-1}. The PMs of three cells were captured in this way to obtain 601 frame time lapse movies which were then analysed to observe collagen exocytosis.

Collagen exocytosis was observed as a small flash of light immediately followed by the disappearance of the collagen carrier from the PM. Exocytosis events are distinct from events where a collagen carrier moves to the PM and then back into the cell based on a number of criteria, discussed later in this section. The location of all burst events which occurred in the time lapse were marked onto the first frame of the obtained time lapse for each cell in red. Although collagen filled carriers are found throughout the cell body, collagen exocytosis predominantly occurs in distinct locations at the cell periphery (figure 7.2 A).

The total number of burst events varied between the cells, with cell 1 having a total of 41 bursts, compared to 12 and 9 bursts in cell 2 and 3, respectively (figure 7.2 B). When considered with the total number of post-Golgi carriers counted for each cell: cell 1 = 1655, cell 2 = 626, cell 3 = 1299. The percentage of mNG post-Golgi carriers observed was also variable between the three cells: with 2.5% of observed carriers undergoing a burst in cell 1, compared to 1.9% and 0.69% in cell 2 and 3, respectively. The range likely reflects normal biological variability under the culture conditions.

Five burst events were chosen at random in each cell. A distinctive change in fluorescence intensity was observed for all 15 burst events in each cell. Measuring the fluorescence intensity of the burst 4 frames prior to (frame 1-4), during the burst (frame 5), and immediately post bust (frames 6-9) shows that fluorescence remains constant prior to burst, sharply decreases during burst and settles at a lower fluorescence post burst (figure 7.2 C-E). The changes in fluorescence correspond with the carrier remaining close to the PM immediately prior to the burst, the collagen being released into the ECM resulting in a sharp drop, and then collagen being absent from the area decreasing the overall fluorescence. The fluorescence intensity of the area once the burst has occurred does not return to zero following the burst, perhaps due to the presence of other carriers in the cell, but more likely due to the presence of collagen in the ECM.

The average carrier size and time spent stationary immediately prior to burst for the 15 chosen carriers in figure 7.2 C-E was also measured. The vesicle area prior to burst did not vary, found, on average, to be between 0.18 and 0.28 μm^2 (figure 7.2 F). Given the variability observed in the area of post-Golgi carriers within the cell periphery, it is interesting that the size of the carrier immediately prior to burst remains very

constant by comparison (section 6.2). It was also observed that vesicles were stationary for an average of 30 – 50 s prior to burst events in all 3 cells. Thirty to forty seconds is a long time for objects which have previously been observed to be highly dynamic in the cytoplasm. Although a range of 8.6 - 101.4 s stationary time was identified between the 15 bursts (figure 7.2 G). The long stationary time at the PM prior to burst was useful to distinguish bursting carriers from those which move to the PM and then return to the cell. Carriers which move up and down in Z and do not burst are far more motile in comparison and rarely persist at the PM for more than 1s before moving back into the cell.

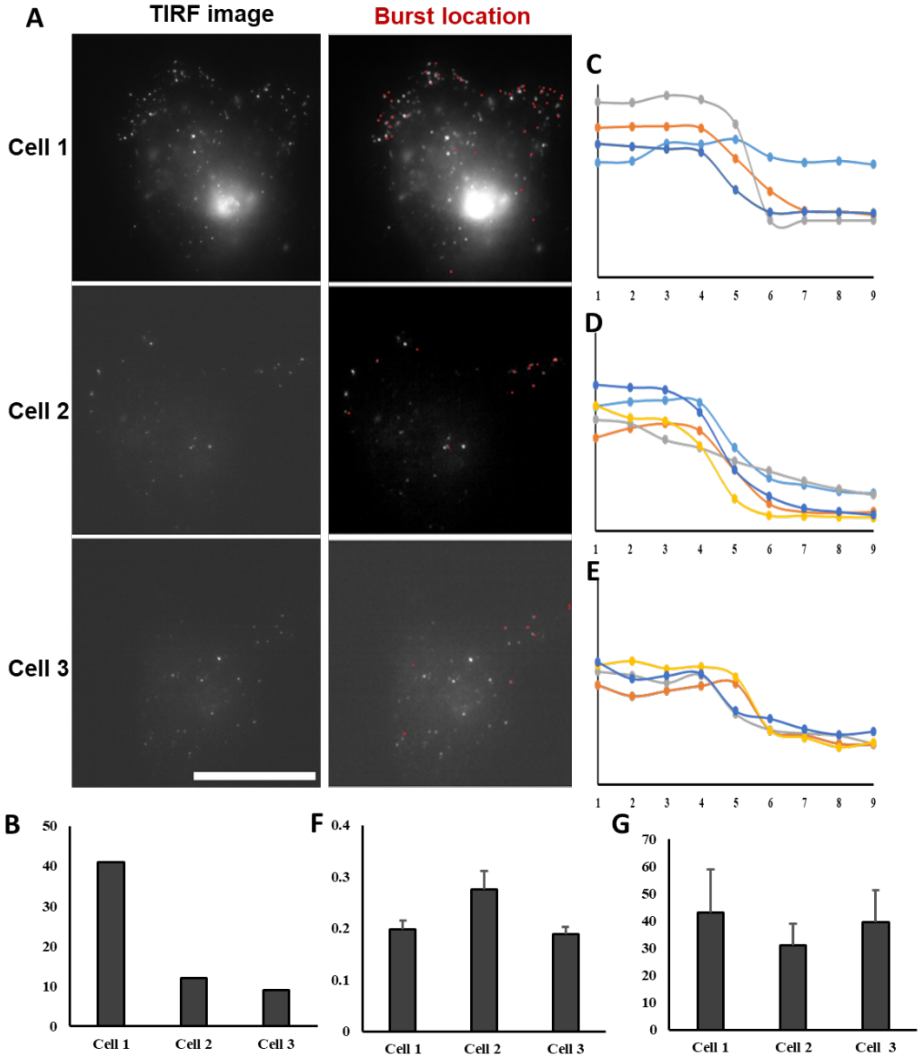

Figure 7.2 TIRF microscopy to visualise mNG-COL1α2 exocytosis. Three HT1080 cells expressing CMV promoter driven mNG-COL1α2 were imaged by TIRF microscopy for 601 frames at a rate of 0.2 s per frame. Panel (A) the first frame of the time lapse for each cell (left) with the location of all collagen bursts observed marked in red (right). Scale bar 20 µm. (B) the total number of bursts counted in each cell The fluorescence intensity of 5 vesicles from cell 1 (C) cell 2 (D) and cell 3 (E) was measured 4 frames prior to and 4 frames post burst. X axis represents frame number, y axis represents relative fluorescence intensity. The burst occurs in frame 5 on the graphs. (F) the average area of vesicles immediately prior to burst with standard error. (G) The average time in s for each cell vesicles remained stationary prior to burst with standard error. TIRF imaging performed by Dr Tim Hawkins.

To better observe the burst event, the time lapse movie for cell 3 was converted to a heat map, to show relative fluorescence intensity on a blue to red scale (figure 7.3 A). An area identified to have lots of burst events was identified from figure 7.2 A and magnified 4 times to observe the bursts in detail. In all burst events, a cloud of mNG fluorescence was seen outside of the cell, which persisted for varying lengths of time. Sometimes the burst was very short lived, lasting only 5 frames or 1 s in figure 7.3 B, or 8 frames/ 1.6 s in figure 7.3 C. Some bursts were longer lived, persisting for over 18 frames or 3.6 s in figure 7.3 D. The burst diameter was highly consistent, with the burst diameters measured from figure 7.3 being within 1 μm of each other: 7.3 B = 1.45, 7.3 C = 1.28 μm, 7.3 D = 1.96 μm.

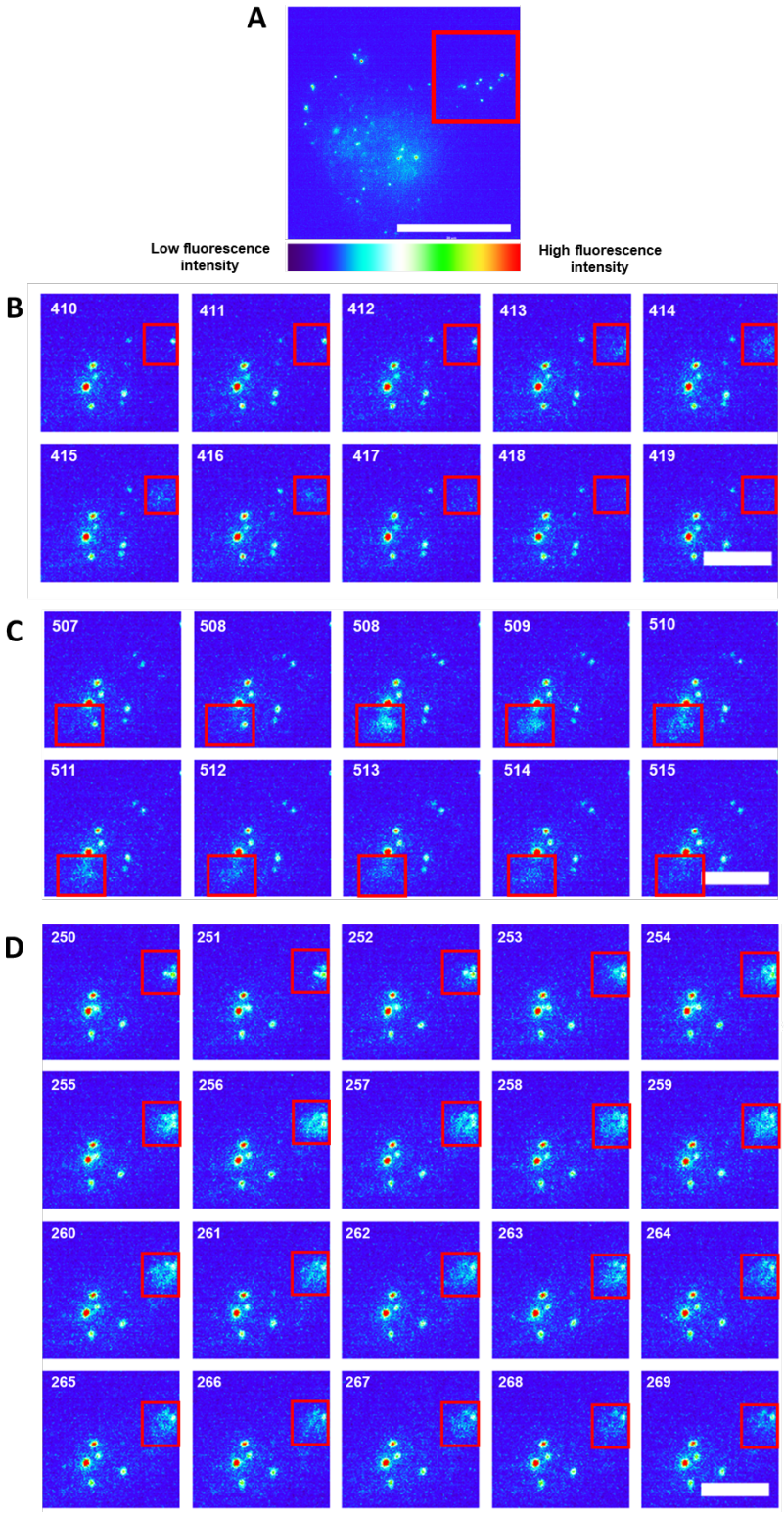

Figure 7.3 observing collagen burst morphology. (A) heat map generated from cell 3 from figure 7.2 with low fluorescence intensity in blue/purple and high intensity in red/yellow. Scale at bottom of figure. The top right portion indicated by a red box was zoomed in on. Scale bar 20 µm. Panel (B) frames 410 – 419 of heat map time lapse. Panel (C) frames 507 – 515 of time lapse. Panel (D) frames 250 – 269 of time lapse. Scale bars 5 µm. Bursts boxed in red.

7.4 Visualising collagen deposition

Fibroblasts are known to deposit collagen in 2D cultures. It is unlikely collagen deposited in 2D culture can form a fully functional ECM, due to lack of 3D environment, other ECM components such as fibronectin, and the absence of forces which would usually act upon collagen in a tissue (Good et al., 2019; Komatsu et al., 2018; Leung et al., 2015). A GFP-Col1α2 fusion protein has been shown to form mature collagen fibrils in the formation of scar tissue in the zebrafish model organism (Morris et al., 2018). In light of this, we aim to show that mNG-COL1α2 can be deposited by cells in a 2D culture as a proof of concept, and that collagen deposited has the correct characteristics to form mature fibrils.

The immortalised osteoblast cell line Saos-2 was used to visualise collagen deposition. The Saos-2 cells were transfected with the CMV promoter driven mNG-COL1α2 construct and treated with 200 µM AA 24 hr prior to imaging by laser scanning confocal microscopy. Optimisation of AA treatment time in this cell line could not be carried out due to time constraints. Instead, the AA treatment time frame identified as optimal for HT1080 collagen secretion was chosen (section 7.2). Immediately prior to imaging, the cells were either stained with cell mask deep red to identify the PM, or ER tracker blue-white to identify the ER.

The fibrillary mNG-COL1α2 was deposited and formed small fibrils immediately adjacent to the PM (figure 7.4 A-B). The average length of the collagen fibrils imaged in each cell were consistent: cell 1 = 13.75 µm, cell 2 = 9.63 µm, cell 3 = 10.97 µm. Most studies of collagen fibrils and their structure have taken place in tendons, because of the high typical and predictable structure of collagen (Hijazi et al., 2019). The physical properties of collagen in tendon is very different to those of collagen within the skin. This means that there is very little literature available on the length of collagen fibres in the skin, so it is unclear if this result is consistent with observations from other studeis. Encouragingly, the fibrils all have a uniform width, which is a typical characteristic of collagen fibrils (Raspanti et al., 2018).

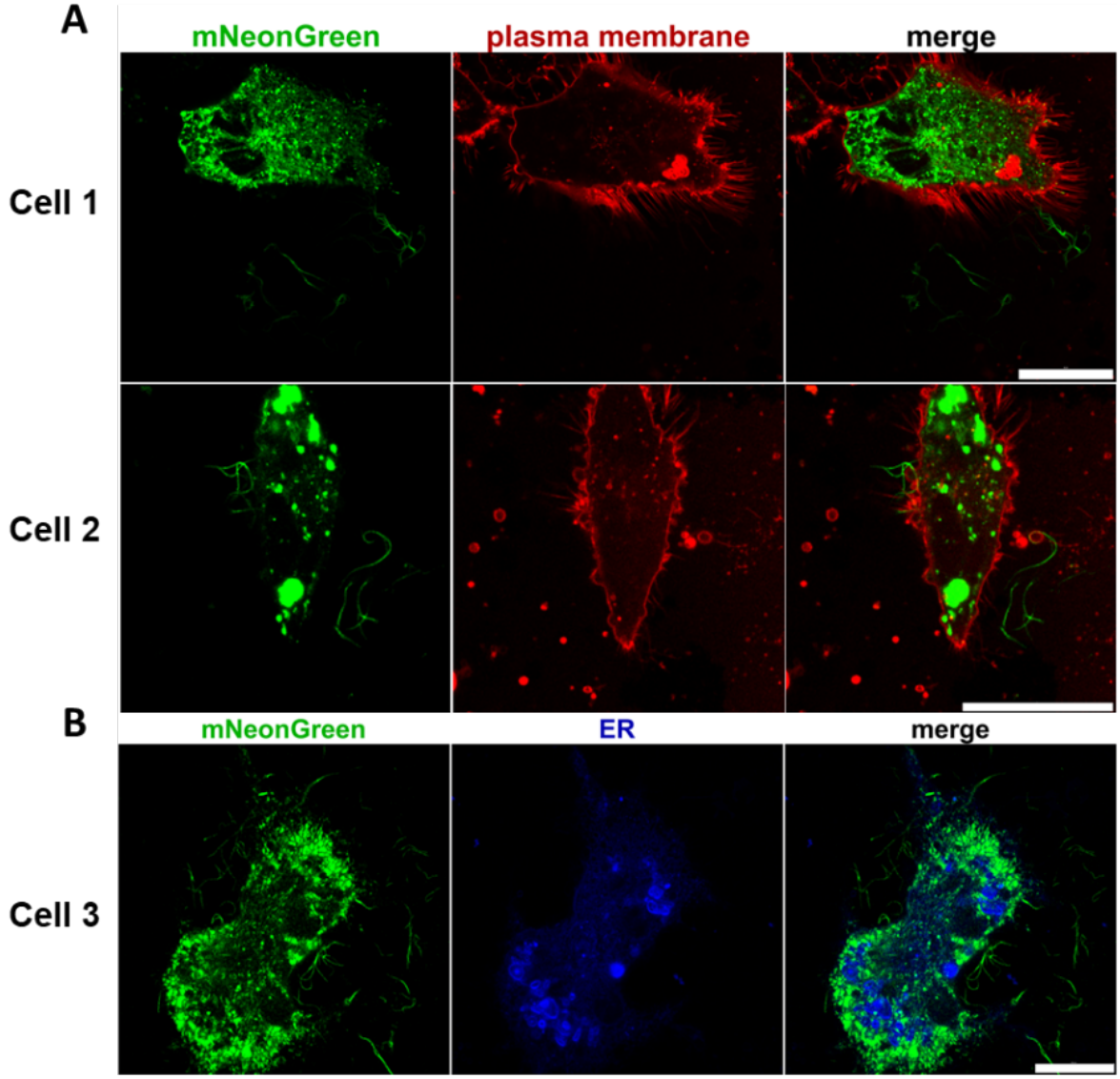

Figure 7.4 deposition of mNG-COL1α2 from Saos-2 cells. Saos2 cells expressing the CMV promoter driven mNG-COL1α2 construct (green) were stained with cell mask to identify the PM (red) or ER tracker to identify the ER (blue) and were imaged by laser scanning confocal microscopy. Panel (A) two cells stained with cell mask depositing collagen. Scale bars 20 µm. Panel (B) one cell stained with ER tracker depositing collagen. Scale bar 20 µm.

7.5 Quantifying collagen production and deposition

Ultimately, mNG-COL1α2 protein can be used to quantify the production of collagen both within the cell and deposited into the ECM, in the presence of different stimuli and bioactives. To achieve this, a novel high-throughput fluorescence assay was designed. In this novel assay, cell lysates and media could be placed in a 96-well plate and excited with 488 nm laser. The fluorescence emission could then be used to quantify the mNG-COL1α2 present (An, 2009).

A standard curve of mNG concentration against fluorescence intensity was first prepared. A lysate of pNCS transformed *E coli* was used as a source of mNG. His-tagged mNG was extracted from the lysate using a histidine purification column. Four elutants were obtained and separated by electrophoresis on a native Tris-Glycine gel. The gel was scanned with 488 nm laser light to identify the presence of mNG. A decreasing concentration of mNG was present in each elutant fraction (figure 7.5 A). The four elutants were combined and the mNG concentrated using a 3 kDa molecular weight cut off spin column. The concentration of the purified mNG was assessed by Bradford assay as 0.1 $mgmL^{-1}$.

A serial dilution of mNG was prepared and read for 512 nm emission following 488 nm excitation. A scatter plot of mNG concentration against fluorescence intensity gave a significant R value of 0.9938 (figure 7.5 B). To provide proof of concept that the assay could be used to quantify mNG concentration in cell lysates, HT1080 cells, either untransfected (UT) or transfected with the CMV promoter driven mNG-COL1α2 construct (CMV), were lysed in 1x MNT buffer. The total protein concentration of the lysates was determined by BCA assay. The lysates were read for 488 nm fluorescence alongside an mNG standard curve. This showed that fluorescence increased in the CMV HT1080 lysates compared to the UT and that the resultant 512 nm emission values could be used to calculate the concentration of mNG, and by extension the proportion of mNG-COL1α2 present in the total protein content (Table 7.1).

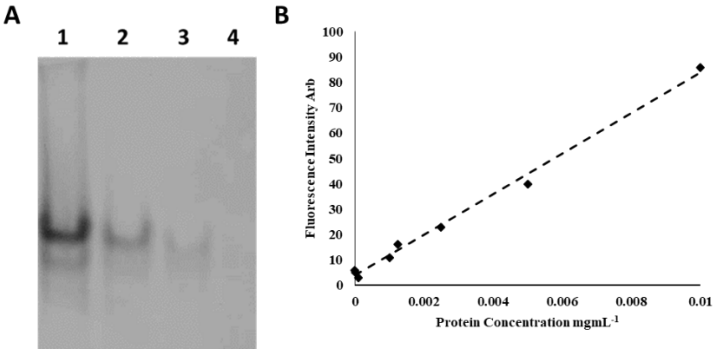

Figure 7.5 mNG standard curve. (A) four elutant fractions from a His-purification of pNCS transformed E coli lysate run on a native tris-glycine gel, which was scanned with 488 nm laser to detect the presence of mNG. (B) The average fluorescence intensity of a serial dilution of purified mNG. R = 0.9938.

Table 7.1 fluorescence intensity from transfected and untransfected HT1080 cells

	Total Protein concentration $mgmL^{-1}$	**mNG concentration $ngmL^{-1}$**	**mNG proportion of total protein $ngmg^{-1}$**
UT	0.400	0.000	0.000
CMV1	0.154	0.130	0.084
CMV2	0.177	0.086	0.074

7.6 Discussion

7.6.1 Optimising AA treatment time

The results of AA treatment time optimisation revealed that collagen could be synthesised and secreted in the absence of AA in BJ hTERT (figure 7.1 B-C). This has also been observed in mice lacking the enzyme gluanolacton oxidase which is essential to convert vitamin C to AA. These mice were still able to synthesise and secrete collagen (Parsons et al., 2006). It was also observed that the longer cells were exposed to AA, the fewer low molecular weight bands there were below the 150 kDa collagen1α2 band of the deposited collagen. The higher molecular weight bands above the 250 kDa collagen1α1 became more intense as AA treatment time was increased (figure 7.1 C). Together, these findings are consistent with the notion that, although some collagen can be produced and deposited in the absence of AA, collagen degradation is reduced in the presence of AA.

Lower amounts of secreted collagen from 5 day AA treated BJ hTERT cells could also be explained as collagen concentration increases and soluble matrices form, resulting in a lower collage concentration in the media (De Clerck & Jones, 1980). Although this is unlikely to happen in the absence of fibronectin (Sottile et al., 2007). There is also a low amount of collagen I present in the media of HT1080 cells which have not been treated with AA, while this might be due in part to deposition, it may also be a result of cell death and will need further investigation (figure 7.1 C). The experimental design should be changed in further investigations in order to account for any insoluble collagen which is deposited by cells, and will therefore be included in the cell lysate rather than the media. Perhaps addition of enzymes to the media which will degrade any ECM material prior to scraping could provide clearer insight into the proportion of soluble collagen versus insoluble deposited collagen.

7.6.2 Collagen exocytosis

Bursts of mNG-COL1α2 exocytosis were observed with TIRF microscopy in three HT1080 cells in the absence of AA. Bursts occurred in distinct locations at the cell periphery (figure 7.2 A). It is likely that these locations are fibripositors; regions from which collagen fibrils pre-form within the cell and are then secreted on masse into the ECM to form mature collagen fibres. Fibripositors have been characterised in the literature and identified as the end location of directed traffic of post-Golgi collagen carriers (section 6.6.5).

The fluorescence intensity of the burst was measured over time. This revealed a characteristic change in fluorescence intensity during bursts (figure 7.2 C-E). Following the burst, the fluorescence intensity of the region does not return back to 0, although this might be due to the presence of background signal in the cell and ECM, or residual mNG-COL1α2 in the area around the burst. The burst size, vesicle size, and static time prior to burst was also recorded and found to be similar for all bursts measured (figure 7.2 F-G).

Characterisation of the burst events by a long stationary time at the PM prior to exocytosis indicates that a regulated process controls these events, likely involving a number of checks to ensure that the procollagen is completely processed and ready to be secreted. It would be fascinating to identify the underlying process and proteins involved in burst regulation using biochemical and genetic approaches.

TIRF imaging has led to the characterisation of highly predictable burst events underlying the process of collagen exocytosis. The post-Golgi carriers tend to be found in discrete locations at the periphery of the basal PM. Carriers are of a similar size and area, and persist in the location of the burst for a long time prior to the event. The burst itself can be characterised by a distinctive change in fluorescent intensity of the region and by the formation of a fluorescent cloud outside of the cell which also has a predictable size (figure 7.3). This makes burst events distinct from movement of post-Golgi carriers in the cytosol. The persistence of the collagen cloud in the ECM could be investigated further using deep learning to de-noise the images and produce higher contrast images showing the cloud morphology.

7.6.3 Collagen deposition in the ECM

Collagen deposited by Saos-2 cells in 2D was visualised by confocal microscopy. The fibrils are clearly observed outside of the cell as determined using a cell mask stain (figure 7.4). The fibrils from all cells have a similar length and width, which is typical of the highly predictable structure of collagen. It would be interesting to observe the deposited fibrils by 3D SIM to determine the orientation of the collagen within the fibril and determine if it correlates with known assembly patterns from the literature (Goldberga et al., 2018; Orgel & Madhurapantula, 2019). The deposited fibrils should also be observed by electron microscopy or CLEM, to determine if the fibrils have the same ultrastructure as those produced endogenously in the bone (Linden et al., 1955).

7.6.4 Novel fluorescence assay to quantify collagen production

Deposited collagen can also be detected with a novel assay. A number of controls and optimisation experiments are needed before this assay can be used for high throughput collagen I quantification. Optimisation of sample volume and throughput is required before this assay can be used commercially. In professional collagen secreting cell lines, the presence of endogenous collagen will need to be controlled and taken into account. Eventually this assay could be used with stably transfected cells grown and treated within a 96-well plate. The growth media can be moved to a different well prior to cell lysis, to compare the concentration of intracellular and secreted collagen in the presence of bioactives. Although this would require further investigation into the proportion of soluble and insoluble collagen within the media and deposited by the cells (discussed in section 7.6.1). The end result will be a high throughput, reproducible and inexpensive assay to quantify collagen I production and secretion.

8 Final Discussion

8.1 Research scope

An mNG-COL1α2 fusion construct has been designed for high resolution and real time imaging of collagen I. Collagen I is a fibrillar component of the ECM, where it provides structure and support to most connective tissues. Collagen I is the main component of the skin ECM and its production is decreased as we age, leading to a loss of elasticity and the formation of wrinkles (Varani et al., 2006). Collagen I is therefore a target of cosmetic research. The overall aim of this thesis was to investigate the expression and trafficking of mNG-COL1α2 and its application across a range of research settings, including academia, research and cosmetics. To achieve this, four aims were laid out in section 1.5. In this section the extent to which these aims have been met by the research in this thesis will be discussed.

8.1.1 Defining suitable controls and characterising expression in cell lines of interest

8.1.1.1 Characterisation of expression

Characterisation of mNG-COL1α2 expression was achieved in three immortalised cell lines: HT1080 fibrosarcoma, BJ hTERT dermal fibroblast, and Saos-2 osteosarcoma. The intracellular distribution of collagen was visualised in each cell line by live confocal imaging (figure 4.2). In BJ hTERT cells collagen I was found in large static structures distributed evenly throughout the cell. In Saos-2 and HT1080, collagen I was found in a large central mass with smaller, more motile peripheral vesicles. In the literature, similar distributions of collagen I have been observed in fibroblast and osteoblast cells by immunofluorescence (De Oliveira et al., 2003; Gay et al., 1976). The peripheral movement and size of collagen carriers in HT1080 and Saos-2 cells were determined to have an average velocity of 0.45 μms^{-1}. In a study of the movement of collagen I carriers in myoblasts, an average vesicle velocity of 0.45 μms^{-1} was also observed (Kamata et al., 2017). Therefore, observations of mNG-COL1α2 distribution and dynamics in three cell lines of interest are consistent with previous observations published in the literature.

In HT1080 cells mNG-COL1α2 expression was further characterised. FRAP was used to provide insights into the dynamics of collagen movement within the cell periphery, especially the dynamics of vesicle movement (figure 4.3). A TET induction time course experiment was used to show that collagen is synthesised as little as 30 min after initiation of transcription, then collagen can be secreted into the ECM 3 hr following addition of TET (figure 4.4). Future experiments should involve repeating that FRAP and TET induction studies in BJ hTERT and Saos-2 cells.

8.1.1.2 Construct controls

To determine if the mNG tag was retained on collagen1α2 expressed by cells of interest, collagen and mNG were identified by SDS PAGE and western blotting, and with native gel analysis by fluorescence excitation. This provided compelling evidence that mNG is retained on expressed collagen1α2 in HT1080 and Saos-2

cells, providing confidence that mNG signal in images of these cells is representative of collagen. However, this experiment was inconclusive for mNG-COL1α2 expression in BJ hTERT cells (figure 5.1). Gel electrophoresis provided ambiguous evidence that mNG-COL1α2 could trimerise with endogenous collagen1α1 in Saos-2 cells (figure 5.2). Immunoprecipitation and LC-MS proteomics could be used in future experiments to address both the retention of mNG on collagen1α2 in BJ hTERTs and mNG-collagen1α2 heterotrimerisation in Saos-2 cells. As LC-Ms can be used to detect collagen peptide fragments and recognise mNG (Doan et al., 2019; Lalande et al., 2018; Simon et al., 2016).

The results of HT1080 cell treatment with BFA and CHX are consistent with the targeting of the mNG-COL1α2 to the ER during translation and movement through the cell secretory pathway, indicating that mNG-COL1α2 is trafficked through the same intracellular pathway as native collagen1α2 (figure 5.3-5.4). Although given the pleotrophic effects of these drugs, further controls are required for these experiments to mitigate for any off target effects which might result in altered collagen trafficking. These experiments could be repeated in Saos-2 and BJ hTERT cells to confirm that mNG-COL1α2 trafficking is consistent with HT1080 in these cell types. To determine if production of mNG-COL1α2 results in ER stress, XBP1 splicing assays could be carried out in all cell lines of interest (Calfon et al., 2002; Kishino et al., 2017). Co-immunoprecipitation to identify collagen interacting proteins within the ER should be carried out to provide insights into the ER processing of mNG-COL1α2 (Doan et al., 2019).

8.1.2 Visualising all stages of collagen I trafficking in real time with high resolution

The mNG-COL1α2 reporter was designed with mNG inserted into the N terminal globular domain of procollagen1α2 in such a way that resulted in the deletion of the N terminal ADAM cleavage site (figure 3.2). The aim here was to permit visualisation of intracellular collagen I trafficking and the extracellular assembly of collagen fibrils, through the prevention of N terminal cleavage which typically occurs following collagen deposition (section 1.3.5). The use of the mNG fluorophore, which is brighter and has a longer half-life than GFP, combined with confocal imagining with airyscan would allow live imaging over long time periods, with a higher resolution than has previously been achieved in the field. This is important to allow a full understanding of all stages of collagen trafficking.

Intracellular trafficking of mNG-COL1α2 has been best characterised within HT1080 cells. Treatment of HT1080 cells with CHX and BFA clearly show that mNG-COL1α2 is synthesised directly into the ER, and is trafficked through the ER to the Golgi (figure 5.3-5.4). Furthermore, the TET time course experiment clearly shows sequential filling of the ER then Golgi with mNG-COL1α2 signal, before the production of collagen carriers (figure 4.4). The live images of intracellular collagen I trafficking presented in this thesis have a greatly increased resolution compared to recently published work using collagen I GFP fusion

proteins, although further research should be done identifying the intracellular trafficking process within BJ hTERT and Saos-2 cells (Lu et al., 2018; McCaughey et al., 2019).

mNG-COL1α2 has also been used to successfully visualise collagen I within the ECM. TIRF microscopy has been utilised to visualise mNG-COL1α2 exocytosis from the basal membrane of HT1080 cells. These data provide proof that mNG-COL1α2 is deposited from the cell and have been used to characterise collagen carrier dynamics immediately prior to exocytosis (figure 7.2-7.3). This result is also very exciting, because high resolution imaging has allowed a novel observation of collagen exocytosis.

Laser scanning confocal microscopy with airyscan also shows that mNG-COL1α2 can be secreted from the cell and found in the ECM. In a 2D culture of Saos-2 cells, deposited collagen forms fibrils around the outside of the cells following 24 hr treatment with 200 μM AA (figure 7.1, 7.3). The deposited fibrils are of a uniform diameter typical to collagen fibrils observed in the literature (Raspanti et al., 2018). Literature suggests that maximum collagen deposition occurs following at least 5 days in 2D culture on fibronectin coated plastic (Almeida et al., 2018; Komatsu et al., 2018). In order to achieve this, stably transfected Saos-2 will need to be used to allow 5 days of collagen deposition and ensure that all cells within an area are secreting collagen.

8.1.3 Application of mNG-COL1α2 to biological questions

Within the field of collagen biology, the process of collagen packaging in the TGN and trafficking toward the PM is poorly understood. It is known that the regulation of sorting and distribution of secretory proteins occurs during TG-to-PM trafficking (Di Martino et al., 2019.; Presley et al., 1998). An expansion of the TGN following activation of collagen secretion has been observed, identifying collagen as a key protein processed and trafficked through the TGN (Ueno et al., 2010). The expression of collagen by dermal fibroblasts changes in response to mechanical stimuli, increasing for example following wounding to form a scar (Bainbridge, 2013). As part of this process there will be increased trafficking of collagen from the TGN to the PM, and it is essential that collagen is correctly trafficked and deposited in this situation. This thesis has investigated the role of the microtubule and actin cytoskeletons, and their associated motor proteins, in TGN to PM trafficking (section 6.0). A model for collagen I trafficking from TGN-to-PM is proposed using results from this thesis and current literature (figure 8.1).

8.1.3.1 Fission of collagen carriers at the TGN

To begin the TGN-to-PM trafficking process, collagen I is packaged into secretory carriers at the TGN. Throughout this research, collagen I carriers are observed as variable structures; with a wide range of morphologies and sizes observed within a single cell. The size of the collagen I carriers make complete dependence on clathrin or COP coats unlikely (section 6.2). When the cells are treated with Lat B, or sodium

azide/2-deoxy-d-glucose, fewer collagen I carriers are produced from the TGN and they are larger in size than those in untreated cells (figure 6.4-6.5). Conversely, when the cells are treated with colchicine there are fewer collagen I carriers produced from the TGN and they are smaller in size than those in untreated cells (figure 6.2). Together these results indicate that the actin and microtubule cytoskeletons are highly important in the regulation of collagen carrier formation and fission at the TGN.

A literature search to identify the underlying molecular components of collagen carrier formation at the TGN was conducted. Six COP and clathrin independent mechanisms of large carrier formation at the TGN are currently characterised. Of the 6 mechanisms outlined, the best candidate for collagen I carrier is the Rab6 positive carrier (Stalder & Gershlick, 2020). *In vitro* pull down assays have shown that an interaction between Rab6 and the actin binding protein non-muscle myosin IIA is critical for fission of post-Golgi carriers. Deletion of myosin IIA, or microtubule motor KIF20A which also interacts with Rab6, prevents fission of post-Golgi carriers (Miserey-Lenkei et al., 2017; Vicente-Manzanares et al., 2009). A pull down assay has shown that collagen V is a cargo of Rab6 positive carriers, although they have not yet been associated with the traffic of collagen I (Fourriere et al., 2019). These data fit observations from this thesis that depolymerising the actin or microtubule cytoskeletons prevents correct fission of collagen carriers from the TGN. However, in the absence of a clear link between Rab6 positive carriers and collagen I, this molecular mechanism is speculative. All that is known for certain is that both the actin and microtubule cytoskeleton and some of their motors are involved in collagen I carrier formation and fission from the TGN. It could be that this occurs through a completely novel mechanism to the six currently characterised.

8.1.3.2 Collagen carrier trafficking through the cytosol

Following collagen carrier fission from the TGN the carrier must be trafficked through the cytosol to the cell periphery. Treatment of cells with Lat B, taxol or colchicine showed that disruption or stabilisation of the microtubule cytoskeleton resulted in a decrease in the average velocity and displacement of collagen carriers, while disruption of the actin cytoskeleton did not result in a significant change in vesicle dynamics (figure 6.3-6.4). A relationship between collagen and microtubules has been observed within the literature, which points to collagen being organised parallel to microtubules (Zylberberg et al., 1988).

Treatment of cells with sodium azide and 2-deoxy-d-glucose also significantly reduce both average collagen carrier velocity and displacement, indicating the role of a microtubule motor protein in this process (figure 6.5). The only microtubule motor protein known to be involved in the trafficking of collagen I is KIF5A, which is associated with transport of collagen I carriers in myoblasts (Kamata et al., 2017). When KIF5A is knocked down in platelets, collagen I production for clotting is reduced, and in KIF5A knockdown mice, collagen I deposition is inhibited in the cartilage (Adam et al., 2018; He et al., 2017). Although KIF5A has not been directly related to collagen I trafficking and deposition in the skin, these data show it is likely to

be involved in collagen I trafficking in the skin, although it may work alongside other kinesins or transport mechanisms. Together these results lead to a model where collagen I carriers are trafficked from TGN-to-PM along the microtubule cytoskeleton in a KIF5A dependent process (figure 8.1).

8.1.3.3 Collagen I deposition at fibripositors

During transport through the cell cytosol, collagen carriers were observed to undergo directed trafficking toward particular regions of the cell PM. These points have been termed fibripositors and are tiny, finger-like projections of the PM which collagen is trafficked to and secreted into the ECM from (Canty et al., 2004; Kapacee et al., 2008). Fibripositors are known to be actin based structures, and movement of collagen at these points is dependent upon non-muscle myosin II (Canty et al., 2006; Kalson et al., 2013; figure 8.1).

On its journey to fibripositors, procollagen I is known to undergo some fibrilogenesis, with collagen fibrils anywhere between 1-30 μm in length reaching the PM (Humphries et al., 2008). These results fit with consistent observations of collagen carriers having a highly variable size (figure 6.1). Perhaps collagen carriers of a larger size contain longer collagen fibrils, and this would explain why large pleomorphic structures are found closer to the PM and in fibripositor regions (figure 6.1). TIRF data to observe collagen exocytosis reveals that collagen carriers remain stationary at the PM for a long time prior to burst (figure 7.2). This is potentially a result of interactions with the actin cytoskeleton and myosin II, ensuring that the carrier is correctly positioned and ready for the burst, although this still needs to be confirmed (figure 8.1). Furthermore, it was observed that the collagen cloud size following bursts was highly variable (figure 7.3). It is likely that cloud size is related to collagen carrier size, with larger carriers having more cargo and therefore producing a larger cloud upon burst.

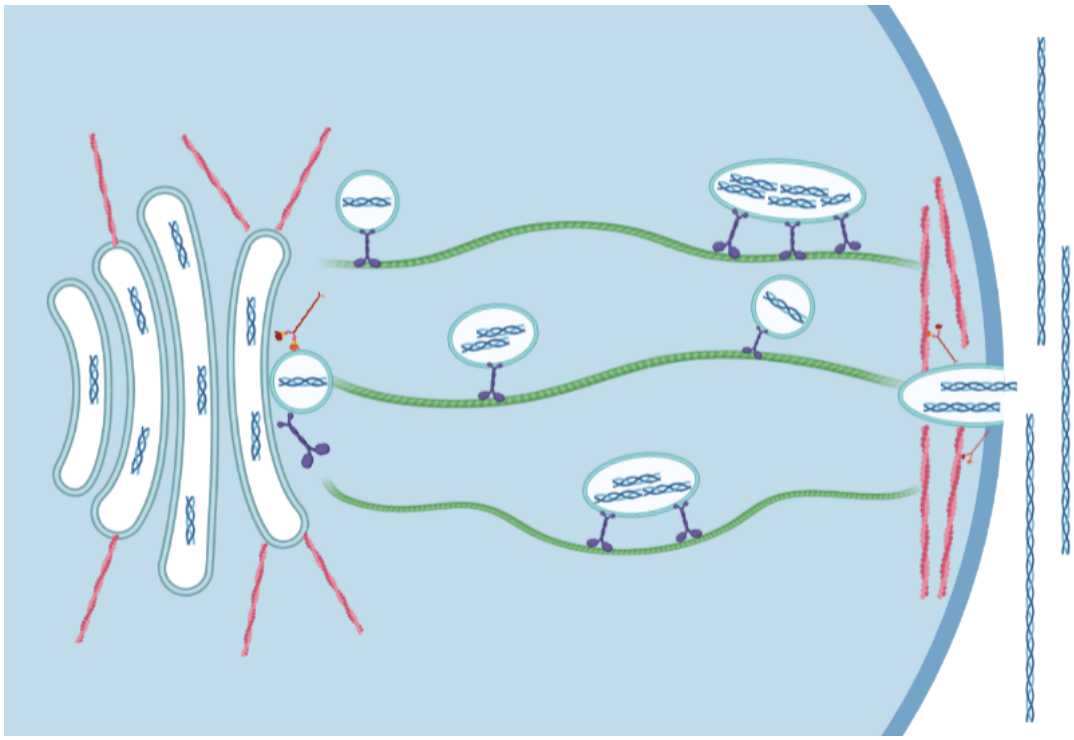

Figure 8.1 schematic to show proposed model of collagen I trafficking from Golgi to PM. Collagen in blue, actin in red, myosin II in orange, kinesin in purple, microtubules in green.

8.1.3.4 A model for Golgi-to-PM trafficking of collagen I

The experimental data from this thesis and data from the literature have been put together to suggest a model of collagen trafficking from Golgi-to-PM (figure 8.1). This model is tentative, and many of the molecular components have been selected as likely candidates from a literature search. Biochemical characterisation these components is required to validate this model. This model currently does not consider collagen I carriers which are trafficked from the Golgi to the autosomal system, or endosomal carriers which are used to recycle collagen I from the ECM (Bi et al., 2014; Omari et al., 2018). However, this has shown the relevance of mNG-COL1α2 as a tool to answer academic questions related to the biology of collagen trafficking.

A COL1α1-GFP tool has been used by other researchers to investigate the traffic of collagen from ER to Golgi, another elusive question within the field and was contested for a long time (McCaughey et al., 2019). The use of the mNG-COL1α2 construct with high resolution imaging is a natural progression from this work, because it allows longer term and higher resolution imaging than achieved in this paper. It also allows clearer imaging in the cell periphery, where the changing pH would have reduced the brightness of GFP (Shorter et al., 2017).

8.1.4 Application of mNG-COL1α2 to cosmetic questions

8.1.4.1 ATPeptide

ATPeptide™ is an 'energy-boosting peptide specially designed to help revitalise aging skin' (Ashland Industries Ltd). Following a 24 hr treatment with 2.5 ppm ATPeptide, HT1080 cells contain significantly more mNG-COL1α2 than untreated control cells, while the dynamics of collagen trafficking remained unchanged (figure 6.7). This result indicates that ATPeptide treatment can increase the production of collagen without changing the underlying trafficking process. Ashland Industries report that ATPeptide supports maintenance of ATP levels *in vitro*, although no study or peptide sequence of ATPeptide is yet published to support this claim (Ashland Industries Ltd). The result in this thesis showing increased collagen production from ATPeptide treated cells does support this claim. ATP plays a central role in protein translation: used directly in the charging of tRNA with peptides, indirectly in ribosome translation along mRNA, and plays an important role in ribosome recycling (Hellen, 2018; Pontes et al., 2015; Rodnina & Wintermeyer, 2011). This explains how ATPeptide is able to increase collagen production in the cell, through increases in ATP which result in increased translation, and increased collagen will help to revitalise skin (Varani et al., 2006).

In the absence of a peptide sequence and structure for ATPeptide, which are currently protected by copyright laws, the mechanism of ATPeptide action cannot be further characterised. ATPeptide should be tested in an *in vivo* system, to confirm that increase collagen production can be observed in a more relevant system (section 8.3.1). Further experiments should also be done to ensure that the increased collagen production is of good quality, can form a normal ECM network, and that increased collagen synthesis does not result in intracellular stress. This might not be a collagen specific effect, but might result from overexpression of any protein. Overall, the mNG-COL1α2 construct has been used to show the effect of bioactive treatment upon cells in high detail and has provided insights into the mechanism of action of ATPeptide. Clearly the construct can also be used to determine the effects of other bioactives upon intracellular collagen trafficking in similar ways.

8.1.4.2 Novel Assay for collagen production

This thesis outlines a novel fluorescence based assay which utilises the mNG-COL1α2 construct fluorescence in order to quantify intracellular collagen production and extracellular collagen secretion. The assay uses a mNG standard curve in order to determine the fluorescence intensity of a known mNG concentration. Fluorescent signal from cell lysates, or cell growth media can then be used to quantify the intracellular and ECM mNG-collagen concentration, respectively (section 7.4). This assay still requires optimisation before it could be used in a high throughput industrial setting to test bioactives, but a proof of concept experiment yielded promising results (table 7.1).

A PubMed search of 'fluorescence assay collagen' reveals that assays currently defined in the literature to quantify collagen utilise fluorophore tagged CMPs. Such assays are highly effective for detecting misfolded or damaged collagen, because of the binding nature of CMPs (section 1.3.2). These assays have been used to determine the effect of different ECM proteins, compounds, and enzymes on collagen quality (Nian et al., 2018; Sano et al., 2004; Sun et al., 2019). Perhaps, once the fluorescence assay characterised in this thesis has been optimised, it could be combined with a red fluorophore tagged CMP to determine the proportion of collagen which is correctly folded. This would determine the effect of bioactives on the quality of the collagen in the cell and ECM, as well as the quantity. Such an assay has already been optimised for a microplate system (Lin et al., 2019). The assay outlined in section 7.4 could easily be adapted to incorporate this technology.

8.2 Continuing development of computational and technical methods

8.2.1 Vesicle Tracking

The research in this thesis would not have been possible without a number of recent technical advances within the field of biological imaging and computational biology. This project relied heavily on the use of Fiji plugin TrackMate which tracks objects of a size set by the user to provide data on the dynamics of the movement (Tinevez et al., 2017). Multiple other tracking algorithms are known and used, but TrackMate was deemed most appropriate for this project (Kalaidzidis, 2009). Despite being designed to track much larger bodies, such as cells or organelles, rather than vesicles, TrackMate performed well to provide insights into collagen vesicle movement in this research.

Due to its design for tracking larger particles, TrackMate did miss some subtler vesicle movements. For example, vesicles which moved out of the Z plane could be measured separately by TrackMate, and there was an issue in user bias when thresholding in initial vesicle detection. The software could not distinguish between different types of vesicle motion, often including Brownian motion or background organelle motion in tracks. This project has demonstrated the importance of understanding the dynamics which occur in living systems, and a key part of this is quantifying motion of intracellular objects. In this section alternative tracking methods which could be used as this research progresses will be discussed.

8.2.1.1 Single Particle Tracking

Single particle tracking is a technique in which individual fluorophores can be detected and tracked in a live sample. The most common method for single particle tracking involves the use of PALM: a type of super resolution microscopy in which photo switchable fluorophores undergo continuous cycles of activation, imaging, and photobleaching to provide flashes. The flashes allow multiple fluorophores which would be spatially indistinguishable under confocal microscopy to be visualised separately, and an exact

location of each fluorophore can be identified (Y. Lee et al., 2019). The trajectory of each fluorophore can then be tracked, either manually or using an automated tracking system (Manley et al., 2010).

mNG has photo switching ability and its use in PALM imaging has already been optimised (Stockmar et al., 2018). It is not unreasonable that with optimisation of sample preparation, mNG-COL1α2 single particle tracking could be achieved by PALM. This would allow quantification of the number of mNG-COL1α2 peptides within a single collagen carrier. It could also be used to provide insights into the fibrillogenesis which occurs within intracellular collagen vesicles and the integration of mNG-COL1α2 into extracellular fibrils, although the speed of the imaging might be limiting for this rapid process.

8.2.1.2 Deep Learning

Deep learning is increasingly being used for the analysis of biological images. In the deep learning process an algorithm is 'trained' against sample data to perform a particular analysis task on subsequent input images. The benefits of deep learning are that it removes user bias and interpretation from the analysis process, and it can be tailored directly to the users research questions during the training process (Moen et al., 2019). A number of deep learning programmes have been coded by different research groups for particle tracking (Arts et al., 2019; Yao et al., 2020). In the future of mNG-COL1α2 research these codes could be utilised in order to provide tracking which is not subject to user bias. This process would have to be optimised and sample images would have to be made to 'train' the code, which would require some optimisation. It might be the case that code would have to be written directly for this question, representing an exciting opportunity for inter-disciplinary research.

8.2.2 mNG-COL1α2 use in complex systems

The immortalised cell lines used in this thesis are highly appropriate for the nature of this research. The cell lines are well characterised and ensure reproducibility when designing and carrying out initial research on the mNG-COL1α2 construct. However, immortalised cell lines in a 2D culture system are not an accurate model of human skin. The immortalisation of cells involves dysregulation of several essential cell cycle check points, which can cause mutations and a loss of normal physiological behaviour (Maqsood et al., 2013). To begin to more accurately study collagen I trafficking in skin with mNG-COL1α2, the construct could be used in primary fibroblast cell lines. Primary cells could then be used in complex systems, discussed in this section, to provide a closer biological replicate of collagen trafficking (Seluanov et al., 2010).

8.2.2.1 mNG-COL1α2 in 3D tissue culture for skin modelling

All experiments in this thesis have taken place in 2D tissue culture conditions due to the need for characterisation in a simple system. Going forward the mNG-COL1α2 construct could be used to observe

collagen production and deposition from stable transfected or knock-in primary cells in a 3D culture system. Many 3D systems better replicate the physiological conditions of tissue and allow co cultures of different cell types to mimic *in vivo* intercellular communication, while improving cell viability (Betriu et al., 2020; Bonnier et al., 2015). There are a number of well characterised and replicable 3D skin culture models of varying complexity to investigate different biological questions (Zeitvogel & Werfel, 2020).

While 3D cultures would allow visualisation of mNG-COL1α2 trafficking from different cell types in a more biologically relevant environment than 2D culture, the increased complexity and thickness of the model would make it difficult to image collagen with the high resolution achieved in this thesis. Two methods to address this issue have been outlines in the literature. The first is the de-cellularisation of the model to allow high resolution of the collagen matrix following deposition from the cells (Benny et al., 2016). This method comes with the obvious caveat that intracellular collagen trafficking cannot be imaged. The second involves sectioning of the model to provide insights into the interactions between cells of the model and the ECM that forms around them (Short et al., 2017).

Neither of these methods is appropriate for live imaging. Potential methods to allow live imaging of collagen trafficking in a complex model with high resolution might include low resolution live imaging, followed by fixation and expansion microscopy of the model to provide a high resolution (Tillberg & Chen, 2019; Wassie et al., 2019). An alternative solution might be to use CLEM, to permit low resolution live imaging, followed by fixation and sectioning of the model, and immunogold staining against mNG to provide corresponding high resolution images (Hanein & Volkmann, 2011; Koike & Yamada, 2019).

Imaging of mNG-COL1α2 trafficking and deposition in a 3D skin model will have huge applications within current research. Human skin models are highly important in the cosmetic industry, as they provide an ethical alternative to animal testing, and are very effective in mimicking the reactions of real skin to cosmetic products (Ma et al., 2020). Such models have already been used to test antiaging products, thus the use of mNG-COL1α2 in a human tissue model would be highly informative of the anti-aging properties of a bioactive (Khmaladze et al., 2020). In an academic setting, mNG-COL1α2 in a 3D skin model could be used to investigate the role of mechanical stress or substrate stiffness on collagen deposition, or the role of collagen deposition in scarring (Aragona et al., 2020; Leavitt et al., 2016).

8.2.2.2 mNG-COL1α2 in transgenic organisms

Within the field, transgenic model organisms expressing GFP-Col1α2 constructs have been created and used to investigate collagen deposition within different tissues. Transgenic zebrafish expressing a GFP-Col1α2 construct have been used to study collagen deposition during wound healing and scarring in real

time (Morris et al., 2018). Transgenic mice expressing a GFP-COL1 reporter construct have been used to investigate liver fibrosis in tissue samples from the organisms (Iwaisako et al., 2014; Nishio et al., 2019).

Due to the ease of live imaging with light sheet microscopy, zebrafish represent a promising organism in which deposition of mNG-COL1α2 can be imaged live, with the use of the mNG tag permitting longer imaging times than those of GFP. Due to the ethical barriers associated with the use of live organisms and creation of transgenic organisms, this is not an appropriate application for cosmetic research, and should be restricted to academic investigation of skin growth, scar formation, and collagen deposition during embryonic development in real time (Keller et al., 2008; Meinert & Rohrbach, 2019).

8.3 Future applications of mNG-COL1α2

This thesis has shown that mNG-COL1α2 visualises collagen trafficking within living cells. Given the success of the mNG tag for visualisation of collagen I within live cells, this idea of tagging proteins could be applied to other research questions. In this section, two future applications of the mNG tag to study ECM biology are discussed.

8.3.1 Tagging other collagen proteins

A total of 28 collagen proteins are found within the human body. Similar to collagen I, all collagen proteins are characterised by primary sequence triplet repeats, most commonly Gly-X-Y where X and Y are proline and hydroxyproline respectively. The unusual primary sequence of the collagen proteins gives rise to the triple helical tertiary structure unique to the collagen family (Ricard-Blum, 2011). Mature collagen proteins are found in the ECM of connective tissues, where they provide support and structure, and can take part in mediation of cell signalling, differentiation and migration (Myllyharju & Kivirikko, 2001). Given the success of mNG-COL1α2 demonstrated in this thesis, the mNG fluorophore could be used to tag and visualise other collagen proteins in future research. Very little work has been done within the literature to add a fluorescent tag to other collagen proteins, with collagen I being the only successfully tagged collagen. The different structures of the collagen proteins make some more viable targets than others, this is demonstrated by the case studies of collagen III and collagen VI.

Like collagen I, collagen III is a fibrillar collagen found abundantly within the skin to provide support and structure to the tissue (Karsdal et al., 2017). Collagen I and collagen III production decreases in aged skin, contributing to the formation of wrinkles and loss of skin elasticity (Varani et al., 2006). To correctly understand the anti-aging effects of a bioactive on the skin, collagen I and collagen III must be considered together. Due to the fibrillary nature of both collagen I and III, the two proteins have a similar structure and undergo similar processing, trafficking, and secretory processes. Collagen III is a homotrimer of the collagen3α1 peptide, encoded for by the COL3α1 gene. The collagen III propeptide triple helix has globular

N and C terminal domains similar to collagen I which are cleaved by ADAM proteinases in the ECM to allow formation of mature fibrils (S. P. Boudko et al., 2008; Kuivaniemi & Tromp, 2019). A mNG-COL3α1 construct could be designed in a similar fashion to mNG-COL1α2, with deletion of the N terminal cleavage domain to visualise intracellular and extracellular trafficking of collagen III. Collagen III homotrimerisation would result in some mNG signal amplification. Because the number of fluorophores in each collagen III propeptide would be three, this could be mitigated for in data analysis.

Collagen VI is a non-fibrillary collagen found throughout the skin where it directs dermal matrix assembly and influences dermal fibroblast behaviour, making it particularly important in the mediation of processes such as wound healing (Theocharidis et al., 2016). Collagen VI is also thought to have an anchoring structure and may be involved in the function of the basement membrane, although much of collagen VI biology is currently unknown (Groulx et al., 2011; Keene et al., 1988). Collagen VI is a heterotrimer of the collagen6α1, collagen6α2, and collagen6α3 proteins which are encoded for by 3 genes on chromosome 9: COL6α1 COL6α2 and COL6α3. COL6α3 is alternately spliced in specific cell types to give rise to the collagen6α4, collagen6α5, and collagen6α6 proteins (Fitzgerald et al., 2013; Zanussis et al., 1992). Each chain of collagen VI has a central Gly-X-Y triple helical domain flanked by N and C terminal globular domain, although collagen VI has the lowest proportion of triple helical sequence of any collagen (Chu et al., 1990; Maaß et al., 2016).

Tagging the COL6α1 or COL6α2 gene with mNG could help to provide insights into the role of collagen VI within the skin. The COL6α3 gene is not a suitable target of tagging due to its complex nature and splice variants. However, a collagen VI fluorophore fusion construct will be difficult to design as research shows that a large number of mutations in the collagen VI gene will result in disease phenotypes (Antoniel et al., 2020; Butterfield et al., 2013). A collagen VI mNG fusion construct will have to be carefully designed to ensure that biological function is preserved. Alternatively, mNG could be introduced in such a way that would allow a novel construct to mimic a disease phenotype.

8.3.2 Wider investigation of the ECM

Although this thesis has focused on collagen trafficking and its deposition into the ECM, it is important to consider that the ECM is a complex 3D structure, made up of a number of different fibrillary proteins, including fibronectin, elastins, lamins, proteoglycans and a range of other glycoproteins (Theocharis et al., 2016). As we age, collagen, and many other ECM proteins are modified and degraded, leading to a decrease in tissue support and the appearance of wrinkles and aged skin (Birch, 2018).

Real time imaging of multiple ECM components within the skin has not yet been achieved within the field. Most ECM imaging is currently achieved through immunostaining in fixed tissues, or for live imaging

through techniques such as SHG and CRM which utilise the native optical properties of the ECM (section 1.3). Immunostaining is limited by its use in fixed tissue sections only, and live imaging with SHG and CRM is limited by difficulties distinguishing between different ECM components with similar properties (Mayorca-Guiliani et al., 2019; Zeug et al., 2014; section 1.3).

Given the success of the mNG-COL1α2 construct for visualisation of collagen both within the cell and within the ECM, it would be very interesting to make similar mNG constructs with other ECM proteins. Each protein would need to be considered individually to make a construct which would allow optimal visualisation within the cell and in the ECM. Different coloured fluorophores could even be used together to visualise interactions between different deposited ECM components and identify differences and similarities in intracellular trafficking pathways. This would be hugely beneficial in the skincare industry, allowing the effect of bioactives on the entire ECM to be imaged in real time. It would also have impacts in academia, allowing restructuring of the ECM in response to external stimuli to be visualised

8.4 Concluding remarks

In this thesis, an mNG- COL1α2 fusion construct has been designed and created, with the aim of visualising collagen I trafficking with high resolution in real time. The expression of mNG-COL1α2 was characterised in three immortalised cell lines of interest, and its expression controlled for. The construct has been successfully used to image collagen trafficking live within the cell, through all stages of intracellular trafficking, and extracellular deposition has been observed in a 2D culture. mNG-COL1α2 has been used to address biological and industrial questions, providing unique insights into Golgi-to-PM trafficking and the antiaging properties of the bioactive ATPeptide. Overall, the mNG-COL1α2 fusion construct is a robust, replicable, and effective tool to study collagen I trafficking.

Going forward, research could focus on improving the techniques underlying this project. Improving the microscopy used for data acquisition and image analysis, and moving the mNG-COL1α2 construct into primary cell lines and *in vitro* skin models which will allow a more biologically relevant investigation of collagen trafficking. Eventually, the technology in this project can be applied to make fusion constructs of other collagen or even ECM proteins, providing insights into the wider context of skin biology.

9 Supplementary data

To determine statistical significance of the data displayed in figures 6.3, 6.4, 6.5 and 6.6, Student's T tests were performed. The results are found in the following tables:

Table S1 Students T test of vesicle velocity at 0 and 30 min after treatment with 5 μM taxol in 3 independent cells

	T value	T critical	P value
Cell 1	2.93	1.66	<0.01
Cell 2	3.74	1.70	<0.01
Cell 3	2.06	1.72	0.03

Table S2 Students T test of vesicle displacement at 0 and 30 min after treatment with 5 μM taxol in 3 independent cells

	T value	T critical	P value
Cell 1	10.05	1.66	<0.01
Cell 2	7.58	1.70	<0.01
Cell 3	2.17	1.72	0.02

Table S3 Students T test of vesicle velocity at 0 and 120 min after treatment with 5 μM colchicine in 3 independent cells

	T value	T critical	P value
Cell 1	0.43	1.66	0.33
Cell 2	10.62	1.65	<0.01
Cell 3	3.77	1.65	<0.01

Table S4 Students T test of vesicle displacement at 0 and 120 min after treatment with 5 μM colchicine in 3 independent cells

	T value	T critical	P value
Cell 1	0.39	1.66	0.37
Cell 2	10.68	1.65	<0.01
Cell 3	12.67	1.65	<0.01

Table S5 Students T test of vesicle velocity at 0 and 90 min after treatment with 5 μM Lat B in 3 independent cells

	T value	T critical	P value
Cell 1	2.39	1.66	0.01
Cell 2	1.72	1.72	0.05
Cell 3	1.71	1.76	0.05

Table S6 Students T test of vesicle displacement at 0 and 90 min after treatment with 5 μM Lat B in 3 independent cells

	T value	T critical	P value
Cell 1	1.57	1.66	0.05
Cell 2	0.86	1.72	0.20
Cell 3	0.17	1.76	0.43

Table S7 Students T test of vesicle velocity at 0 and 120 min after treatment with 0.05% sodium azide and 50 μM 2-deoxy-d-glucose in 3 independent cells

	T value	T critical	P value
Cell 1	4.26	1.70	<0.01
Cell 2	3.18	1.66	<0.01
Cell 3	4.69	1.65	<0.01

Table S8 Students T test of vesicle displacement at 0 and 120 min after treatment with 0.05% sodium azide and 50 μM 2-deoxy-d-glucose in 3 independent cells

	T value	T critical	P value
Cell 1	6.62	1.70	<0.01
Cell 2	3.73	1.66	<0.01
Cell 3	1.68	1.65	0.05

Table S9 Students T test between control HT1080 cells and HT1080 cells treated for 24 hr with 2.5 ppm ATPeptide.

	T value	T critical	P value
Cell fluorescence intensity	5.21	1.76	<0.01
Vesicle Fluorescence intensity	5.95	1.76	<0.01
Average vesicle number	0.52	1.76	0.3
Average vesicle velocity	1.22	1.76	0.2
Average vesicle displacement	0.10	1.76	0.5

10 References

Adam, F., Kauskot, A., Kurowska, M., Goudin, N., Munoz, I., Bordet, J. C., Huang, J. D., Bryckaert, M., Fischer, A., Borgel, D., De Saint Basile, G., Christophe, O. D., & Ménasché, G. (2018). Kinesin-1 is a new actor involved in platelet secretion and thrombus stability. *Arteriosclerosis, Thrombosis, and Vascular Biology*, *38*(5), 1037–1051. https://doi.org/10.1161/ATVBAHA.117.310373

Ahn, S., Lee, K. Y., Parker, K. K., & Shin, K. (2018). Formation of Multi-Component Extracellular Matrix Protein Fibers. *Scientific Reports*, *8*(1), 1–6. https://doi.org/10.1038/s41598-018-20371-8

Almeida, P. N., Barboza, D. do N., Luna, E. B., Correia, M. C. de M., Dias, R. B., Siquara de Sousa, A. C., Duarte, M. E. L., Rossi, M. I. D., & Cunha, K. S. (2018). Increased extracellular matrix deposition during chondrogenic differentiation of dental pulp stem cells from individuals with neurofibromatosis type 1: an in vitro 2D and 3D study. *Orphanet Journal of Rare Diseases*, *13*(1), 98. https://doi.org/10.1186/s13023-018-0843-1

Ameri, A., Khodarahmi, G., Forootanfar, H., Hassanzadeh, F., & Hakimelahi, G. H. (2018). Hybrid Pharmacophore Design, Molecular Docking, Synthesis, and Biological Evaluation of Novel Aldimine-Type Schiff Base Derivatives as Tubulin Polymerization Inhibitor. *Chemistry and Biodiversity*, *15*(3). https://doi.org/10.1002/cbdv.201700518

An, W. F. (2009). Fluorescence-based assays. *Methods in Molecular Biology (Clifton, N.J.)*. https://doi.org/10.1007/978-1-60327-545-3_7

Antoniel, M., Traina, F., Merlini, L., Andrenacci, D., Tigani, D., Santi, S., Cenni, V., Sabatelli, P., Faldini, C., & Squarzoni, S. (2020). Tendon Extracellular Matrix Remodeling and Defective Cell Polarization in the Presence of Collagen VI Mutations. *Cells*, *9*(2), 409. https://doi.org/10.3390/cells9020409

Aper, S. J. A., Van Spreeuwel, A. C. C., Van Turnhout, M. C., Van Der Linden, A. J., Pieters, P. A., Van Der Zon, N. L. L., De La Rambelje, S. L., Bouten, C. V. C., & Merkx, M. (2014). Colorful protein-based fluorescent probes for collagen imaging. *PLoS ONE*, *9*(12), 1–21. https://doi.org/10.1371/journal.pone.0114983

Aragona, M., Sifrim, A., Malfait, M., Song, Y., Van Herck, J., Dekoninck, S., Gargouri, S., Lapouge, G., Swedlund, B., Dubois, C., Baatsen, P., Vints, K., Han, S., Tissir, F., Voet, T., Simons, B. D., & Blanpain, C. (2020). Mechanisms of stretch-mediated skin expansion at single-cell resolution. *Nature*, *584*(7820), 268–273. https://doi.org/10.1038/s41586-020-2555-7

Arts, M., Smal, I., Paul, M. W., Wyman, C., & Meijering, E. (2019). Particle Mobility Analysis Using Deep Learning and the Moment Scaling Spectrum. *Scientific Reports*, *9*(1), 1–10. https://doi.org/10.1038/s41598-019-53663-8

Atkinson, J. M., Falconer, R. A., Edwards, D. R., Pennington, C. J., Siller, C. S., Shnyder, S. D., Bibby, M. C., Patterson, L. H., Loadman, P. M., & Gill, J. H. (2010). Development of a novel tumor-targeted vascular disrupting agent activated by membrane-type matrix metalloproteinases. *Cancer Research*, *70*(17), 6902–6912. https://doi.org/10.1158/0008-5472.CAN-10-1440

BÄCHINGER, H. P., BRUCKNER, P., TIMPL, R., PROCKOP, D. J., & ENGEL, J. (1980). Folding Mechanism of the Triple Helix in Type-III Collagen and Type-III pN–Collagen: Role of Disulfide Bridges and Peptide Bond Isomerization. *European Journal of Biochemistry*. https://doi.org/10.1111/j.1432-1033.1980.tb04610.x

Bainbridge, P. (2013). Wound healing and the role of fibroblasts. *Journal of Wound Care*, *22*(8), 407–412. https://doi.org/10.12968/jowc.2013.22.8.407

Banushi, B., Forneris, F., Straatman-Iwanowska, A., Strange, A., Lyne, A. M., Rogerson, C., Burden, J. J., Heywood, W. E., Hanley, J., Doykov, I., Straatman, K. R., Smith, H., Bem, D., Kriston-Vizi, J., Ariceta, G., Risteli, M., Wang, C., Ardill, R. E., Zaniew, M., … Gissen, P. (2016). Regulation of post-Golgi LH3 trafficking is essential for collagen homeostasis. *Nature Communications*. https://doi.org/10.1038/ncomms12111

Bella, J, Eaton, M., Brodsky, B., & Berman, H. (1994). Crystal and molecular structure of a collagen-like peptide at 1.9 A resolution. *Science*. https://doi.org/10.1126/science.7695699

Bella, Jordi, Brodsky, B., & Berman, H. M. (1995). Hydration structure of a collagen peptide. *Structure*. https://doi.org/10.1016/S0969-2126(01)00224-6

Benny, P., Badowski, C., Lane, E. B., & Raghunath, M. (2016). Improving 2D and 3D Skin In Vitro Models Using Macromolecular Crowding. *J. Vis. Exp*, *114*, 53642. https://doi.org/10.3791/53642

Berg, R. A., & Prockop, D. J. (1973). The thermal transition of a non-hydroxylated form of collagen. Evidence for a role for hydroxyproline in stabilizing the triple-helix of collagen. *Biochemical and Biophysical Research Communications*. https://doi.org/10.1016/0006-291X(73)90961-3

Betriu, N., Jarrosson-Moral, C., & Semino, C. E. (2020). Culture and differentiation of human hair follicle dermal papilla cells in a soft 3D self-assembling peptide scaffold. *Biomolecules*, *10*(5). https://doi.org/10.3390/biom10050684

Bi, Y., Mukhopadhyay, D., Drinane, M., Ji, B., Li, X., Cao, S., & Shah, V. H. (2014). Endocytosis of collagen by hepatic stellate cells regulates extracellular matrix dynamics. *American Journal of Physiology - Cell Physiology*, *307*(7), C622–C633. https://doi.org/10.1152/ajpcell.00086.2014

Birch, H. L. (2018). Extracellular matrix and ageing. In *Subcellular Biochemistry* (Vol. 90, pp. 169–190). Springer New York. https://doi.org/10.1007/978-981-13-2835-0_7

Birk, D. E., Zycband, E. I., Winkelmann, D. A., & Trelstad, R. L. (1989). Collagen fibrillogenesis in situ: Fibril segments are intermediates in matrix assembly. *Proceedings of the National Academy of Sciences of the United States of America*. https://doi.org/10.1073/pnas.86.12.4549

Blau, H. M., & Rossi, F. M. V. (1999). Tet B or not tet B: Advances in tetracycline-inducible gene expression. In *Proceedings of the National Academy of Sciences of the United States of America*. https://doi.org/10.1073/pnas.96.3.797

Bonfanti, L., Mironov, A. A., Martínez-Menárguez, J. A., Martella, O., Fusella, A., Baldassarre, M., Buccione, R., Geuze, H. J., Mironov, A. A., & Luini, A. (1998). Procollagen traverses the Golgi stack without leaving the lumen of cisternae: Evidence for cisternal maturation. *Cell*. https://doi.org/10.1016/S0092-8674(00)81723-7

Bonnier, F., Keating, M. E., Wróbel, T. P., Majzner, K., Baranska, M., Garcia-Munoz, A., Blanco, A., & Byrne, H. J. (2015). Cell viability assessment using the Alamar blue assay: A comparison of 2D and 3D cell culture models. *Toxicology in Vitro*, *29*(1), 124–131. https://doi.org/10.1016/j.tiv.2014.09.014

Boudko, S., Frank, S., Kammerer, R. A., Stetefeld, J., Schulthess, T., Landwehr, R., Lustig, A., Bächinger, H. P., & Engel, J. (2002). Nucleation and propagation of the collagen triple helix in single-chain and trimerized peptides: Transition from third to first order kinetics. *Journal of Molecular Biology*. https://doi.org/10.1006/jmbi.2002.5439

Boudko, S. P., Engel, J., Okuyama, K., Mizuno, K., Bächinger, H. P., & Schumacher, M. A. (2008). Crystal structure of human type III collagen Gly991-Gly 1032 cystine knot-containing peptide shows both 7/2 and 10/3 triple helical symmetries. *Journal of Biological Chemistry*, *283*(47),

32580–32589. https://doi.org/10.1074/jbc.M805394200

Bowes, J. H., & Kenten, R. H. (1948). The amino-acid composition and titration curve of collagen. *The Biochemical Journal*. https://doi.org/10.1042/bj0430358

Brodsky, B., & Baum, J. (2008). Structural biology: Modelling collagen diseases. In *Nature*. https://doi.org/10.1038/453998a

Butterfield, R. J., Foley, A. R., Dastgir, J., Asman, S., Dunn, D. M., Zou, Y., Hu, Y., Donkervoort, S., Flanigan, K. M., Swoboda, K. J., Winder, T. L., Weiss, R. B., & Bönnemann, C. G. (2013). Position of glycine substitutions in the triple helix of COL6A1, COL6A2, and COL6A3 is correlated with severity and mode of inheritance in collagen vi myopathies. *Human Mutation*, *34*(11), 1558–1567. https://doi.org/10.1002/humu.22429

Cai, X., Liu, Z., Zhao, S., Song, C., Dong, S., & Xiao, J. (2017). A single stranded fluorescent peptide probe for targeting collagen in connective tissues. *Chemical Communications*, *53*(87), 11905–11908. https://doi.org/10.1039/c7cc06056d

Calfon, M., Zeng, H., Urano, F., Till, J. H., Hubbard, S. R., Harding, H. P., Clark, S. G., & Ron, D. (2002). IRE1 couples endoplasmic reticulum load to secretory capacity by processing the XBP-1 mRNA. *Nature*, *415*(6867), 92–96. https://doi.org/10.1038/415092a

Canty-Laird, E. G., Lu, Y., & Kadler, K. E. (2012). Stepwise proteolytic activation of type I procollagen to collagen within the secretory pathway of tendon fibroblasts in situ. *Biochemical Journal*. https://doi.org/10.1042/BJ20111379

Canty, E. G., & Kadler, K. E. (2005). Procollagen trafficking, processing and fibrillogenesis. In *Journal of Cell Science*. https://doi.org/10.1242/jcs.01731

Canty, E. G., Lu, Y., Meadows, R. S., Shaw, M. K., Holmes, D. F., & Kadler, K. E. (2004). Coalignment of plasma membrane channels and protrusions (fibropositors) specifies the parallelism of tendon. *Journal of Cell Biology*, *165*(4), 553–563. https://doi.org/10.1083/jcb.200312071

Canty, E. G., Starborg, T., Lu, Y., Humphries, S. M., Holmes, D. F., Meadows, R. S., Huffman, A., O'Toole, E. T., & Kadler, K. E. (2006). Actin filaments are required for fibripositor-mediated collagen fibril alignment in tendon. *Journal of Biological Chemistry*, *281*(50), 38592–38598. https://doi.org/10.1074/jbc.M607581200

Chang, J., Garva, R., Pickard, A., Yeung, C. Y. C., Mallikarjun, V., Swift, J., Holmes, D. F., Calverley, B., Lu, Y., Adamson, A., Raymond-Hayling, H., Jensen, O., Shearer, T., Meng, Q. J., & Kadler, K. E. (2020). Circadian control of the secretory pathway maintains collagen homeostasis. *Nature Cell Biology*, *22*(1), 74–86. https://doi.org/10.1038/s41556-019-0441-z

Chardin, P., & Mccormick, F. (1999). Brefeldin A: The Advantage Minireview of Being Uncompetitive of brefeldin A action might have important implications for drug discovery. By what mechanism does brefeldin A inhibit Arf1 ex. *Cell*, *97*, 153–155. https://blackboard.cornell.edu/bbcswebdav/pid-3936741-dt-content-rid-22558789_1/courses/10853_2018FA_COMBINED-CROSSLIST/BFAadvantageUncompetitive.pdf

Chazotte, B. (2010). Labeling cytoskeletal F-Actin with rhodamine phalloidin or fluorescein phalloidin for imaging. *Cold Spring Harbor Protocols*. https://doi.org/10.1101/pdb.prot4947

Chen, X., Nadiarynkh, O., Plotnikov, S., & Campagnola, P. J. (2012). Second harmonic generation microscopy for quantitative analysis of collagen fibrillar structure. *Nature Protocols*, *7*(4), 654–669. https://doi.org/10.1038/nprot.2012.009

Chen, Z., Liu, J., & Zhang, Y. (2017). Role of epithelial cell transforming sequence 2 (ECT2) in predicting prognosis of osteosarcoma. *Medical Science Monitor*, *23*, 3861–3868. https://doi.org/10.12659/MSM.905951

Choo, K. H., Tan, T. W., & Ranganathan, S. (2009). A comprehensive assessment of N-terminal signal peptides prediction methods. *BMC Bioinformatics*. https://doi.org/10.1186/1471-2105-10-S15-S2

CHU, M. -L, PAN, T. -C, CONWAY, D., SAITTA, B., STOKES, D., KUO, H. -J, GLANVILLE, R. W., TIMPL, R., MANN, K., & DEUTZMANN, R. (1990). The Structure of Type VI Collagen. *Annals of the New York Academy of Sciences*, *580*(1), 55–63. https://doi.org/10.1111/j.1749-6632.1990.tb17917.x

Clark, A. G., Rohrbaugh, A. L., Otterness, I., & Kraus, V. B. (2002). The effects of ascorbic acid on cartilage metabolism in guinea pig articular cartilage explants. *Matrix Biology*. https://doi.org/10.1016/S0945-053X(01)00193-7

Costes, S. V., Daelemans, D., Cho, E. H., Dobbin, Z., Pavlakis, G., & Lockett, S. (2004). Automatic and quantitative measurement of protein-protein colocalization in live cells. *Biophysical Journal*, *86*(6), 3993–4003. https://doi.org/10.1529/biophysj.103.038422

Croce, A. C., & Bottiroli, G. (2014). Autofluorescence spectroscopy and imaging: A tool for biomedical research and diagnosis. *European Journal of Histochemistry*, *58*(4), 320–337. https://doi.org/10.4081/ejh.2014.2461

De Clerck, Y. A., & Jones, P. A. (1980). The Effect of Ascorbic Acid on the Nature and Production of Collagen and Elastin by Rat Smooth-Muscle Cells. In *Biochem. J* (Vol. 186).

De Oliveira, P. T., Zalzal, S. F., Irie, K., & Nanci, A. (2003). Early expression of bone matrix proteins in osteogenic cell cultures. *Journal of Histochemistry and Cytochemistry*, *51*(5), 633–641. https://doi.org/10.1177/002215540305100509

Deshmukh, S. N., Dive, A. M., Moharil, R., & Munde, P. (2016). Enigmatic insight into collagen. In *Journal of Oral and Maxillofacial Pathology*. https://doi.org/10.4103/0973-029X.185932

Di Campli, A., Valderrama, F., Babià, T., De Matteis, M. A., Luini, A., & Egea, G. (1999). Morphological changes in the Golgi complex correlate with actin cytoskeleton rearrangements. *Cell Motility and the Cytoskeleton*, *43*(4), 334–348. https://doi.org/10.1002/(SICI)1097-0169(1999)43:4<334::AID-CM6>3.0.CO;2-3

Di Martino, R., Sticco, L., Luini, A., Di Martino, R., & Luini, A. (n.d.). *Regulation of cargo export and sorting at the trans-Golgi network*. https://doi.org/10.1002/1873-3468.13572

Diomede, F., Marconi, G. D., Serroni, M., Pizzicannella, G., Trubiani, O., & Pizzicannella, J. (2019). Ascorbic acid enhances bone parameter expression in human gingival mesenchymal stem cells. *Journal of Biological Regulators and Homeostatic Agents*. https://doi.org/10.23812/19-312-A

Doan, N. D., DiChiara, A. S., Del Rosario, A. M., Schiavoni, R. P., & Shoulders, M. D. (2019). Mass spectrometry-based proteomics to define intracellular collagen interactomes. In *Methods in Molecular Biology* (Vol. 1944, pp. 95–114). Humana Press Inc. https://doi.org/10.1007/978-1-4939-9095-5_7

Dunn, K. W., Kamocka, M. M., & McDonald, J. H. (2011). A practical guide to evaluating colocalization in biological microscopy. *American Journal of Physiology - Cell Physiology*, *300*(4), 723–742. https://doi.org/10.1152/ajpcell.00462.2010

Egea, G., Serra-Peinado, C., Salcedo-Sicilia, L., & Gutiérrez-Martínez, E. (2013). Actin acting at the

golgi. *Histochemistry and Cell Biology*, *140*(3), 347–360. https://doi.org/10.1007/s00418-013-1115-8

Ellison, A. J., Tanrikulu, I. C., Dones, J. M., & Raines, R. T. (2020). Cyclic Peptide Mimetic of Damaged Collagen. *Biomacromolecules*, *21*(4), 1539–1547. https://doi.org/10.1021/acs.biomac.0c00103

Eyre, D. R., & Glimcher, M. J. (1973). Evidence for intramolecular crosslinks in chicken bone collagen: The isolation of peptides containing allysine aldol. *BBA - Protein Structure*. https://doi.org/10.1016/0005-2795(73)90097-4

Fernandes, R. J., Harkey, M. A., Weis, M., Askew, J. W., & Eyre, D. R. (2007). The post-translational phenotype of collagen synthesized by SAOS-2 osteosarcoma cells. *Bone*, *40*(5), 1343–1351. https://doi.org/10.1016/j.bone.2007.01.011

Fitzgerald, J., Holden, P., & Hansen, U. (2013). The expanded collagen VI family: New chains and new questions. In *Connective Tissue Research* (Vol. 54, Issue 6, pp. 345–350). NIH Public Access. https://doi.org/10.3109/03008207.2013.822865

Fourriere, L., Kasri, A., Gareil, N., Bardin, S., Bousquet, H., Pereira, D., Perez, F., Goud, B., Boncompain, G., & Miserey-Lenkei, S. (2019). RAB6 and microtubules restrict protein secretion to focal adhesions. *Journal of Cell Biology*, *218*(7), 2215–2231. https://doi.org/10.1083/jcb.201805002

Frank, S., Boudko, S., Mizuno, K., Schulthess, T., Engel, J., & Bächinger, H. P. (2003). Collagen triple helix formation can be nucleated at either end. *Journal of Biological Chemistry*. https://doi.org/10.1074/jbc.C200698200

Gasteiger, E., Gattiker, A., Hoogland, C., Ivanyi, I., Appel, R. D., & Bairoch, A. (2003). ExPASy: The proteomics server for in-depth protein knowledge and analysis. *Nucleic Acids Research*. https://doi.org/10.1093/nar/gkg563

Gay, S., Martint, G. R., Muller, P. K., Timpl, R., & Kuhn, K. (1976). Simultaneous synthesis of types I and III collagen by fibroblasts in culture (ascorbic acid/connective tissue/heritable diseases). In *Cell Biology* (Vol. 73, Issue 11).

Gelse, K., Pöschl, E., & Aigner, T. (2003). Collagens - Structure, function, and biosynthesis. *Advanced Drug Delivery Reviews*. https://doi.org/10.1016/j.addr.2003.08.002

Goldberga, I., Li, R., & Duer, M. J. (2018). Collagen Structure-Function Relationships from Solid-State NMR Spectroscopy. *Accounts of Chemical Research*. https://doi.org/10.1021/acs.accounts.8b00092

Good, R. B., Eley, J. D., Gower, E., Butt, G., Blanchard, A. D., Fisher, A. J., & Nanthakumar, C. B. (2019). A high content, phenotypic 'scar-in-a-jar' assay for rapid quantification of collagen fibrillogenesis using disease-derived pulmonary fibroblasts. *BMC Biomedical Engineering*. https://doi.org/10.1186/s42490-019-0014-z

Gordon, M. K., & Hahn, R. A. (2010). Collagens. In *Cell and Tissue Research*. https://doi.org/10.1007/s00441-009-0844-4

Griffiths, G., & Simons, K. (1986). The trans Golgi network: Sorting at the exit site of the Golgi complex. *Science*. https://doi.org/10.1126/science.2945253

Groulx, J. F., Gagné, D., Benoit, Y. D., Martel, D., Basora, N., & Beaulieu, J. F. (2011). Collagen VI is a basement membrane component that regulates epithelial cell-fibronectin interactions. *Matrix Biology*, *30*(3), 195–206. https://doi.org/10.1016/j.matbio.2011.03.002

Guo, M., Chandris, P., Giannini, J. P., Trexler, A. J., Fischer, R., Chen, J., Vishwasrao, H. D., Rey-

Suarez, I., Wu, Y., Wu, X., Waterman, C. M., Patterson, G. H., Upadhyaya, A., Taraska, J. W., & Shroff, H. (2018). Single-shot super-resolution total internal reflection fluorescence microscopy. *Nature Methods*. https://doi.org/10.1038/s41592-018-0004-4

Hanein, D., & Volkmann, N. (2011). Correlative lightelectron microscopy. In *Advances in Protein Chemistry and Structural Biology* (Vol. 82, pp. 91–99). Academic Press Inc. https://doi.org/10.1016/B978-0-12-386507-6.00004-X

Hartmann, A., Boukamp, P., & Friedl, P. (2006). Confocal reflection imaging of 3D fibrin polymers. *Blood Cells, Molecules, and Diseases*, *36*(2), 191–193. https://doi.org/10.1016/j.bcmd.2005.12.033

He, S., Xue, W., Duan, Z., Sun, Q., Li, X., Gan, H., Huang, J., & Qu, J. Y. (2017). Multimodal nonlinear optical microscopy reveals critical role of kinesin-1 in cartilage development. *Biomedical Optics Express*, *8*(3), 1771. https://doi.org/10.1364/boe.8.001771

Heggeness, M. H., Ash, J. F., & Singert, S. J. (1978). *IN T R A C EL LU L A R ACT1 N -C 0 N T A IN I N G FI LA M EN TS I N Cl J L T U R E D H U M A N FIBROBLASTS * Heggeness er al .: Transmembrane Linkage of LETS. 0*, 414–417.

Hellen, C. U. T. (2018). Translation termination and ribosome recycling in eukaryotes. *Cold Spring Harbor Perspectives in Biology*, *10*(10). https://doi.org/10.1101/cshperspect.a032656

Hijazi, K. M., Singfield, K. L., & Veres, S. P. (2019). Ultrastructural response of tendon to excessive level or duration of tensile load supports that collagen fibrils are mechanically continuous. *Journal of the Mechanical Behavior of Biomedical Materials*. https://doi.org/10.1016/j.jmbbm.2019.05.002

Hirschberg, K., Miller, C. M., Ellenberg, J., Presley, J. F., Siggia, E. D., Phair, R. D., & Lippincott-Schwartz, J. (1998). Kinetic analysis of secretory protein traffic and characterization of Golgi to plasma membrane transport intermediates in living cells. *Journal of Cell Biology*, *143*(6), 1485–1503. https://doi.org/10.1083/jcb.143.6.1485

Hostettler, L., Grundy, L., Käser-Pébernard, S., Wicky, C., Schafer, W. R., & Glauser, D. A. (2017). The bright fluorescent protein mNeonGreen facilitates protein expression analysis in vivo. *G3: Genes, Genomes, Genetics*, *7*(2), 607–615. https://doi.org/10.1534/g3.116.038133

Humphries, S. M., Lu, Y., Canty, E. G., & Kadler, K. E. (2008). Active negative control of collagen fibrillogenesis in vivo: Intracellular cleavage of the type I procollagen propeptides in tendon fibroblasts without intracellular fibrils. *Journal of Biological Chemistry*, *283*(18), 12129–12135. https://doi.org/10.1074/jbc.M708198200

Iannarone, V. J., Cruz, G. E., Hilliard, B. A., & Barbe, M. F. (2019). The answer depends on the question: Optimal conditions for western blot characterization of muscle collagen type 1 depends on desired isoform. *Journal of Biological Methods*, *6*(3), 117. https://doi.org/10.14440/jbm.2019.289

Ishida, Y., Kubota, H., Yamamoto, A., Kitamura, A., Bächinger, H. P., & Nagata, K. (2006). Type I collagen in Hsp47-null cells is aggregated in endoplasmic reticulum and deficient in N-propeptide processing and fibrillogenesis. *Molecular Biology of the Cell*. https://doi.org/10.1091/mbc.E05-11-1065

Iwaisako, K., Jiang, C., Zhang, M., Cong, M., Moore-Morris, T. J., Park, T. J., Liu, X., Xu, J., Wang, P., Paik, Y. H., Meng, F., Asagiri, M., Murray, L. A., Hofmann, A. F., Iida, T., Glass, C. K., Brenner, D. A., & Kisseleva, T. (2014). Origin of myofibroblasts in the fibrotic liver in mice. *Proceedings of the National Academy of Sciences of the United States of America*, *111*(32), E3297. https://doi.org/10.1073/pnas.1400062111

Jawerth, L. M., Münster, S., Vader, D. A., Fabry, B., & Weitz, D. A. (2010). A blind spot in confocal

reflection microscopy: The dependence of fiber brightness on fiber orientation in imaging biopolymer networks. *Biophysical Journal*, *98*(3), L1–L3. https://doi.org/10.1016/j.bpj.2009.09.065

Jin, L., Pahuja, K. B., Wickliffe, K. E., Gorur, A., Baumgärtel, C., Schekman, R., & Rape, M. (2012). Ubiquitin-dependent regulation of COPII coat size and function. *Nature*. https://doi.org/10.1038/nature10822

Jiravanichanun, N., Nishino, N., & Okuyama, K. (2006). Conformation of alloHyp in the Y position in the host-guest peptide with the Pro-Pro-Gly sequence: Implication of the destabilization of (Pro-alloHyp-Gly)10. *Biopolymers*. https://doi.org/10.1002/bip.20405

Kalaidzidis, Y. (2009). Multiple objects tracking in fluorescence microscopy. *Journal of Mathematical Biology*, *58*(1–2), 57–80. https://doi.org/10.1007/s00285-008-0180-4

Kalson, N. S., Starborg, T., Lu, Y., Mironov, A., Humphries, S. M., Holmes, D. F., & Kadler, K. E. (2013). Nonmuscle myosin II powered transport of newly formed collagen fibrils at the plasma membrane. *Proceedings of the National Academy of Sciences of the United States of America*. https://doi.org/10.1073/pnas.1314348110

Kamata, H., Tsukasaki, Y., Sakai, T., Ikebe, R., Wang, J., Jeffers, A., Boren, J., Owens, S., Suzuki, T., Higashihara, M., Idell, S., Tucker, T. A., & Ikebe, M. (2017). KIF5A transports collagen vesicles of myofibroblasts during pleural fibrosis. *Scientific Reports*, *7*(1), 1–12. https://doi.org/10.1038/s41598-017-04437-7

Kapacee, Z., Richardson, S. H., Lu, Y., Starborg, T., Holmes, D. F., Baar, K., & Kadler, K. E. (2008). Tension is required for fibripositor formation. *Matrix Biology*, *27*(4), 371–375. https://doi.org/10.1016/j.matbio.2007.11.006

Karamyshev, A. L., Tikhonova, E. B., & Karamysheva, Z. N. (2020). Translational control of secretory proteins in health and disease. *International Journal of Molecular Sciences*, *21*(7). https://doi.org/10.3390/ijms21072538

Karsdal, M. A., Nielsen, S. H., Leeming, D. J., Langholm, L. L., Nielsen, M. J., Manon-Jensen, T., Siebuhr, A., Gudmann, N. S., Rønnow, S., Sand, J. M., Daniels, S. J., Mortensen, J. H., & Schuppan, D. (2017). The good and the bad collagens of fibrosis – Their role in signaling and organ function. In *Advanced Drug Delivery Reviews* (Vol. 121, pp. 43–56). Elsevier B.V. https://doi.org/10.1016/j.addr.2017.07.014

Kazami, S., Usui, T., & Osada, H. (2011). Actin stress fiber retraction and aggresome formation is a common cellular response to actin toxins. *Bioscience, Biotechnology and Biochemistry*, *75*(9), 1853–1855. https://doi.org/10.1271/bbb.110334

Keene, D. R., Engvall, E., & Glanville, R. W. (1988). Ultrastructu4re of type VI collagen in human skin and cartilage suggests an anchoring function for this filamentous network. *Journal of Cell Biology*, *107*(5), 1995–2006. https://doi.org/10.1083/jcb.107.5.1995

Keller, P. J., Schmidt, A. D., Wittbrodt, J., & Stelzer, E. H. K. (2008). Reconstruction of zebrafish early embryonic development by scanned light sheet microscopy. *Science*, *322*(5904), 1065–1069. https://doi.org/10.1126/science.1162493

Kelley, L. A., Mezulis, S., Yates, C. M., Wass, M. N., & Sternberg, M. J. E. (2015). The Phyre2 web portal for protein modeling, prediction and analysis. *Nature Protocols*. https://doi.org/10.1038/nprot.2015.053

Kelly, R. B. (1985). Pathways of protein secretion in eukaryotes. *Science*. https://doi.org/10.1126/science.2994224

Khmaladze, I., Österlund, C., Smiljanic, S., Hrapovic, N., Lafon-Kolb, V., Amini, N., Xi, L., & Fabre, S. (2020). A novel multifunctional skin care formulation with a unique blend of antipollution, brightening and antiaging active complexes. *Journal of Cosmetic Dermatology*, *19*(6), 1415–1425. https://doi.org/10.1111/jocd.13176

Kim, J. J., Lipatova, Z., Majumdar, U., & Segev, N. (2016). Regulation of Golgi Cisternal Progression by Ypt/Rab GTPases. *Developmental Cell*. https://doi.org/10.1016/j.devcel.2016.01.016

Kim, S. D., Pahuja, K. B., Ravazzola, M., Yoon, J., Boyadjiev, S. A., Hammamoto, S., Schekman, R., Orci, L., & Kim, J. (2012). SEC23-SEC31 the interface plays critical role for export of procollagen from the endoplasmic reticulum. *Journal of Biological Chemistry*. https://doi.org/10.1074/jbc.M111.283382

Kirchhausen, T., Owen, D., & Harrison, S. C. (2014). *of Clathrin-Mediated Membrane Traffic*.

Kishino, A., Hayashi, K., Hidai, C., Masuda, T., Nomura, Y., & Oshima, T. (2017). XBP1-FoxO1 interaction regulates ER stress-induced autophagy in auditory cells. *Scientific Reports*, *7*(1). https://doi.org/10.1038/s41598-017-02960-1

Koike, T., & Yamada, H. (2019). Methods for array tomography with correlative light and electron microscopy. In *Medical Molecular Morphology* (Vol. 52, Issue 1, pp. 8–14). Springer Tokyo. https://doi.org/10.1007/s00795-018-0194-y

Koivu, J., Myllylä, R., Helaakoski, T., Pihlajaniemi, T., Tasanen, K., & Kivirikko, K. I. (1987). A single polypeptide acts both as the beta subunit of prolyl 4-hydroxylase and as a protein disulfide-isomerase. *Journal of Biological Chemistry*.

Komatsu, N., Kajiya, M., Motoike, S., Takewaki, M., Horikoshi, S., Iwata, T., Ouhara, K., Takeda, K., Matsuda, S., Fujita, T., & Kurihara, H. (2018). Type i collagen deposition via osteoinduction ameliorates YAP/TAZ activity in 3D floating culture clumps of mesenchymal stem cell/extracellular matrix complexes. *Stem Cell Research and Therapy*. https://doi.org/10.1186/s13287-018-1085-9

Krahn, K. N., Bouten, C. V. C., Van Tuijl, S., Van Zandvoort, M. A. M. J., & Merkx, M. (2006). Fluorescently labeled collagen binding proteins allow specific visualization of collagen in tissues and live cell culture. *Analytical Biochemistry*, *350*(2), 177–185. https://doi.org/10.1016/j.ab.2006.01.013

Kudalkar, E. M., Davis, T. N., & Asbury, C. L. (2016). Single-molecule total internal reflection fluorescence microscopy. *Cold Spring Harbor Protocols*. https://doi.org/10.1101/pdb.top077800

Kuivaniemi, H., & Tromp, G. (2019). Type III collagen (COL3A1): Gene and protein structure, tissue distribution, and associated diseases. In *Gene* (Vol. 707, pp. 151–171). Elsevier B.V. https://doi.org/10.1016/j.gene.2019.05.003

Kumar, P., Nagarajan, A., & Uchil, P. D. (2019). DNA transfection mediated by cationic lipid reagents. *Cold Spring Harbor Protocols*, *2019*(3), 215–223. https://doi.org/10.1101/pdb.prot095414

Lalande, M., Comby-Zerbino, C., Bouakil, M., Dugourd, P., Chirot, F., & Poully, J. C. (2018). Isolated Collagen Mimetic Peptide Assemblies Have Stable Triple-Helix Structures. *Chemistry - A European Journal*, *24*(52), 13728–13733. https://doi.org/10.1002/chem.201802929

Lau, Y. H., Giessen, T. W., Altenburg, W. J., & Silver, P. A. (2018). Prokaryotic nanocompartments form synthetic organelles in a eukaryote. *Nature Communications*, *9*(1). https://doi.org/10.1038/s41467-018-03768-x

Lavieu, G., Dunlop, M. H., Lerich, A., Zheng, H., Bottanelli, F., & Rothman, J. E. (2014). The Golgi

ribbon structure facilitates anterograde transport of large cargoes. *Molecular Biology of the Cell*. https://doi.org/10.1091/mbc.E14-04-0931

Lázaro-Diéguez, F., Jiménez, N., Barth, H., Koster, A. J., Renau-Piqueras, J., Llopis, J. L., Burger, K. N. J., & Egea, G. (2006). Actin filaments are involved in the maintenance of Golgi cisternae morphology and intra-Golgi pH. *Cell Motility and the Cytoskeleton*, *63*(12), 778–791. https://doi.org/10.1002/cm.20161

Le Goff, C., Somerville, R. P. T., Kesteloot, F., Powell, K., Birk, D. E., Colige, A. C., & Apte, S. S. (2006). Regulation of procollagen amino-propeptide processing during mouse embryogenesis by specialization of homologous ADAMTS proteases: Insights on collagen biosynthesis and dermatosparaxis. *Development*. https://doi.org/10.1242/dev.02308

Leavitt, T., Hu, M. S., Marshall, C. D., Barnes, L. A., Lorenz, H. P., & Longaker, M. T. (2016). Scarless wound healing: finding the right cells and signals. In *Cell and Tissue Research* (Vol. 365, Issue 3, pp. 483–493). Springer Verlag. https://doi.org/10.1007/s00441-016-2424-8

Lee, M., Chea, K., Pyda, R., Chua, M., & Dominguez, I. (2017). Comparative analysis of non-viral transfection methods in mouse embryonic fibroblast cells. *Journal of Biomolecular Techniques*, *28*(2), 67–74. https://doi.org/10.7171/jbt.17-2802-003

Lee Sweeney, H., & Holzbaur, E. L. F. (2018). Motor proteins. *Cold Spring Harbor Perspectives in Biology*, *10*(5), 1–17. https://doi.org/10.1101/cshperspect.a021931

Lee, Y., Phelps, C., Huang, T., Mostofian, B., Wu, L., Zhang, Y., Tao, K., Chang, Y. H., Stork, P. J. S., Gray, J. W., Zuckerman, D. M., & Nan, X. (2019). High-throughput single-particle tracking reveals 1 nested membrane domains that dictate krasg12d 2 diffusion and trafficking. *ELife*, *8*. https://doi.org/10.7554/eLife.46393

Lees, J. F., Tasab, M., & Bulleid, N. J. (1997). Identification of the molecular recognition sequence which determines the type-specific assembly of procollagen. *EMBO Journal*, *16*(5), 908–916. https://doi.org/10.1093/emboj/16.5.908

Leung, B. M., Moraes, C., Cavnar, S. P., Luker, K. E., Luker, G. D., & Takayama, S. (2015). Microscale 3D Collagen Cell Culture Assays in Conventional Flat-Bottom 384-Well Plates. *Journal of Laboratory Automation*. https://doi.org/10.1177/2211068214563793

Li, P., Bademosi, A. T., Luo, J., & Meunier, F. A. (2018). Actin Remodeling in Regulated Exocytosis: Toward a Mesoscopic View. In *Trends in Cell Biology*. https://doi.org/10.1016/j.tcb.2018.04.004

Liebmann, J. E., Cook, J. A., Lipschultz, C., Teague, D., Fisher, J., & Mitchell, J. B. (1993). Cytotoxic studies of pacfitaxel (Taxol®) in human tumour cell lines. *British Journal of Cancer*, *68*(6), 1104–1109. https://doi.org/10.1038/bjc.1993.488

Lim Goh, K., Holmes, D. F., Lu, Y. H., Kadler, K. E., & Purslow, P. P. (2018). Data Descriptor: Age-related dataset on the mechanical properties and collagen fibril structure of tendons from a murine model. *Nature Publishing Group*. https://doi.org/10.1038/sdata.2018.140

Lin, A. H., Zitnay, J. L., Li, Y., Yu, S. M., & Weiss, J. A. (2019). Microplate assay for denatured collagen using collagen hybridizing peptides. *Journal of Orthopaedic Research*, *37*(2), 431–438. https://doi.org/10.1002/jor.24185

LINDEN, I. H., LADEN, E., ERICKSON, J. O., & ARMEN, D. (1955). Electron microscopic study of normal skin collagen and elastic fibers. *The Journal of Investigative Dermatology*, *24*(2), 83–88. https://doi.org/10.1038/jid.1955.13

Lippincott-Schwartz, J., Snapp, E. L., & Phair, R. D. (2018). The Development and Enhancement of FRAP as a Key Tool for Investigating Protein Dynamics. In *Biophysical Journal*. https://doi.org/10.1016/j.bpj.2018.08.007

Long, C. G., Apigo, J., Brodsky, B., Braswell, E., Zhu, D., & Baum, J. (1993). Characterization of Collagen-like Peptides Containing Interruptions in the Repeating Gly-X-Y Sequence. *Biochemistry*. https://doi.org/10.1021/bi00094a027

Louvard, D. (1980). Apical membrane aminopeptidase appears at site of cell-cell contact in cultured kidney epithelial cells. *Proceedings of the National Academy of Sciences of the United States of America*, *77*(7 II), 4132–4136. https://doi.org/10.1073/pnas.77.7.4132

Lu, Y., Kamel-El Sayed, S. A., Wang, K., Tiede-Lewis, L. A. M., Grillo, M. A., Veno, P. A., Dusevich, V., Phillips, C. L., Bonewald, L. F., & Dallas, S. L. (2018). Live Imaging of Type I Collagen Assembly Dynamics in Osteoblasts Stably Expressing GFP and mCherry-Tagged Collagen Constructs. *Journal of Bone and Mineral Research*. https://doi.org/10.1002/jbmr.3409

Lucero, H. A., & Kagan, H. M. (2006). Lysyl oxidase: An oxidative enzyme and effector of cell function. In *Cellular and Molecular Life Sciences*. https://doi.org/10.1007/s00018-006-6149-9

Luo, J., & Tong, Y. W. (2011). Self-assembly of collagen-mimetic peptide amphiphiles into biofunctional nanofiber. *ACS Nano*. https://doi.org/10.1021/nn202822f

Luo, L. M., Huang, Y., Zhao, B. X., Zhao, X., Duan, Y., Du, R., Yu, K. F., Song, P., Zhao, Y., Zhang, X., & Zhang, Q. (2013). Anti-tumor and anti-angiogenic effect of metronomic cyclic NGR-modified liposomes containing paclitaxel. *Biomaterials*, *34*(4), 1102–1114. https://doi.org/10.1016/j.biomaterials.2012.10.029

Lutz, V., Sattler, M., Gallinat, S., Wenck, H., Poertner, R., & Fischer, F. (2012). Impact of collagen crosslinking on the second harmonic generation signal and the fluorescence lifetime of collagen autofluorescence. *Skin Research and Technology*, *18*(2), 168–179. https://doi.org/10.1111/j.1600-0846.2011.00549.x

Ma, X., Wang, F., & Wang, B. (2020). Application of an in vitro reconstructed human skin on cosmetics in skin irritation tests. *Journal of Cosmetic Dermatology*. https://doi.org/10.1111/jocd.13789

Maaß, T., Bayley, C. P., Mörgelin, M., Lettmann, S., Bonaldo, P., Paulsson, M., Baldock, C., & Wagener, R. (2016). Heterogeneity of collagen VI microfibrils: Structural analysis of non-collagenousregions. *Journal of Biological Chemistry*, *291*(10), 5247–5258. https://doi.org/10.1074/jbc.M115.705160

Malhotra, V., & Erlmann, P. (2015). The Pathway of Collagen Secretion. *Annual Review of Cell and Developmental Biology*. https://doi.org/10.1146/annurev-cellbio-100913-013002

Manley, S., Gillette, J. M., & Lippincott-Schwartz, J. (2010). Single-Particle Tracking Photoactivated Localization Microscopy for Mapping Single-Molecule Dynamics. In *Methods in Enzymology* (Vol. 475, Issue C, pp. 109–120). Academic Press Inc. https://doi.org/10.1016/S0076-6879(10)75005-9

Mansfield, J. C., Mandalia, V., Toms, A., Peter Winlove, C., & Brasselet, S. (2019). Collagen reorganization in cartilage under strain probed by polarization sensitive second harmonic generation microscopy. *Journal of the Royal Society Interface*, *16*(150). https://doi.org/10.1098/rsif.2018.0611

Maqsood, M. I., Matin, M. M., Bahrami, A. R., & Ghasroldasht, M. M. (2013). Immortality of cell lines: Challenges and advantages of establishment. In *Cell Biology International* (Vol. 37, Issue 10, pp. 1038–1045). Blackwell Publishing Ltd. https://doi.org/10.1002/cbin.10137

Mattheyses, A. L., Simon, S. M., & Rappoport, J. Z. (2010). Imaging with total internal reflection

fluorescence microscopy for the cell biologist. In *Journal of Cell Science*. https://doi.org/10.1242/jcs.056218

Mayorca-Guiliani, A. E., Willacy, O., Madsen, C. D., Rafaeva, M., Elisabeth Heumüller, S., Bock, F., Sengle, G., Koch, M., Imhof, T., Zaucke, F., Wagener, R., Sasaki, T., Erler, J. T., & Reuten, R. (2019). Decellularization and antibody staining of mouse tissues to map native extracellular matrix structures in 3D. *Nature Protocols*, *14*(12), 3395–3425. https://doi.org/10.1038/s41596-019-0225-8

Mazo, G. (2020). QuickFigures: A tool to quickly transform microscope images into quality figures. In *bioRxiv* (p. 2020.09.24.311282). bioRxiv. https://doi.org/10.1101/2020.09.24.311282

McCaughey, J., Stevenson, N. L., Cross, S., & Stephens, D. J. (2019). ER-to-Golgi trafficking of procollagen in the absence of large carriers. *Journal of Cell Biology*. https://doi.org/10.1083/jcb.201806035

McGourty, C. A., Akopian, D., Walsh, C., Gorur, A., Werner, A., Schekman, R., Bautista, D., & Rape, M. (2016). Regulation of the CUL3 Ubiquitin Ligase by a Calcium-Dependent Co-adaptor. *Cell*. https://doi.org/10.1016/j.cell.2016.09.026

McKee, T. J., Perlman, G., Morris, M., & Komarova, S. V. (2019). Extracellular matrix composition of connective tissues: a systematic review and meta-analysis. *Scientific Reports*. https://doi.org/10.1038/s41598-019-46896-0

Meinert, T., & Rohrbach, A. (2019). Light-sheet microscopy with length-adaptive Bessel beams. *Biomedical Optics Express*, *10*(2), 670. https://doi.org/10.1364/boe.10.000670

Midorikawa, M. (2018). Real-time imaging of synaptic vesicle exocytosis by total internal reflection fluorescence (TIRF) microscopy. In *Neuroscience Research*. https://doi.org/10.1016/j.neures.2018.01.008

Miklavc, P., & Frick, M. (2020). Actin and Myosin in Non-Neuronal Exocytosis. *Cells*, *9*(6), 1–18. https://doi.org/10.3390/cells9061455

Miller, E., & Grosel, J. M. (2020). A review of Ehlers-Danlos syndrome. In *Journal of the American Academy of Physician Assistants* (Vol. 33, Issue 4, pp. 23–28). Lippincott Williams and Wilkins. https://doi.org/10.1097/01.JAA.0000657160.48246.91

Mironov, A., Beznoussenko, G. V., Trucco, A., Lupetti, P., Smith, J. D., Geerts, W. J. C., Koster, A. J., Burger, K. N. J., Martone, M. E., Deerinck, T. J., Ellisman, M. H., & Luini, A. (2003). ER-to-Golgi carriers arise through direct en bloc protrusion and multistage maturation of specialized ER exit domains. *Developmental Cell*. https://doi.org/10.1016/S1534-5807(03)00294-6

Miserey-Lenkei, S., Bousquet, H., Pylypenko, O., Bardin, S., Dimitrov, A., Bressanelli, G., Bonifay, R., Fraisier, V., Guillou, C., Bougeret, C., Houdusse, A., Echard, A., & Goud, B. (2017). Coupling fission and exit of RAB6 vesicles at Golgi hotspots through kinesin-myosin interactions. *Nature Communications*, *8*(1). https://doi.org/10.1038/s41467-017-01266-0

Moen, E., Bannon, D., Kudo, T., Graf, W., Covert, M., & Van Valen, D. (2019). Deep learning for cellular image analysis. In *Nature Methods* (Vol. 16, Issue 12, pp. 1233–1246). Nature Research. https://doi.org/10.1038/s41592-019-0403-1

Morris, J. L., Cross, S. J., Lu, Y., Kadler, K. E., Lu, Y., Dallas, S. L., & Martin, P. (2018). Live imaging of collagen deposition during skin development and repair in a collagen I – GFP fusion transgenic zebrafish line. *Developmental Biology*. https://doi.org/10.1016/j.ydbio.2018.06.001

Mostaço-Guidolin, L., Rosin, N. L., & Hackett, T. L. (2017). Imaging collagen in scar tissue:

Developments in second harmonic generation microscopy for biomedical applications. *International Journal of Molecular Sciences*, *18*(8). https://doi.org/10.3390/ijms18081772

Murad, S., Grove, D., Lindberg, K. A., Reynolds, G., Sivarajah, A., & Pinnell, S. R. (1981). Regulation of collagen synthesis by ascorbic acid. *Proceedings of the National Academy of Sciences of the United States of America*. https://doi.org/10.1073/pnas.78.5.2879

Myllyharju, J., & Kivirikko, K. I. (2001). Collagens and collagen-related diseases. In *Annals of Medicine* (Vol. 33, Issue 1, pp. 7–21). Royal Society of Medicine Press Ltd. https://doi.org/10.3109/07853890109002055

Narice, B. F., Green, N. H., MacNeil, S., & Anumba, D. (2016). Second Harmonic Generation microscopy reveals collagen fibres are more organised in the cervix of postmenopausal women. *Reproductive Biology and Endocrinology*, *14*(1), 1–8. https://doi.org/10.1186/s12958-016-0204-7

Nian, L., Hu, Y., Fu, C., Song, C., Wang, J., & Xiao, J. (2018). Fluorescence self-quenching assay for the detection of target collagen sequences using a short probe peptide. *Talanta*, *176*(May 2017), 492–498. https://doi.org/10.1016/j.talanta.2017.08.042

Nimni, M. E. (1983). Collagen: Structure, function, and metabolism in normal and fibrotic tissues. In *Seminars in Arthritis and Rheumatism*. https://doi.org/10.1016/0049-0172(83)90024-0

Nishimura, Y., Bereczky, B., Yoshioka, K., Taniguchi, S., & Itoh, K. (2011). A novel role of Rho-kinase in the regulation of ligand-induced phosphorylated EGFR endocytosis via the early/late endocytic pathway in human fibrosarcoma cells. *Journal of Molecular Histology*, *42*(5), 427–442. https://doi.org/10.1007/s10735-011-9348-0

Nishio, T., Hu, R., Koyama, Y., Liang, S., Rosenthal, S. B., Yamamoto, G., Karin, D., Baglieri, J., Ma, H. Y., Xu, J., Liu, X., Dhar, D., Iwaisako, K., Taura, K., Brenner, D. A., & Kisseleva, T. (2019). Activated hepatic stellate cells and portal fibroblasts contribute to cholestatic liver fibrosis in MDR2 knockout mice. *Journal of Hepatology*, *71*(3), 573–585. https://doi.org/10.1016/j.jhep.2019.04.012

Okoro, C., Kelkar, V., Sivaguru, M., Emmadi, R., & Toussaint, K. C. (2018). Second-harmonic patterned polarization-analyzed reflection confocal microscopy of stromal collagen in benign and malignant breast tissues. *Scientific Reports*, *8*(1), 1–8. https://doi.org/10.1038/s41598-018-34693-0

Omari, S., Makareeva, E., Roberts-Pilgrim, A., Mirigian, L., Jarnik, M., Ott, C., Lippincott-Schwartz, J., & Leikin, S. (2018). Noncanonical autophagy at ER exit sites regulates procollagen turnover. *Proceedings of the National Academy of Sciences*. https://doi.org/10.1073/pnas.1814552115

Orgel, J. P. R. O., & Madhurapantula, R. S. (2019). A structural prospective for collagen receptors such as DDR and their binding of the collagen fibril. In *Biochimica et Biophysica Acta - Molecular Cell Research* (Vol. 1866, Issue 11). Elsevier B.V. https://doi.org/10.1016/j.bbamcr.2019.04.008

Pajak, B., Siwiak, E., Sołtyka, M., Priebe, A., Zieliński, R., Fokt, I., Ziemniak, M., Jaśkiewicz, A., Borowski, R., Domoradzki, T., & Priebe, W. (2020). 2-Deoxy-D-Glucose and its analogs: From diagnostic to therapeutic agents. In *International Journal of Molecular Sciences*. https://doi.org/10.3390/ijms21010234

Panwar, P., Butler, G. S., Jamroz, A., Azizi, P., Overall, C. M., & Brömme, D. (2018). Aging-associated modifications of collagen affect its degradation by matrix metalloproteinases. *Matrix Biology*. https://doi.org/10.1016/j.matbio.2017.06.004

Parmar, P. A., Skaalure, S. C., Chow, L. W., St-Pierre, J. P., Stoichevska, V., Peng, Y. Y., Werkmeister, J. A., Ramshaw, J. A. M., & Stevens, M. M. (2016). Temporally degradable collagen-mimetic hydrogels tuned to chondrogenesis of human mesenchymal stem cells. *Biomaterials*.

https://doi.org/10.1016/j.biomaterials.2016.05.011

Parsons, K. K., Maeda, N., Yamauchi, M., Banes, A. J., & Koller, B. H. (2006). Ascorbic acid-independent synthesis of collagen in mice. *American Journal of Physiology-Endocrinology and Metabolism*, *290*(6), E1131–E1139. https://doi.org/10.1152/ajpendo.00339.2005

Pelham, H. R. B. (2001). Traffic through the Golgi apparatus. In *Journal of Cell Biology*. https://doi.org/10.1083/jcb.200110160

Pinnell, S. R. (1985). Regulation of collagen biosynthesis by ascorbic acid: A review. *Yale Journal of Biology and Medicine*.

Polishchuk, R. S., Polishchuk, E. V., Marra, P., Alberti, S., Buccione, R., Luini, A., & Mironov, A. A. (2000). Correlative light-electron microscopy reveals the tubular-saccular ultrastructure of carriers operating between Golgi apparatus and plasma membrane. *Journal of Cell Biology*, *148*(1), 45–58. https://doi.org/10.1083/jcb.148.1.45

Pontes, M. H., Sevostyanova, A., & Groisman, E. A. (2015). When Too Much ATP Is Bad for Protein Synthesis. In *Journal of Molecular Biology* (Vol. 427, Issue 16, pp. 2586–2594). Academic Press. https://doi.org/10.1016/j.jmb.2015.06.021

Presley, J. F., Smith, C., Hirschberg, K., Miller, C., Cole, N. B., Zaal, K. J. M., & Lippincott-Schwartz, J. (1998). Video Essay Golgi Membrane Dynamics 1□ V. In *Molecular Biology of the Cell* (Vol. 9). www.molbiolcell.org.

Qiao, H., Bell, J., Juliao, S., Li, L., & May, J. M. (2008). Ascorbic acid uptake and regulation of type I collagen synthesis in cultured vascular smooth muscle cells. *Journal of Vascular Research*. https://doi.org/10.1159/000135661

Rajpar, M. H., Koch, M. J., Davies, R. M., Mellody, K. T., Kielty, C. M., & Dixon, M. J. (2002). Mutation of the signal peptide region of the bicistronic gene DSPP affects translocation to the endoplasmic reticulum and results in defective dentine biomineralization. *Human Molecular Genetics*, *11*(21), 2559–2565. https://doi.org/10.1093/hmg/11.21.2559

Ramachandran, G. N., & Kartha, G. (1954). Structure of collagen. *Nature*. https://doi.org/10.1038/174269c0

Ramshaw, J. A. M., Shah, N. K., & Brodsky, B. (1998). Gly-X-Y tripeptide frequencies in collagen: A context for host-guest triple-helical peptides. *Journal of Structural Biology*. https://doi.org/10.1006/jsbi.1998.3977

Raote, I., Ortega-Bellido, M., Santos, A. J. M., Foresti, O., Zhang, C., Garcia-Parajo, M. F., Campelo, F., & Malhotra, V. (2018). TANGO1 builds a machine for collagen export by recruiting and spatially organizing COPII, tethers and membranes. *ELife*. https://doi.org/10.7554/eLife.32723

Raspanti, M., Reguzzoni, M., Protasoni, M., & Basso, P. (2018). Not only tendons: The other architecture of collagen fibrils. In *International Journal of Biological Macromolecules*. https://doi.org/10.1016/j.ijbiomac.2017.10.037

Reynolds, H. M., Zhang, L., Tran, D. T., & Hagen, X. K. G. Ten. (2019). *Tango1 creates ER/Golgi docking sites*. *1*(8), 19498–19510. https://doi.org/10.1074/jbc.RA119.011063

Ricard-Blum, S. (2011). The Collagen Family. *Cold Spring Harbor Perspectives in Biology*, *3*(1), 1–19. https://doi.org/10.1101/cshperspect.a004978

Rich, A., & Crick, F. H. C. (1961). The molecular structure of collagen. *Journal of Molecular Biology*.

https://doi.org/10.1016/S0022-2836(61)80016-8

Rodan, S. B., Imai, Y., Thiede, M. A., Wesolowski, G., Thompson, D., Bar-Shavit, Z., Shull, S., Mann, K., & Rodan, G. A. (1987). Characterization of a Human Osteosarcoma Cell Line (Saos-2) with Osteoblastic Properties. *Cancer Research*, *47*(18), 4961–4966.

Rodnina, M. V., & Wintermeyer, W. (2011). The ribosome as a molecular machine: The mechanism of tRNA-mRNA movement in translocation. In *Biochemical Society Transactions* (Vol. 39, Issue 2, pp. 658–662). Portland Press. https://doi.org/10.1042/BST0390658

Rose, J. K. (2003). Optimization of Transfection. *Current Protocols in Cell Biology*. https://doi.org/10.1002/0471143030.cb2007s19

Saito, K., Maeda, M., & Katada, T. (2017). Regulation of the Sar1 GTPase cycle is necessary for large cargo secretion from the endoplasmic reticulum. In *Frontiers in Cell and Developmental Biology*. https://doi.org/10.3389/fcell.2017.00075

Saito, K., Yamashiro, K., Ichikawa, Y., Erlmann, P., Kontani, K., Malhotra, V., & Katada, T. (2011). cTAGE5 mediates collagen secretion through interaction with TANGO1 at endoplasmic reticulum exit sites. *Molecular Biology of the Cell*. https://doi.org/10.1091/mbc.E11-02-0143

Saito, K., Yamashiro, K., Shimazu, N., Tanabe, T., Kontani, K., & Katada, T. (2014). Concentration of Sec12 at ER exit sites via interaction with cTAGE5 is required for collagen export. *Journal of Cell Biology*. https://doi.org/10.1083/jcb.201312062

Sano, M., Nishino, I., Ueno, K., & Kamimori, H. (2004). Assay of collagenase activity for native triple-helical collagen using capillary gel electrophoresis with laser-induced fluorescence detection. *Journal of Chromatography B*, *809*(2), 251–256. https://doi.org/10.1016/j.jchromb.2004.06.036

Sarkar, B., Oleary, L. E. R., & Hartgerink, J. D. (2014). Self-assembly of fiber-forming collagen mimetic peptides controlled by triple-helical nucleation. *Journal of the American Chemical Society*. https://doi.org/10.1021/ja504377s

Sarkar, N., Banerjee, J., Hanson, A. J., Elegbede, A. I., Rosendahl, T., Krueger, A. B., Banerjee, A. L., Tobwala, S., Wang, R., Lu, X., Mallik, S., & Srivastava, D. K. (2008). Matrix metalloproteinase-assisted triggered release of liposomal contents. *Bioconjugate Chemistry*. https://doi.org/10.1021/bc070081p

Schegg, B., Hulsmeier, A. J., Rutschmann, C., Maag, C., & Hennet, T. (2009). Core Glycosylation of Collagen Is Initiated by Two (1-O)Galactosyltransferases. *Molecular and Cellular Biology*. https://doi.org/10.1128/mcb.02085-07

Schlabach, M. R., Hu, J. K., Li, M., & Elledge, S. J. (2010). Synthetic design of strong promoters. *Proceedings of the National Academy of Sciences of the United States of America*. https://doi.org/10.1073/pnas.0914803107

Schneider-poetsch, T., Ju, J., Eyler, D. E., Dang, Y., Bhat, S., Merrick, W. C., Green, R., Shen, B., & Liu, J. O. (2010). *HHS Public Access*. *6*(3), 209–217. https://doi.org/10.1038/nchembio.304.Inhibition

Schneider, C. A., Rasband, W. S., & Eliceiri, K. W. (2012). NIH Image to ImageJ: 25 years of image analysis. In *Nature Methods* (Vol. 9, Issue 7, pp. 671–675). Nature Publishing Group. https://doi.org/10.1038/nmeth.2089

Seluanov, A., Vaidya, A., & Gorbunova, V. (2010). Establishing primary adult fibroblast cultures from rodents. *Journal of Visualized Experiments*, *44*. https://doi.org/10.3791/2033

Shaner, N. C., Lambert, G. G., Chammas, A., Ni, Y., Cranfill, P. J., Baird, M. A., Sell, B. R., Allen, J. R., Day, R. N., Israelsson, M., Davidson, M. W., & Wang, J. (2013). A bright monomeric green fluorescent protein derived from Branchiostoma lanceolatum. *Nature Methods*. https://doi.org/10.1038/nmeth.2413

Short, A. R., Czeisler, C., Stocker, B., Cole, S., Otero, J. J., & Winter, J. O. (2017). Imaging Cell–Matrix Interactions in 3D Collagen Hydrogel Culture Systems. *Macromolecular Bioscience*, *17*(6). https://doi.org/10.1002/mabi.201600478

Shorter, S. A., Pettit, M. W., Dyer, P. D. R., Coakley Youngs, E., Gorringe-Pattrick, M. A. M., El-Daher, S., & Richardson, S. (2017). Green fluorescent protein (GFP): is seeing believing and is that enough? *Journal of Drug Targeting*, *25*(9–10), 809–817. https://doi.org/10.1080/1061186X.2017.1358725

Shoulders, M. D., & Raines, R. T. (2009). Collagen Structure and Stability. *Annual Review of Biochemistry*. https://doi.org/10.1146/annurev.biochem.77.032207.120833

Simon, H. J., Van Agthoven, M. A., Lam, P. Y., Floris, F., Chiron, L., Delsuc, M. A., Rolando, C., Barrow, M. P., & O'Connor, P. B. (2016). Uncoiling collagen: A multidimensional mass spectrometry study. *Analyst*, *141*(1), 157–165. https://doi.org/10.1039/c5an01757b

Soltaninassab, S. R., Sotos, J. P., Bonds, M. D., Williams, L. a, Williams, J. W., Abbott, N. L., Murphy, C. J., & Held, P. G. (2008). A Novel High Throughput-Compatible Cell Migration Screening Assay. *Cell*, 3–6.

Sottile, J., Shi, F., Rublyevska, I., Chiang, H. Y., Lust, J., & Chandler, J. (2007). Fibronectin-dependent collagen I deposition modulates the cell response to fibronectin. *American Journal of Physiology - Cell Physiology*, *293*(6). https://doi.org/10.1152/ajpcell.00130.2007

Stalder, D., & Gershlick, D. C. (2020). Direct trafficking pathways from the Golgi apparatus to the plasma membrane. *Seminars in Cell and Developmental Biology*, *107*(January), 112–125. https://doi.org/10.1016/j.semcdb.2020.04.001

Stephens, D. J., & Pepperkok, R. (2002). Imaging of procollagen transport reveals COPI-dependent cargo sorting during ER-to-Golgi transport in mammalian cells. *Journal of Cell Science*, *115*(6), 1149–1160.

Stockmar, I., Feddersen, H., Cramer, K., Gruber, S., Jung, K., Bramkamp, M., & Shin, J. Y. (2018). Optimization of sample preparation and green color imaging using the mNeonGreen fluorescent protein in bacterial cells for photoactivated localization microscopy. *Scientific Reports*, *8*(1), 1–11. https://doi.org/10.1038/s41598-018-28472-0

Stow, J. L., Fath, K. R., & Burgess, D. R. (1998). Budding roles for myosin II on the Golgi. *Trends in Cell Biology*, *8*(4), 138–141. https://doi.org/10.1016/S0962-8924(98)01238-0

Sun, X., Yao, L., Fu, C., Xiao, J., Luo, L., & Wang, J. (2019). Detection of target collagen peptides with single amino acid mutation using two fluorescent peptide probes. *Journal of Materials Chemistry B*, *7*(48), 7676–7682. https://doi.org/10.1039/c9tb00610a

Tafoya, S., & Bustamante, C. (2018). Molecular switch-like regulation in motor proteins. In *Philosophical Transactions of the Royal Society B: Biological Sciences*. https://doi.org/10.1098/rstb.2017.0181

Takaki, R., Mugnai, M. L., Goldtzvik, Y., & Thirumalai, D. (2019). How kinesin waits for ATP affects the nucleotide and load dependence of the stepping kinetics. *Proceedings of the National Academy of Sciences of the United States of America*. https://doi.org/10.1073/pnas.1913650116

Tanida-Miyake, E., Koike, M., Uchiyama, Y., & Tanida, I. (2018). Optimization of mNeonGreen for Homo sapiens increases its fluorescent intensity in mammalian cells. *PLoS ONE*. https://doi.org/10.1371/journal.pone.0191108

Theocharidis, G., Drymoussi, Z., Kao, A. P., Barber, A. H., Lee, D. A., Braun, K. M., & Connelly, J. T. (2016). Type VI collagen regulates dermal matrix assembly and fibroblast motility. *Journal of Investigative Dermatology*, *136*(1), 74–83. https://doi.org/10.1038/JID.2015.352

Theocharis, A. D., Skandalis, S. S., Gialeli, C., & Karamanos, N. K. (2016). Extracellular matrix structure. In *Advanced Drug Delivery Reviews* (Vol. 97, pp. 4–27). Elsevier B.V. https://doi.org/10.1016/j.addr.2015.11.001

Tillberg, P. W., & Chen, F. (2019). Expansion microscopy: Scalable and convenient super-resolution microscopy. In *Annual Review of Cell and Developmental Biology* (Vol. 35, pp. 683–701). Annual Reviews Inc. https://doi.org/10.1146/annurev-cellbio-100818-125320

Timmins, A., Saint-André, M., & De Visser, S. P. (2017). Understanding How Prolyl-4-hydroxylase Structure Steers a Ferryl Oxidant toward Scission of a Strong C-H Bond. *Journal of the American Chemical Society*. https://doi.org/10.1021/jacs.7b02839

Tinevez, J. Y., Perry, N., Schindelin, J., Hoopes, G. M., Reynolds, G. D., Laplantine, E., Bednarek, S. Y., Shorte, S. L., & Eliceiri, K. W. (2017). TrackMate: An open and extensible platform for single-particle tracking. *Methods*, *115*, 80–90. https://doi.org/10.1016/j.ymeth.2016.09.016

Toomre, D., Keller, P., White, J., Olivo, J. C., & Simons, K. (1999). Dual-color visualization of trans-Golgi network to plasma membrane traffic along microtubules in living cells. *Journal of Cell Science*, *112*(1), 21–33.

Townley, A. K., Feng, Y., Schmidt, K., Carter, D. A., Porter, R., Verkade, P., & Stephens, D. J. (2008). Efficient coupling of Sec23-Sec24 to Sec13-Sec31 drives COPII-dependent collagen secretion and is essential for normal craniofacial development. *Journal of Cell Science*. https://doi.org/10.1242/jcs.031070

Trucco, A., Polischuck, R. S., Martella, O., Di Pentima, A., Fusella, A., Di Giandomenico, D., San Pietro, E., Beznoussenko, G. V., Polischuk, E. V., Baldassarre, M., Buccione, R., Geerts, W. J. C., Koster, A. J., Burger, K. N. J., Mironov, A. A., & Luini, A. (2004). Secretory traffic triggers the formation of tubular continuities across Golgi sub-compartments. *Nature Cell Biology*. https://doi.org/10.1038/ncb1180

Ueno, T., Kaneko, K., Katano, H., Sato, Y., Mazitschek, R., Tanaka, K., Hattori, S., Irie, S., Sata, T., & Ogawa-Goto, K. (2010). Expansion of the trans-Golgi network following activated collagen secretion is supported by a coiled-coil microtubule-bundling protein, p180, on the ER. *Experimental Cell Research*, *316*(3), 329–340. https://doi.org/10.1016/j.yexcr.2009.11.009

Valente, C., Polishchuk, R., & De Matteis, M. A. (2010). Rab6 and myosin II at the cutting edge of membrane fission. *Nature Cell Biology*, *12*(7), 635–638. https://doi.org/10.1038/ncb0710-635

Varani, J., Dame, M. K., Rittie, L., Fligiel, S. E. G., Kang, S., Fisher, G. J., & Voorhees, J. J. (2006). Decreased Collagen Production in Chronologically Aged Skin. *The American Journal of Pathology*, *168*(6), 1861–1868. https://doi.org/10.2353/ajpath.2006.051302

Vasta, J. D., & Raines, R. T. (2016). Human Collagen Prolyl 4-Hydroxylase Is Activated by Ligands for Its Iron Center. *Biochemistry*. https://doi.org/10.1021/acs.biochem.6b00251

Vicente-Manzanares, M., Ma, X., Adelstein, R. S., & Horwitz, A. R. (2009). Non-muscle myosin II takes centre stage in cell adhesion and migration. *Nature Reviews Molecular Cell Biology*, *10*(11), 778–

790. https://doi.org/10.1038/nrm2786

Wakatsuki, T., Schwab, B., Thompson, N. C., & Elson, E. L. (2001). Effects of cytochalasin D and latrunculin B on mechanical properties of cells. *Journal of Cell Science*.

Walmsley, A. R., Batten, M. R., Lad, U., & Bulleid, N. J. (1999). Intracellular retention of procollagen within the endoplasmic reticulum is mediated by prolyl 4-hydroxylase. *Journal of Biological Chemistry*. https://doi.org/10.1074/jbc.274.21.14884

Wang, A. Y., Leong, S., Liang, Y. C., Huang, R. C. C., Chen, C. S., & Yu, S. M. (2008). Immobilization of growth factors on collagen scaffolds mediated by polyanionic collagen mimetic peptides and its effect on endothelial cell morphogenesis. *Biomacromolecules*. https://doi.org/10.1021/bm800727z

Wang, M., Liu, Y., Fang, W., Liu, K., Jiao, X., Wang, Z., Wang, J., & Zang, Y. S. (2017). Increased SNAT1 is a marker of human osteosarcoma and potential therapeutic target. *Oncotarget*, *8*(45), 78930–78939. https://doi.org/10.18632/oncotarget.20693

Wassie, A. T., Zhao, Y., & Boyden, E. S. (2019). Expansion microscopy: principles and uses in biological research. In *Nature Methods* (Vol. 16, Issue 1, pp. 33–41). Nature Publishing Group. https://doi.org/10.1038/s41592-018-0219-4

Williams, R. M., Zipfel, W. R., & Webb, W. W. (2005). Interpreting second-harmonic generation images of collagen I fibrils. *Biophysical Journal*, *88*(2), 1377–1386. https://doi.org/10.1529/biophysj.104.047308

Xu, Y., & Kirchner, M. (2021). Collagen mimetic peptides. In *Bioengineering* (Vol. 8, Issue 1, pp. 1–24). MDPI AG. https://doi.org/10.3390/bioengineering8010005

Yao, Y., Smal, I., Grigoriev, I., Akhmanova, A., & Meijering, E. (2020). Deep-learning method for data association in particle tracking. *Bioinformatics*, *36*(19), 4935–4941. https://doi.org/10.1093/bioinformatics/btaa597

Zanussis, S., Dolianas, R., Segats, D., Bonaldos, P., & Colombattisll, A. (1992). THE JOURNAL OF BIOLOGICAL CHEMISTRY The Human Type VI Collagen Gene mRNA AND PROTEIN VARIANTS OF THE a3 CHAIN GENERATED BY ALTERNATIVE SPLICING OF AN ADDITIONAL 5-END EXON*. In *Journal of Biological Chemistry* (Vol. 267, Issue 33). https://doi.org/10.1016/S0021-9258(18)35949-0

Zeitvogel, J., & Werfel, T. (2020). Use of 2D and 3D cell cultures in dermatology. In *Hautarzt* (Vol. 71, Issue 2, pp. 91–100). Springer Medizin. https://doi.org/10.1007/s00105-019-04537-7

Zeug, A., Stawarski, M., Bieganska, K., Korotchenko, S., Wlodarczyk, J., Dityatev, A., & Ponimaskin, E. (2014). Current microscopic methods for the neural ECM analysis. In *Progress in Brain Research* (Vol. 214, pp. 287–312). Elsevier B.V. https://doi.org/10.1016/B978-0-444-63486-3.00013-X

Zhang, D., Li, J., Wang, F., Hu, J., Wang, S., & Sun, Y. (2014). 2-Deoxy-D-glucose targeting of glucose metabolism in cancer cells as a potential therapy. In *Cancer Letters*. https://doi.org/10.1016/j.canlet.2014.09.003

Zhao, H. L., Zhang, C. P., Zhu, H., Jiang, Y. F., & Fu, X. B. (2017). Autofluorescence of collagen fibres in scar. *Skin Research and Technology*, *23*(4), 588–592. https://doi.org/10.1111/srt.12375

Zuo, Y., Hu, J., Xu, X., Gao, X., Wang, Y., & Zhu, S. (2019). Sodium azide induces mitochondria-mediated apoptosis in PC12 cells through Pgc-1α-associated signaling pathway. *Molecular Medicine Reports*. https://doi.org/10.3892/mmr.2019.9853

Zylberberg, L., Bereiter-Hahn, J., & Sire, J. Y. (1988). Cytoskeletal organization and collagen orientation in the fish scales. *Cell and Tissue Research*, *253*(3), 597–607. https://doi.org/10.1007/BF00219750